Ingrid Gryteland Holm

Laboratory testing of a monopile in dry sand

For verification of a macro model

June 2020

NTNU
Norwegian University of
Science and Technology

NTNU
Norwegian University of
Science and Technology

Laboratory testing of a monopile in dry sand

For verification of a macro model

Ingrid Gryteland Holm

Bygg- og miljøteknikk
Submission date: June 2020
Supervisor: Gudmund Reidar Eiksund

Norwegian University of Science and Technology
Department of Civil and Environmental Engineering

Preface

This master thesis in geotechnics under the Department of Civil and Environmental Engineering is written as part of the MSc in Civil and Environmental Engineering at NTNU. The work was carried out during the spring semester of 2020, and is a continuation of the specialization project conducted during the fall semester of 2019.

The idea for the thesis was brought up by Gudmund Eiksund, as a post study of the PhD work conducted by Ana Page at NGI, supervised by Gudmund. Page's PhD work was part of a research project lead by NGI, with the aim of reducing cost of offshore wind.

<div align="center">

Trondheim, 2020-06-11

Ingrid G. Holm

Ingrid Gryteland Holm

</div>

Acknowledgements

Abstract

The purpose of this master thesis was to conduct a small scale laboratory test of a monopile in dry sand, and use the results to calibrate and verify a macro model created to describe pile-soil interaction in integrated dynamic load analyses. The macro model was developed as part of a project with the aim of reducing costs of offshore wind. Previously, the model has been verified for homogeneous clay ground conditions and layered soils with mainly clay. It is therefore desired to expand its applicability by verifying it for sand conditions.

Static pushover analyses with pure horizontal force and moment applied at mudline were conducted in order to create input for the macro model. To generate data that could be used for comparison with the predicted pile response from the macro model, the pile was subjected to multidirectional loading and combined loading in-plane. All tests performed in the lab were also recreated in the FE program PLAXIS 3D for comparison.

The lab and PLAXIS results were coinciding, but the generated input from both failed to properly calibrate the macro model. Pile response predicted by the macro model could therefore not be compared with the experiments. In an attempt to solve the calibration problem, the calibration routine was adjusted, but new problems arose that were not solved in this thesis.

It was concluded that the macro model could not be verified for sand conditions with the tested input. It should therefore be investigated if the conducted experiments are unsuitable to test the macro model, due to near surface scale effects as a result of the pile being buried close to the sand surface. An alternative is to adjust the macro model to work for cases such as the tested input.

Sammendrag

Hensikten med denne masteropppgaven var å gjennomføre et labforsøk på en monopel i tørr sand. Resultatene skulle brukes til å verifisere en makromodell som beskriver interaksjonen mellom pel og jord i intergrerte dynamiske lastanalyser. Makromodellen ble utviklet som en del av et prosjekt som har til hensikt å redusere kostnadene ved offshore vindturbiner. Tidligere har modellen blitt verifisert for grunnforhold med homogen leire, og lagdelt jord med hovedsaklig leire. Derfor er det ønsket å også verifisere modellen for sand.

Statiske pushover-analyser med ren horisontallast og rent moment påført ved sandoverflaten ble gjennomført for å generere input til makromodellen. Det ble også gjennomført forsøk der pelen ble utsatt for kombinerte laster, i og ut av planet. Disse skulle senere brukes til å sammenligne med responsen fra makromodellen. Alle forsøkene gjennomført i laben ble også modellert med elementmetodeprogrammet PLAXIS 3D til sammenligning.

Resultatene fra labforsøk og PLAXIS modellering stemte godt overens, men makromodellen feilet i kalibreringen med input fra begge tilfeller. Pelresponsen fra forsøkene med kombinerte laster kunne derfor ikke sammenlignes med responsen fra makromodellen. Det ble forsøkt å korrigere kalibreringsproblemene ved å endre på kalibreringsrutinen, men det førte til nye problemer med modellen som ikke kunne løses i denne masteroppgaven.

Det ble konkludert med at makromodellen ikke kunne verifiseres for sand med input fra gjennomførte labforsøk eller PLAXIS modellering. Det burde undersøkes om de gjennomførte forsøkene ikke egner seg til å verifisere makromodellen, på grunn av skalaeffekter som en konsekvens av at pelen var begravd nær sandoverflaten. Et alternativ er å tilpasse modellen slik at den er gyldig for tilfeller som den testede inputen.

List of Figures

List of Tables

Contents

Appendix   **53**

List of symbols

a_{ik} Coefficients representing size and orientation of yield surface i

A_k Coefficients contained in the macro model consistency condition

b/a Ratio between the elliptical yield surface axes

c' Cohesion

C_u Coefficient of uniformity

D Diameter

Dr Relative density

du^p Plastic displacement increment

$d\boldsymbol{v}^p$ Incremental plastic displacement vector

d_{50} Mean grain size

$d\lambda$ Incremental multiplier

$d\theta^p$ Plastic rotation increment

E_i Initial Young's modulus

E_{50}^{ref} Reference Young's modulus for loading

E_{50} Young's modulus for loading

E_{ur}^{ref} Reference Young's modulus for unloading

E_{ur} Young's modulus for unloading

E_{oed}^{ref} Reference oedometer modulus

E_{oed} Oedometer modulus

$\boldsymbol{f}$ Yield surface vector

H Horisontal force

H_x Force in x-direction

H_y Force in y-direction

H_z Force in z-direction

$\boldsymbol{K}$ Elastic stiffness matrix

K_0 Earth pressure coefficient

K_0^{NC} Earth pressure coefficient for normal consolidation

L Length

m Stress exponent

M	Overturning moment
M_x	Moment around x-axis
M_y	Moment around y-axis
M_z	Moment around z-axis
n	porosity
p_{ref}	Reference stress equal to atmospheric pressure
q_a	Asymptotic shear strength
q_f	Deviatoric failure stress
$\boldsymbol{R}$	Transformation matrix
s	Variable determining compression of the yield surfaces in transformed load space
S_i	Radius in transformed yield surface i
$\boldsymbol{t}$	Force vector
$\boldsymbol{t}'$	Transformed force vector
u_x	Displacement in x-direction
u_y	Displacement in y-direction
u_z	Displacement in z-direction
u_H	Displacement caused by horizontal force, H
u_M	Displacement caused by overturning moment, M
$\boldsymbol{v^e}$	Elastic displacement vector
W_p	Plastic work
$\boldsymbol{\alpha}_i$	Variables defining the position of the i'th yield surface center
β	Variable determining the rotation of the yield surfaces
ϵ_1	Axial strain
γ_{sat}	Saturated unit weight
γ_{unsat}	Unsaturated unit weight
ϕ	Friction angle
ϕ_u	Angle of contours of plastic displacement
ϕ_θ	Angle of contours of plastic rotation
ψ	Dilatancy angle
ν	Poisson's ratio
ν_{ur}	Poisson's ratio for unloading and reloading

ρ_s	Grain density
σ_v	Vertical stress
σ_1	Largest principle stress
σ_3	Smallest principle stress
θ_x	Rotation around x-axis
θ_y	Rotation around y-axis
θ_z	Rotation around z-axis
θ_H	Rotation caused by horizontal force, H
θ_M	Rotation caused by overturning moment, M

Acronyms

DOF	Degree of freedom
FE	Finite element
FEA	Finite element analysis
HS	Hardening soil
NC	Normally consolidated
NGI	Norges Geotekniske Institutt
NTNU	Norges Tekniske-Naturvitenskapelige Universitet
OC	Over consolidated
OWT	Offshore wind turbine

Chapter 1

Introduction

1.1 Background

In design of offshore wind turbines (OWTs), foundation on monopiles is a popular solution. As of February 2020, 81% off installed OWTs are founded on monopiles according to a report by Wind Europe (2020). Today's industry practice to represent the monopile foundation behaviour in integrated load analyses, meaning analysis of the entire OWT under dynamic loading, is the py-method. This method is developed for long, flexible and slender piles (Det Norske Veritas, 2014). The monopiles used as foundation for OWTs are not flexible and slender, and the method is in general not valid (Det Norske Veritas, 2014). By the use of py-curves, foundation stiffness and fundamental frequencies tend to be underestimated (Zaaijer (2006), Shadlou and Bhattacharya (2016) and Hald et al. (2009)). Finite element analysis (FEA) can also be used to predict the pile response, but in design of OWTs, the response to thousands of load cycles are simulated, and FEA is therefore too time consuming and costly as it requires great computational effort. As a results, one is looking to other methods in order to increase the accuracy and efficiency in predicting pile response in load analyses.

REDWIN is a project led by NGI (Norges Geotekniske Institutt) with the aim of reducing cost of offshore wind by integrated structural and geotechnical design. As part of the REDWIN project, Ana Page worked on developing a model to accurately describe the soil and pile response in integrated load analyses during her PhD (Page, 2018). Page proposes a macro model, which will be presented in this master thesis. The macro model concept is to describe the pile response in one node located at the interface between foundation and structure. The model

must be calibrated, typically by the use of FEA, but only two loads cycles are needed. For the rest of the load analysis, the macro model is used with much higher efficiency than FEA, and with similar accuracy.

So far, Page has validated the foundation model against monotonic and cyclic FEA in clay and layered soil profiles with mainly clay, and against large-scale tests in clay. Among the recommendations for further research are to do analyses on drained and undrained sands, and compare with small and large scale field tests. Particularly comparison with multidirectional load tests in field are recommended (Page, 2018).

1.2 Problem formulation and research questions

Previously the macro model has been validated for clay, and a validation for sand conditions is desired. As a step towards validation of the model in sand, the aim of this master thesis is to conduct a small-scale load test of a pile in dry sand. The test program comprises of load with fixed and free rotation at ground level to calibrate the macro model, and multidirectional load with variable eccentricity with respect to ground level for validation of the macro model. Multidirectional load means that the resulting moment and horizontal force do not act in the same plane. Simulations of the lab pile were also to be performed in the geotechnical finite element (FE) program PLAXIS 3D, for comparison. Both numerical results and results from load tests can be used as input curves for calibration of the macro model.

During the project work done as a preparation for the master thesis, Holm (2019) attached in Appendix A3, the macro model was studied and simulations of the planned laboratory pile were performed in PLAXIS 3D. The results from PLAXIS were then used to calibrate the macro model, and to compare response under multidirectional loading. The author struggled to calibrate the macro model, and also experienced that the macro model produced an illogical response to multidirectional loading. These issues were therefore also to be addressed in the master thesis.

Lastly, the soil parameters used in the 3D modeling during the project work had to be optimized, when results from the laboratory test became available for comparison with the 3D model response.

The tasks that have been addressed in this master thesis are summed up in the following research questions:

- Can the PLAXIS model be optimized so that the calculation results match the results from laboratory testing?

- Can input for the macro model successfully be generated with laboratory testing?

- Can the macro model code be verified by testing different input curves from laboratory experiments and PLAXIS modeling?

- Is the macro model developed in the REDWIN project valid for pile-soil interaction in dry sand?

- Does the macro model predict realistic pile response to multidirectional loading

1.3   Structure of the thesis

The rest of this thesis is structured in the following way:

- Chapter 2 contains theory regarding monopiles used for OWTs in general, the theory behind the macro model investigated in this thesis, and the theoretical background for the soil model used in the 3D modeling.

- Chapter 3 explains the methods used in the laboratory testing, in the 3D modeling and to extract input for the macro model from the lab and 3D modeling. The investigation of the macro model source code is also explained.

- Chapter 4 presents the results from laboratory testing, 3D modeling and the investigation of the macro model.

- In chapter 5, the results from the previous chapter are analyzed and discussed.

- In chapter 6 the research questions are answered and the conclusion is made. Suggestions for further work are also presented.

Chapter 2

Theory

2.1 OWTs and monopiles

To meet the worlds increasing demand of energy, or more specifically *clean energy*, the development of OWTs are continuing and the number of offshore windfarms are growing. To make it profitable producing wind energy offshore, the costs must be reduced. According to Krohn et al. (2009), the foundation of a medium sized wind turbine represents 20-25% of the total costs of the turbine. (The reference is quite old, but it is reasonable to believe that the number have not changed drastically since 2009). However, this means that the costs can be reduced substantially if the foundation models can be improved.

2.1.1 Monopiles

The most used foundation for the OWTs are monopiles, which is a hollow large-diameter steel cylinder penetrated into the ground. The monopiles used for OWTs are subjected to large lateral forces compared to the axial forces, and the response to lateral load is hence the major concern in design. Typical monopiles have diameters of 4-7m and are 20-40m long. In comparison to piles that have been used for offshore structures, like jacket structures, for decades, the dimensions are very different. Those piles have typical diameters of 1.2-2.8m, and are 40-100m long (Hanssen, 2016). The traditional piles are long, flexible and slender, whereas the monopiles are shorter and show a more rigid behavior during deformation. It is documented, for instance in Hald et al. (2009) and Zaaijer (2006), that the traditional py-method (Det Norske Veritas, 2014) to describe pile-soil interaction is not suitable for monopiles. The foundation stiff-

ness and fundamental frequencies tend to be underestimated. As Hanssen (2016) mentioned in his PhD; high accuracy in prediction of the dynamic response of the OWT is required, because the system eigenfrequency is often close to the excitation frequencies from environmental- and rotor loads. And the dynamic response of the OWT is much affected by the foundation stiffness. Hanssen (2016) also explains that while it in geotechnical design of traditional offshore oil and gas structures have been important with cyclic and static ultimate capacity, it is just as crucial with dynamic foundation stiffness during fatigue and serviceability limit state in design of OWTs. This means, that it is even more important to correctly describe the foundation behavior for the OWTs.

2.1.2 Pile-soil interaction for monopiles

In order to correctly describe the soil-pile interaction, knowledge of soil properties such as stiffness must be at hand. It is well known that soil stiffness is nonlinear and dependent on strain level (Nordal, 2019). Soil stiffness decreases with increasing strain level. The stiffness reduction is a key aspect when it comes to laterally loaded piles, such as monopiles for OWTs. The soil around the pile will experience huge variations in strain level, typically larger strains near the soil surface and smaller strains deeper down. Soil strains will also decrease radially with distance from the pile. Due to these facts, it is necessary to describe the soil behavior under different strain levels. A soil model that does account for degradation of soil stiffness is presented in section 2.3.

2.2 Macro model

Parts of this section is copied from Holm (2019) in Appendix A3, but it has partly been rewritten and new information has been added.

A macro element is used to describe the foundation behavior in one point typically through 3 or 6 degrees of freedom (DOFs) (Skau et al., 2018). As the development of OWTs has taken place the last decades, so has the development of macro models for turbine foundations. Skau et al. (2018) argues that the general problem with previously published macro element methodologies is that they miss an approach to adapt the models to varying ground conditions. He says that research has focused on the theoretical formulation of macro elements, without including a

way to adapt them to real and varying soil conditions. There is therefore a need to develop more practically formulated macro models, and Page (2018) did so in her PhD. The macro model for monopiles proposed by her will hereby be presented.

2.2.1 Model formulation

Ana Page have formulated a model (Page et al., 2019) that describes a pile's response to loading in one point, located in the interface between foundation and structure, usually at seabed. The situation is illustrated in Figure 2.1. This macro model requires much less computational effort than traditional finite element analysis (FEA), and predicts the pile behavior with higher accuracy than the conventional py-curve method described in Det Norske Veritas (2014).

Figure 2.1: Figure showing the concept of the macro model, from Løkke et al. (2018).

The macro model applies load, t, at the center of the pile at mudline, and the pile response, v, is described with only 6 DOFs. These are three displacements, u_x, u_y and u_z, and three rotations, θ_x, θ_y and θ_z. The load and displacement components with the sign convention are shown in Figure 2.2. The response to vertical load and torsion is considered elastic and uncoupled, whereas the response to lateral loading is described as non-linear and with a coupling between the response in perpendicular planes, that is between u_x and θ_y, and u_y and θ_x (Page et al., 2019). This means that the response in the direction of a load is softer when also applying a load in the perpendicular horizontal plane, than when only applying load in one direction.

(a) Force components.   **(b)** Displacements components.
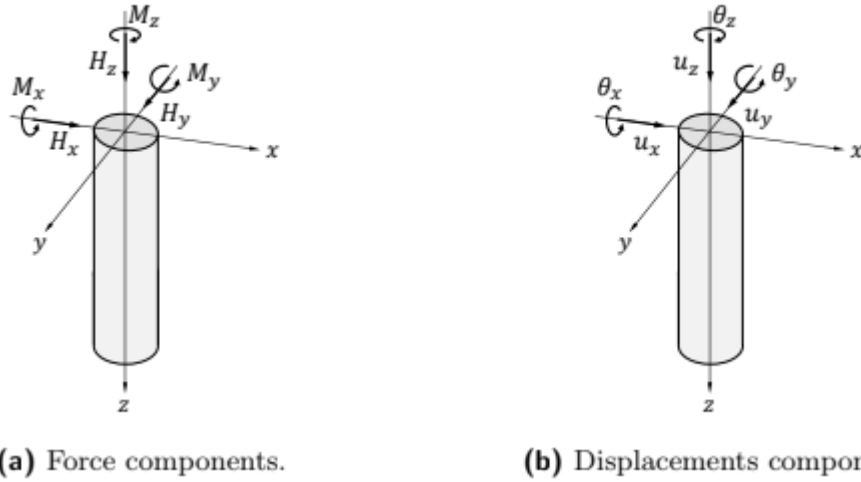
Figure 2.2: Figure showing the sign convention used in the macro model, from Page (2018).

The macro model is based on multi-surface plasticity, and consists of the following components:

- A relationship that separates the elastic and plastic contribution.

- Yield surfaces defining possible load combinations.

- A hardening law that controls the movement of the yield surfaces.

- A flow rule controlling the plastic deformation when yielding.

The elastic contribution is related to the applied load through an elastic stiffness matrix, $\boldsymbol{K}$ (Equation 2.1a). The plastic contribution is then the total response minus the elastic (Equation 2.1b).

$$\boldsymbol{t} = \boldsymbol{K} \cdot \boldsymbol{v}^e \tag{2.1a}$$

$$\boldsymbol{v}^p = \boldsymbol{v} - \boldsymbol{v}^e \tag{2.1b}$$

An initial yield surface describes the border between elasticity and elastoplasticity (Page et al., 2018). A failure surface represents the limit of possible force states. In between these two surfaces are load surfaces or yield surfaces, and the plastic response between the surfaces depend on how the load surfaces move in load space, in other words the hardening (Løkke et al., 2018).

Kinematic hardening is applied in the macro model, which means that the surfaces can translate and even intersect, however they do not change shape or size. Furtermore, the yield

7

surfaces do not rotate, and they are hence homothetic to each other. Figure 2.3 illustrates how the yield surfaces translate in a 2D-load space. A more elaborating description of the hardening rule is given in Appendix A1.1.
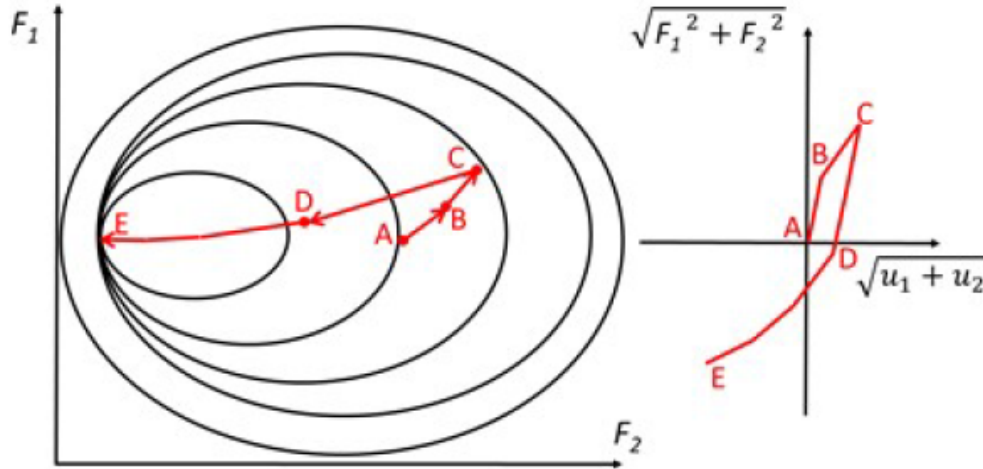
Figure 2.3: Figure illustrating the multi-surface plasticity model and the translation of yield surfaces in load space, from Løkke et al. (2018).

The yield surfaces are rotated ellipses in 2D-load space. When taking the effect of multidirectional loading into account, the yield surfaces become 4D ellipsoids. An illustration of the situation is shown in Figure 2.4. The illustration shows that when applying an overturning moment at the pile head, one will increase the capacity if at the same time applying a counteracting horizontal force. The yield criterion is a function of in-plane loads H_x and M_y, and out-of-plane loads H_y and M_x. They also represent contours of constant plastic work, which is calculated according to Equation 2.2 (Page et al., 2019).

$$W^p = \int\limits_0^{u_y^p} H_y \cdot du_y^p + \int\limits_0^{u_x^p} H_x \cdot du_x^p + \int\limits_0^{\theta_y^p} M_y \cdot d\theta_y^p + \int\limits_0^{\theta_x^p} M_x \cdot d\theta_x^p \qquad (2.2)$$
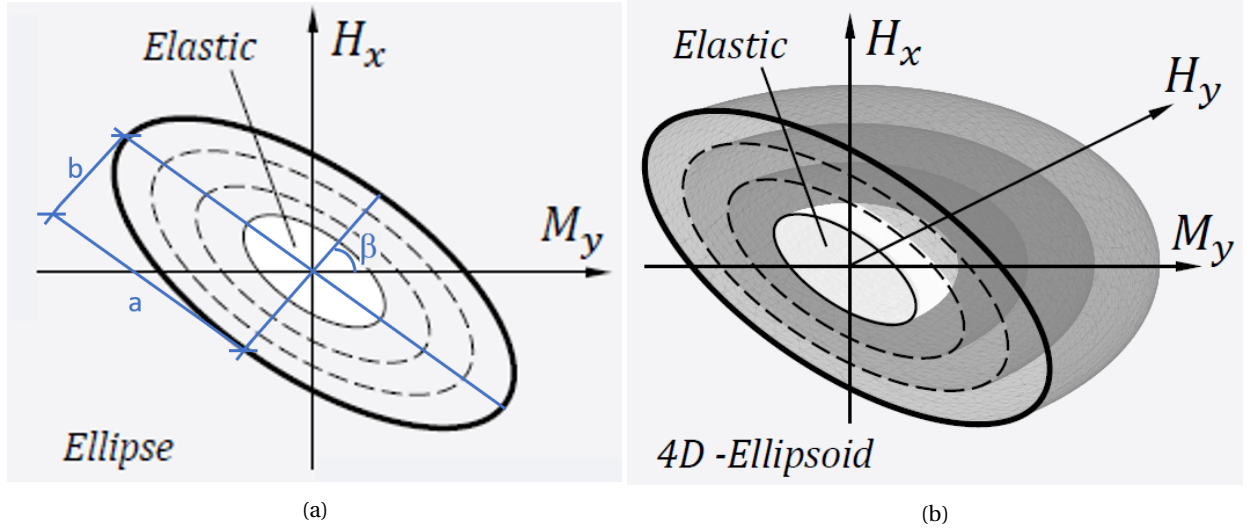
Figure 2.4: (a) 2D elliptical yield surface in load space. From Page (2018). (b) 4D ellipsoid yield surfaces in load space. From Page (2018).

In 2D loadspace, the elliptical yield surfaces are formulated as in Equation 2.3. A similar expression for the yield surfaces in 4D load space can be found in Page et al. (2019). $\boldsymbol{\alpha}_i$ are generalized state variables defining the center of yield surface i, or so called back stress, in load space. β defines the rotation of the surfaces, and coefficients a_i and b_i are the lengths of the ellipse axes. They are illustrated in Figure 2.4a, and as the figure suggests, β must be on the interval $\langle 0°, 90° \rangle$. β and the ratio b_i / a_i are constant for all the yield surfaces, hence homothetic surfaces.

$$f_i(\boldsymbol{t}, \boldsymbol{\alpha}) = \tag{2.3}$$

$$\left(\frac{M/D - \alpha_{M,i} \cdot \sin\beta + (H - \alpha_{H,i}) \cdot \cos\beta}{b_i} \right)^2 +$$
$$\left(\frac{-M/D - \alpha_{M,i} \cdot \cos\beta + (H - \alpha_{H,i}) \cdot \sin\beta}{a_i} \right)^2 - 1 = 0$$

The response between each load surface is incrementally linear. Each load increment causes elastoplastic displacement, and whenever a new load surface is reached, plastic strains occur. Plastic flow in this model is defined by an associated flow rule, meaning the direction of plastic flow is perpendicular to the yield surface or contours of constant plastic work. The flow rule is more thoroughly described in Appendix A1.1.

2.2.2 Model input

The necessary input in this model are an elastic stiffness matrix, and non linear load-displacement curves. The number of loading surfaces can also be selected, and a number in the range 15-25 is recommended (Løkke et al., 2018). Load-displacement curves can for instance be extracted from FEA, by running two static pushover analyses; one with an overturning moment at seabed, and one with lateral load applied at seabed, shown in Figure 2.5. The load displacement curves must be monotonically increasing (Løkke et al., 2018). It is assumed that the response is equal in all horizontal directions (Page et al., 2018). Even though FEA may be needed to calibrate the model, only two load cycles need to be run with FEA, whereas the rest of the maybe thousands of load cycles can be run with the macro model.
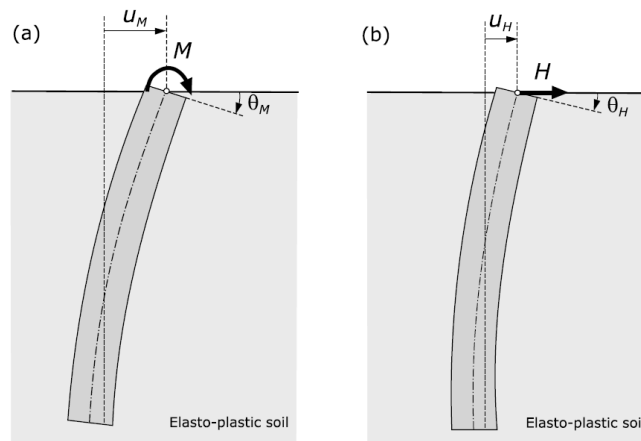
Figure 2.5: Loading conditions applied to determine non linear load-displacement curves, from Page et al. (2018)

2.2.3 Numerical implementation and calibration

The macro model is written in the programming language Fortran through the code editor Microsoft Visual Studios. To create an executable program, the Fortran files have been compiled using Intel Fortran compiler (Løkke et al., 2018). The model has been implemented in OWT simulation softwares, but in the master project the model was used through a matlab-script written by Ana Page. With the matlab script, a wanted loadhistory can be applied in the macro model, along with the necessary input to calibrate the model. The script then executes the macro model, and returns the response caused by the applied loadhistory.

When provided with the correct input, the macro model is calibrated like this; plastic displacements are computed from the input load displacement curves as the difference between

the total displacements and the elastic contribution. Secondly, the ellipse parameters β and b/a are calculated based on the plastic input curves as explained in next paragraph.

Note that the theory in this paragraph and the following equations are from a document received from Ana Page on the calibration of the macro model, and from the macro model code. In order to calculate the ellipse parameters, the calibration routine interpolates one of the input curves such that both input curves have forces and moments corresponding to the same plastic displacements and rotations. Then, plastic contour angles, which is the ratio between the horizontal force and moment corresponding to the same plastic displacement and rotation, are calculated. The idea is displayed in Figure 2.6, where lines are drawn between points on the H-axis and M-axis caused by the same plastic displacement and rotation. The contour angles of plastic displacements and rotations are calculated after Equation 2.4a and 2.4b respectively.

$$\phi_u^i = \left(\frac{H_i}{M_j}\right) \text{ for } u_p^i = u_p^j \tag{2.4a}$$

$$\phi_\theta^i = \left(\frac{H_i}{M_j}\right) \text{ for } \theta_p^i = \theta_p^j \tag{2.4b}$$

The contour angles are taken as the average value of all ϕ_u^i and ϕ_θ^i, and are further used to calculate the ellipse parameters after Equation 2.5 and Equation 2.6. A thorough derivation of the ellipse parameters from the contour angles are attached in Appendix A1.2.

$$\beta = \frac{\pi}{2} + \frac{1}{2} \cdot \arctan\left(\frac{2 \cdot \tan\phi_u}{\tan\phi_u \tan\phi_\theta - 1}\right) \tag{2.5}$$

$$\frac{b}{a} = \sqrt{\frac{\tan\phi_u \cdot \tan\phi_\theta + 1 - \sqrt{(\tan\phi_u \cdot \tan\phi_\theta - 1)^2 + 4\tan^2\phi_u)}}{\tan\phi_u \cdot \tan\phi_\theta + 1 + \sqrt{(\tan\phi_u \cdot \tan\phi_\theta - 1)^2 + 4\tan^2\phi_u)}}} \tag{2.6}$$
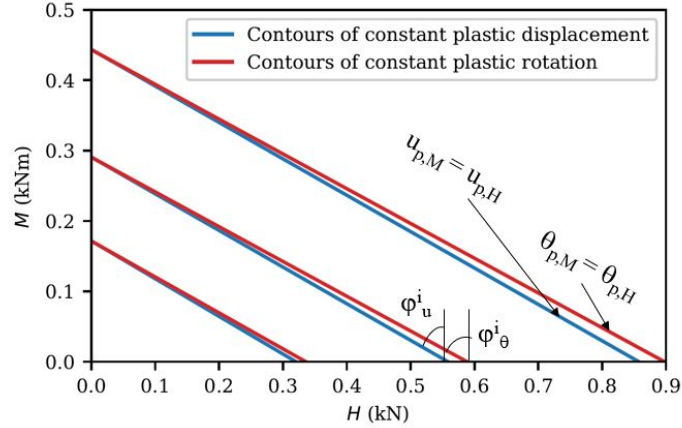
Figure 2.6: Figure displaying the concept of contours of constant plastic rotations and displacements. The blue lines connect points on the H-axis and M-axis with the same plastic displacement. The red lines connect points with the same plastic rotation.

When the ellipse parameters have been calculated, the calibration continues and the transformation matrix $\boldsymbol{R}$ is calculated based on the ellipse parameters. $\boldsymbol{R}$ is used to shift the input load-plastic displacement curves to the transformed load space. The yield surfaces are four dimensional spheres in the transformed load space, where the response in any radial direction is the same. Based on the transformed input curves, the radius of the yield surfaces, and the plastic stiffness matrix for each surface are calculated. Reference is made to Appendix A1.1 for a more thorough description of the calibration.

2.3   Hardening soil

This section is copied from Holm (2019) in Appendix A3.

The hardening soil model (HS) in PLAXIS is an elastoplastic model that accounts for the stress dependent stiffness of soils. The model combines hardening in shear governed by a Coulomb criterion, with volumetric hardening governed by preconsolidation stress (PLA, 2018a).

The yield surface in the hardening soil model consists of two components; a "cone" and a "cap". The cone is defined by the coulomb criterion and the cap is defined by the preconsolidation stress (Nordal, 2019). When shear loading approaches failure, the cone expands and plastic strains occur. Similarly, volumetric loading past preconsolidation stress causes expansion of the cap and corresponding plastic volumetric strains. This behaviour is similar to that in an oedometer test; stiff in the overconsolidated (OC) area and softer behavior in the normally con-

solidated (NC) area (Nordal, 2019). The elastic and plastic strains caused by shear are described by a hyperbola in case of a drained triaxial condition (PLA, 2018a), as displayed in Figure 2.7. In this figure, E_{50} is the secant modulus halfway to deviatoric failure stress, q_f, E_{ur} is the elastic stiffness in unloading-reloading and q_a is the asymptotic shear strength defined as $q_a = q_f/0.9$. The total yield surface with the cone and the cap is visualized in Figure 2.8.
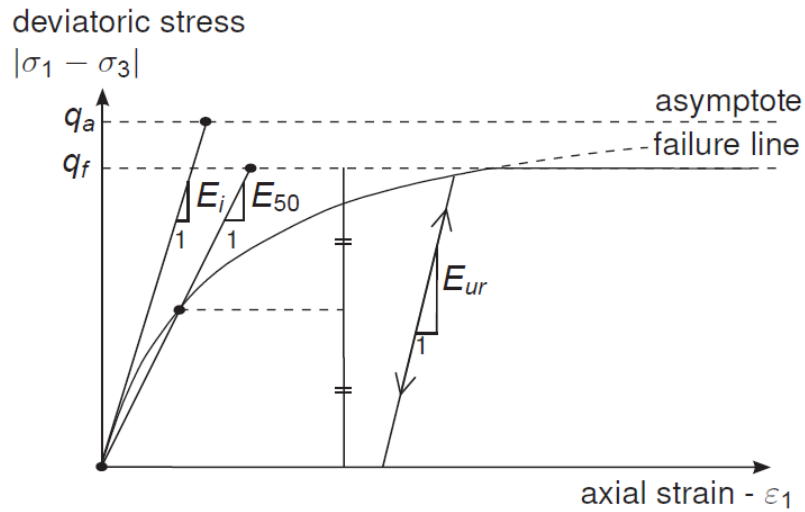
Figure 2.7: Hyberbolic stress-strain relationship in a standard drained triaxial test (PLA, 2018a)
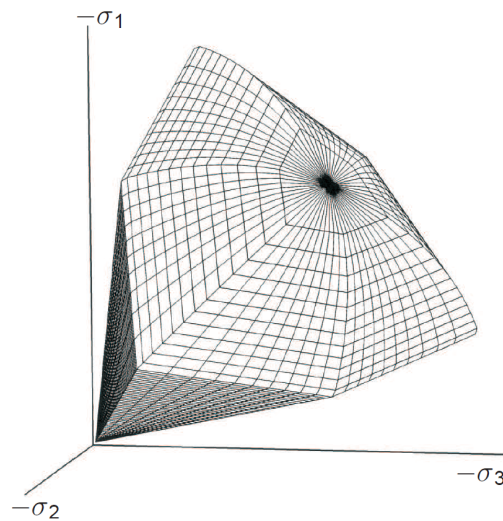
Figure 2.8: Yield surface represented by a cap and a cone in a principal stress diagram (PLA, 2018a)

The basic input parameters in the hardening soil model from (PLA, 2018a) is presented below.

- E_{50}^{ref} (kPa): Secant stiffness in standard drained triaxial test. Elastoplastic parameter controlling plastic strains caused by deviatoric loading

- E_{ur}^{ref} (kPa): Elastic unloading/reloading stiffness, connected to elastic unloading and reloading within the yield surface.

- E_{oed}^{ref} (kPa): Tangent stiffness for oedometer loading, connected to plastic strains caused by compression.

- m: Parameter controlling the stress dependent stiffnesses.

- c' (kPa): cohesion

- ϕ' (°): Friction angle.

- ψ (°): Dilatancy angle

- ν_{ur}: Poisson's ratio in unloading/reloading

- p^{ref} (kPa): Reference stress for stiffness, default 100kPa

- K_0^{NC}: K_0 for normal consolidation, default K_0^{NC} = 1-sinϕ

The reference parameters presented above are values defined at effective stress levels equal to p_{ref}; $\sigma_3' = p_{ref}$ for E_{50}^{ref} and E_{ur}^{ref}, and $\sigma_1' = p_{ref}$ for E_{oed}^{ref}. The stress dependent stiffnesses E_{50}, E_{ur} and E_{oed} are calculated according to equation 2.7, 2.8 and 2.9 respectively (PLA, 2018a).

$$E_{50} = E_{50}^{ref} \left(\frac{c\cos\phi - \sigma_3'\sin\phi}{c\cos\phi + p^{ref}\sin\phi} \right)^m \tag{2.7}$$

$$E_{ur} = E_{ur}^{ref} \left(\frac{c\cos\phi - \sigma_3'\sin\phi}{c\cos\phi + p^{ref}\sin\phi} \right)^m \tag{2.8}$$

$$E_{oed} = E_{oed}^{ref} \left(\frac{c\cos\phi - \sigma_1'\sin\phi}{c\cos\phi + p^{ref}\sin\phi} \right)^m \tag{2.9}$$

Chapter 3

Methods

3.1 Laboratory testing

Small scale testing of a monopile installed in dry sand, in the foundation laboratory at NTNU have been performed. The test setup is inspired by the test setup used by Hanssen (2016) and Tistel (2018) in their PhD work.

3.1.1 Test setup

Sand bin

The foundation laboratory at NTNU includes a sand bin made of concrete that measures 4m×4m×3m (B). The sand bin was filled by a spreader wagon that passed back and forth over the bin sprinkling sand through 462 nozzles. The nozzles can be adjusted to alter the sand density (porosity) Lieng et al. (1984). An illustrative sketch of the sand handling system is shown in Figure 3.1.

The bin was filled with an approximately 3m thick layer of dry sand. After the first filling, the sand surface was quite uneven. This happened because some of the chambers in the spreader emptied before the others, and the filling still continued for a while with empty chambers.

Due to the uneven filling of the sand bin, the area suitable for testing the pile was limited. Refilling the sand bin was therefore necessary after a while. The sand bin was emptied by removing 1m of the bottom sand, planing the surface and refilling the bin again. This time, it was payed close attention during the filling in order to secure that the chambers were refilled before they emptied and filling continued.
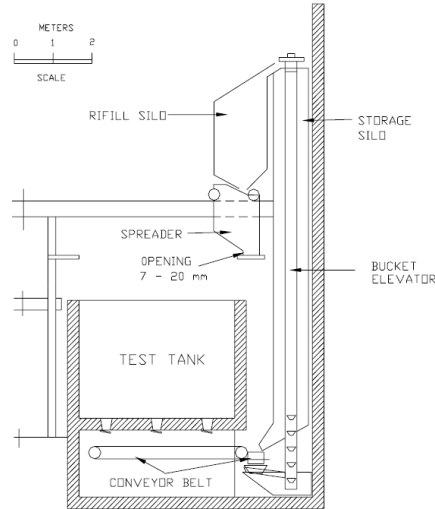
Figure 3.1: Sketch of the sand bin and sand handling system, from Tefera et al. (2006).

Test pile

Initially, the plan was to use the pile used by Hanssen (2016) with 27cm diameter. However, a very small deflection of the pile was achieved in the 3D modeling when applying the maximum force available from the test equipment. It was therefore chosen to use a smaller pile in order to get greater deformation. A cylindrical steel pile with 10cm diameter and 2mm wall thickness was used. It was embedded 0.6m in the sand, and the pile parameters are given in Table 3.1. In a 1:60 scale, this pile would have a real size diameter of 6m and an embedded length of 36m, which is a typical monopile size, see section 2.1.

Table 3.1: Parameters of the laboratory pile (Hanssen, 2016).

Parameter	Value
Diameter, D (m)	0.10
Embedded length, L (m)	0.6
L/D ratio	6
Wall thickness, t (m)	0.002
Unit weight, γ (kg/m^3)	7850
Young's modulus, E (GPa)	210
Poisson's ratio, v	0.3

Sand characterization

Hokksund sand has been used in the laboratory at NTNU for a long time, and its properties are well documented in for instance Lieng (1988) and Tadesse (2000). Some years ago, Sponesand

was mixed with the Hokksund sand used at NTNU, and the properties changed slightly. Both sands are natural glacifluvial deposits, and are characterized as uniform, medium grained and medium dense quartz sand (Søvik, 2017). The grain size distribution of the model sand, along with the distribution for both Hokksund sand and Sponesand are shown in Figure 3.2. The sand was used in experiments in 2017, and a master student performed several geotechnical tests on the sand. Properties are therefore taken from this work, Søvik (2017), and are given in Table 3.2. The sand after filling is characterized as loose.
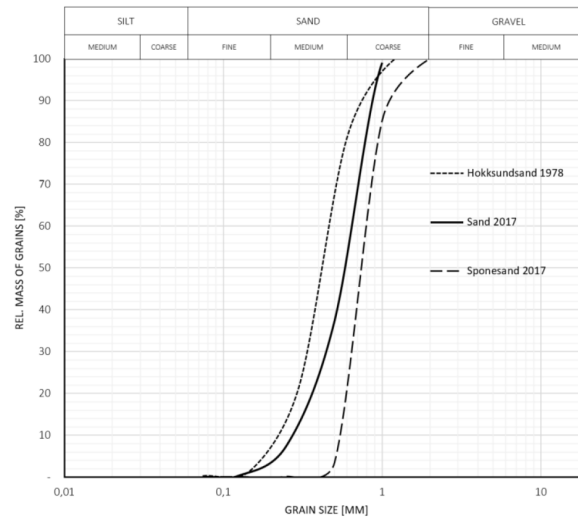
Figure 3.2: Grain size distribution for Hokksund sand, Sponesand and the sand used in the experiments. From Søvik (2017).

Table 3.2: Properties of the laboratory sand from Søvik (2017) and Tefera et al. (2006).

Parameter	Value
Dry friction angle, ϕ loose (deg)	36.7°
Dry friction angle, ϕ dense (deg)	39.8°
Cohesion, c (kPa)	0
Min. porosity, n_{min} (%)	35.4
Max. porosity, n_{max} (%)	46.4
Relative density, Dr (%)	65
Grain density, ρ_s (g/cm^3)	2.64
Coefficient of uniformity, $C_u = d_{60}/d_{10}$ (−)	2.3
Mean grain size, d_{50} (mm)	0.6

Pile installation procedure

The pile was placed on top of the filled sand bin and pushed into the sand by repeatedly hammering the top of it. Between each test, the pile was extracted from the sand and placed in

17

another spot of the sand bin.

Instrumentation and data measuring

The forces imposed on the pile are applied through actuators connected to ball screws. The ball screws are of type CCBR 32 (SKF) and can be regulated with an accuracy of 1/250mm. Their capacity is 2.5kN. Load application and recording are controlled by scripts written in the Windows-based programming language LabView, and the load application can be programmed as either displacement or load controlled.

In order to calculate rotation of the pile at mudline, the displacement at mudline and in one additional point had to be recorded. Recordings of displacement were either done with the actuators, or when load was not applied in the point where displacement had to be measured; with a string position transducer of brand Firstmark, also known as a string pot.

3.1.2 Test program

Four different tests were performed; 1) pure horizontal force applied at mudline, 2) pure moment applied at mudline through a force pair, 3) in-plane combination of moment and horizontal force, 4) both moment and horizontal force applied in two perpendicular planes. A summary of the test program is presented in Table 3.3, the loading regime shown in Figure 3.3, and each test is explained more thoroughly below. The table also tells in which filling of the sand bin the tests were performed. Pictures and schematic drawings of the test setup for all tests are attached in Appendix A2.1. Note that in Table 3.3, each repetition of a test is given a test ID, which will be used to address the tests from now on.
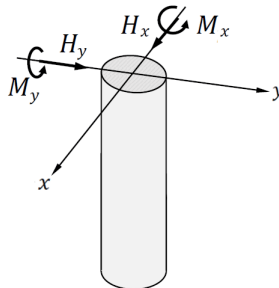
Figure 3.3: Loading regime used to define the direction of loads in laboratory, PLAXIS and in the macro model.

Table 3.3: Test program performed in the foundation laboratory. Loading according to loading regime shown in Figure 3.3.

	Test ID	H_x (N)	M_y (Nm)	H_y (N)	M_x (Nm)	Load application point (height above mudline)	Filling
Test 1, pure horizontal load	h1	1754				5cm	first
	h2	1506				8cm	first
	h3	1503				10cm	second
Test 2, pure moment	m1		789			218cm, 10cm	first
	m2		560			208cm, 9cm	first
Test 3, in-plane combination of load	mh1	284	613			221cm	first
	mh2	451	469			109cm	second
Test 4, multidirectional loading	multi1	253	519	507	-91	205cm, 15cm	second
	multi2	263	538	508	-79	204cm, 12cm	second
	multi3	223	459	712	-122	205cm, 14cm	second

Test nr. 1 - pure horizontal force at mudline

A schematic drawing and a picture of the test setup for test number 1 are shown in Figure 3.4. The test was repeated three times. One actuator was placed as close to mudline as possible for load application, and a string pot was placed approximately 200cm above the actuator to measure displacement. Due to practical reasons, there was a 5-10cm distance between the actuator and mudline. The load application point is considered as mudline.

Horizontal load was applied displacement controlled at a speed of 10 μm/s. In the first repetition of this test, there was a slip in the hinge between the support frame and the actuator at 687N applied load, causing a drop in the load. The test continued, and the part of the curve representing the load drop and reloading to 687N was cut off.

(a)

(b)

Figure 3.4: (a) Picture of test setup for test nr.1. (b) Schematic drawing of test setup for test nr.1. Note that not all details are drawn to scale, and all units are in mm. Depth of support frame is 600mm.

Test nr. 2 - pure moment at mudline

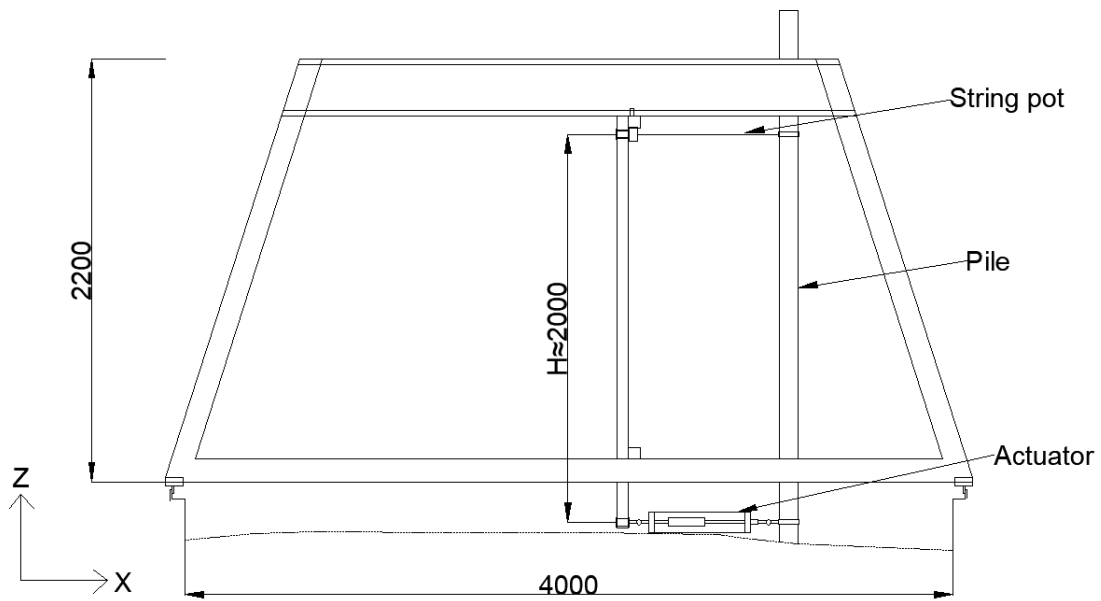A schematic drawing and a picture of the test setup for test number 2 are shown in Appendix A2.1. The test was performed twice. One actuator was placed as close to the sand surface as possible, and another one was placed approximately 200cm above. A moment was applied through a force pair; the upper actuator pushing the pile, and the lower actuator pulling the pile with equal force. The load application was force controlled. The LabView program controlled the test by trying to get the actuators to apply load with a speed of 0.02N/s. If the difference between the load in the two actuators passed 5N, the wanted force in each actuator would halt until the difference was below 5N.

Test nr. 3 - combination of loading in plane

A schematic drawing and a picture of the test setup for test number 3 are shown in Appendix A2.1. The test was repeated twice. The first time, one actuator was fastened to the pile 220cm above the sand surface, and the second time 109cm. A string pot was placed approximately 5cm above mudline, due to practical reasons it was not placed at mudline. The load was applied displacement controlled by the actuator pushing the pile with a speed of 10 μm/s.

Test nr. 4 - multidirectional loading

A schematic drawing and a picture of the test setup for test number 4 are shown in Appendix A2.1. One actuator was fastened to the pile 205cm above the sand surface. Another actuator was fastened to the pile orthogonal to the other, approximately 15 cm above the sand surface. In all three repetitions of the test, 115N was applied by the upper actuator in-plane, before halting and keeping this load constant. Then the lower actuator applied load in the perpendicular plane until a horizontal load of 500N in two of the tests, and 700N in the third test, was reached. The horizontal force out of the plane then halted and was kept constant, and the upper actuator continued to apply load in-plane.

Because load was applied in two perpendicular planes, the pile would move in both x- and y-direction. This caused the upper actuator, which was meant to apply load in x-direction, to also give a contribution to the loading in y-direction. In order to calculate this second order effect, and decompose the load in two directions, a string pot was fastened to the pile above the upper actuator to measure the displacement in this point out of the plane. The second order effect

caused by the lower actuator was not taken into account, due to much smaller displacement closer to the sand surface. The second order effects was calculated based on the trigonometric relations illustrated in Figure 3.5, and formulated in Equation 3.1.
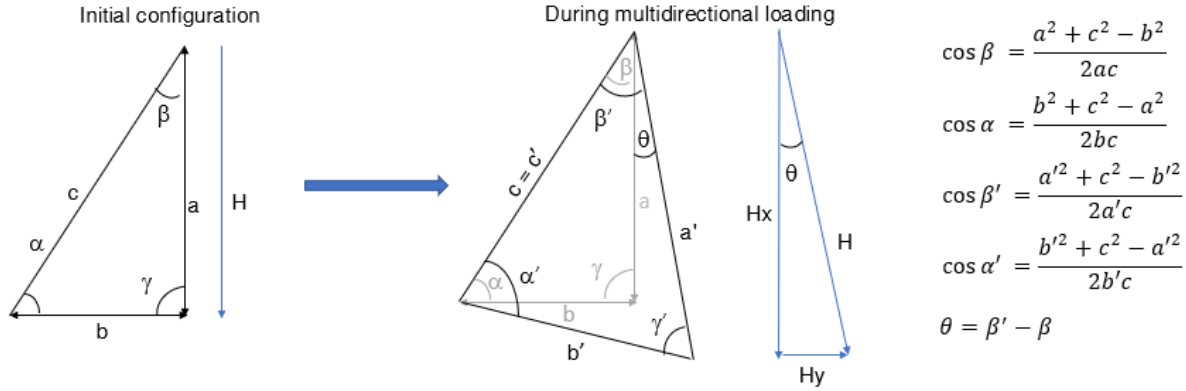
Figure 3.5: Illustration of how to decompose the applied force in the upper actuator into an in-plane and an out of plane load.

$$H_x = H\cos\theta \tag{3.1a}$$

$$H_y = H\sin\theta \tag{3.1b}$$

3.2   Modeling in PLAXIS 3D

3.2.1   Model and mesh

Because of the small size of the pile and the embedded length, it was considered sufficient to model the sand as a 2m×2m×1.5m ($L \times B \times H$) sand block in PLAXIS 3D. The pile center was placed 1m from the vertical boundaries, which were modeled as normally fixed. Due to symmetry, it was only necessary to model half of the pile for the in-plane load calculations. The pile center was then placed at the symmetry line, and 1m from the other vertical boundaries.

PLAXIS 3D uses 10 node tetrahedral volume elements to represent the soil. The pile is modeled with 6-noded triangular plate elements (PLA, 2018b). The soil in a 0.25m radius from the pile center has been modeled with a refined mesh with average element side length 0.05m. The meshed model is shown in Figure 3.6. The mesh used is quite coarse, and interface elements

were not used. A finer mesh and interface elements caused problems with the load advancement procedure in PLAXIS, and the problem was not resolved. It was considered sufficient to use the coarser mesh without interface elements because calculation results from PLAXIS and laboratory results matched quite well. Note that the pile is modeled as wished in place, and the pile installation effects are not considered.
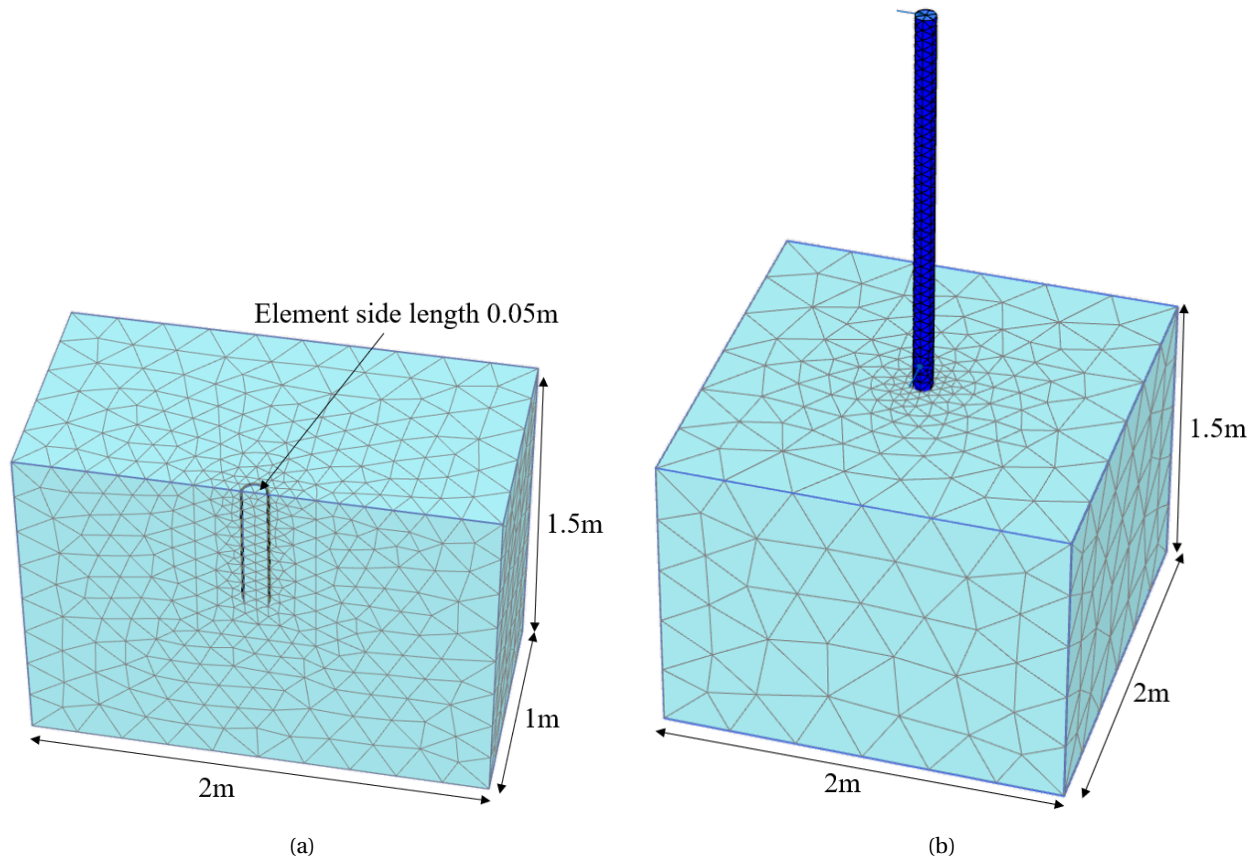
Figure 3.6: (a) Meshed PLAXIS model with half of the pile geometry. (b) Meshed PLAXIS model used to simulate multidirectional loading of the pile.

3.2.2 Parameter selection

The choice of soil parameters to represent the sand in the numerical PLAXIS model were studied closely in Holm (2019), and they were chosen based on the work of Hanssen (2016). However, a comparison with the laboratory tests demonstrated a poor match, and adjustments were necessary.

The necessity to describe soil properties at different strain levels, as described in section 2.1, lead to the choice of the HS soil model in PLAXIS. The model, its properties and parameters are

explained in section 2.3. The stiffness and strength parameters were found by trial and fail in order to make the results from lab test nr 1 and 2 in subsection 3.1.1 match with PLAXIS. The friction angle of the sand was given in for instance Tefera et al. (2006), but a lower value which is still reasonable for a loose sand, was better to match PLAXIS and lab results. Chosen soil parameters are presented in Table 3.5.

The pile was modeled with the parameters presented in Table 3.4.

Table 3.4: Pile parameters used as input in PLAXIS 3D.

Property	Value
Diameter, D (m)	0.10
Embedded length, L (m)	0.6
Wall thickness, t (m)	0.002
Unit weight, γ (kN/m^3)	77.0
Young's modulus, E (GPa)	210
Poisson's ratio, ν	0.3
Interface roughness, R	1.0

Table 3.5: Soil parameters used as input in PLAXIS 3D.

Parameter	Value
Condition	Drained
Soil model	HS
$\gamma_{sat} = \gamma_{unsat}$ (kN/m^3)	16
ϕ' (°)	35
ψ (°)	5
c' (kPa)	0.1
ν_{ur}	0.2
E_{50}^{ref} (MPa)	15
E_{ur}^{ref} (MPa)	30
E_{oed}^{ref} (MPa)	15
m	0.45

3.2.3 Load application

The loads presented in the test program in 3.1.2 were also applied in PLAXIS. In the half model, a rigid body was modeled at the pile head in order to apply loads. For the full model, a 10cm thick steel plate was modeled in the heights where loads were applied in order for the loads to distribute evenly over the pile's cross section. The loads were applied as point loads at the pile cross section center.

3.3 Input parameters in the macro model

This section is an edited version of the same section in Holm (2019) in Appendix A3.

3.3.1 Elastic stiffness matrix

As mentioned in section 2.2, the macro model needs an elastic stiffness matrix as input. Two load cases are considered, explained in subsection 2.2.2 and displayed in Figure 2.5. The resulting force-displacement, and moment-rotation curves can be used to calculate the elastic stiffness matrix, K, in Equation 3.2, where v^e and t are the elastic displacement vector and applied force vector respectively.

$$K v^e = t \tag{3.2}$$

Two basis cases, Equation 3.3 and Equation 3.4, are used to obtain four equations in matrix form. There are four unknown stiffness parameters in the equations, and by inserting the first nonzero points on the input load-displacement/rotation curves, the coefficients can be calculated.

$$\begin{bmatrix} k_{11} & k_{12} \\ k_{21} & k_{22} \end{bmatrix} \cdot \begin{bmatrix} u_H \\ \theta_H \end{bmatrix} = \begin{bmatrix} H \\ 0 \end{bmatrix} \tag{3.3}$$

$$\begin{bmatrix} k_{11} & k_{12} \\ k_{21} & k_{22} \end{bmatrix} \cdot \begin{bmatrix} u_M \\ \theta_M \end{bmatrix} = \begin{bmatrix} 0 \\ M \end{bmatrix} \tag{3.4}$$

By rearranging the four equations above, the following expressions for each element in the elastic stiffness matrix are achieved:

$$k_{22} = \frac{M \cdot u_H}{\theta_M \cdot u_H - \theta_H \cdot u_M} \tag{3.5}$$

$$k_{21} = -\frac{M \cdot \theta_H}{\theta_M \cdot u_H - \theta_H \cdot u_M} \tag{3.6}$$

$$k_{12} = \frac{H \cdot u_M}{\theta_H \cdot u_M - \theta_M \cdot u_H} \tag{3.7}$$

$$k_{11} = -\frac{H \cdot \theta_M}{\theta_H \cdot u_M - \theta_M \cdot u_H} \tag{3.8}$$

3.3.2   Nonlinear load displacement curves

Displacements and ΣM_{stage}, which is the completed proportion of a plastic calculation in PLAXIS (PLA, 2018b), are direct output for selected nodes in PLAXIS. ΣM_{stage} is used to calculate the applied load in each loadstep, and displacements are used to calculate rotations as it is no direct output from PLAXIS. In the lab experiments, forces and displacements were recorded, and as for the 3D modeling, rotations must be calculated from displacements.

Two points on the pile is selected for displacement measurements. In the 3D model, these points are along the pile wall at mudline and below mudline. For the lab pile, displacements are measured on the cylinder wall approximately at mudline, and in one point on the cylinder wall further up. As mentioned in section 2.2, load is applied at the pile head center in the macro model. It is therefore assumed that the displacements and rotations measured and calculated at a point on the cylinder wall is representative for the pile head cross section center.

Rotations are calculated according to Equation 3.9, where definition of each variable is shown in Figure 3.7. Δ_{x2} in Equation 3.9 is calculated after Equation 3.10, which is taken from the beam formulas in Bell (2018). Δ_{x2} is only taken into consideration if the pile is expected to have curvature. Curvature of the pile is only considered in the lab experiments when loads are applied above mudline. When this is not the case, Δ_{x2} is zero.

Due to small displacements, the impact of vertical displacements on the rotation is considered negligible.

$$\theta_y = \arctan\left(\frac{\Delta u_x - \Delta u_{x2}}{\Delta u_z}\right) \tag{3.9}$$

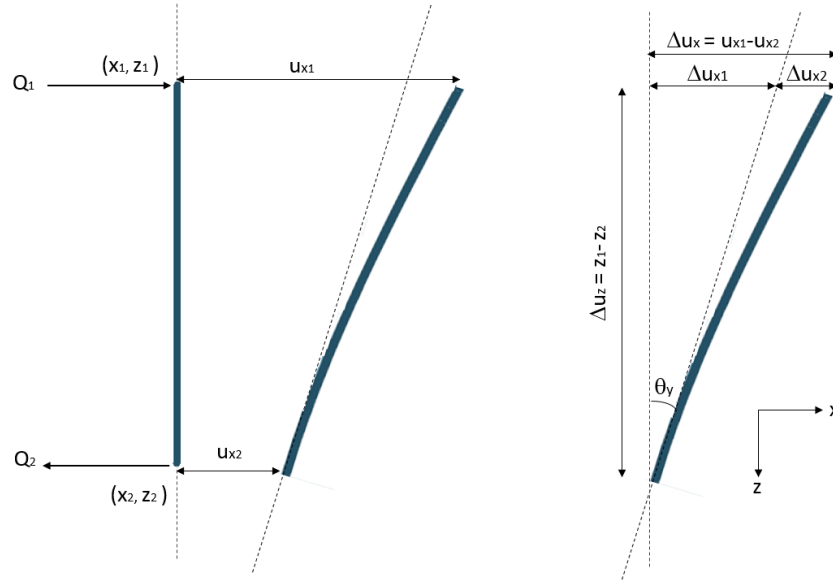$$\Delta u_{x2} = Q_1 \cdot \frac{\Delta_z^3}{3EI} \tag{3.10}$$

Figure 3.7: Sketch of how rotation of the pile head is calculated. Defintions for Equation 3.9.

3.4 Investigating the macro model code

During the project work, Holm (2019), the macro model sometimes failed to run and the reason was not identified. Therefore, the source code to the macro model e.i. the Fortran files mentioned in subsection 2.2.3, were provided by NGI, who owns the program. In order to discover where the macro model encountered problems during failed runs, print statements explaining what the code does at all times were added. The code was also edited so that results from the calibration routine such as the computed plastic displacements and rotations, the ellipse parameters, the transformed plastic displacements and plastic stiffness of the yield surfaces were saved to files. After making these changes to the code, a new executable program was compiled using Intel Fortran compiler. When running the new program, messages appeared on the screen explaining where in the code the program was at all times, and looking into the saved results from the calibration routine, it was possible to see where the problems were encountered.

It turned out that the input from PLAXIS modeling, and from the laboratory experiments produced illogical ellipse parameters, see Figure 2.4 (a), during calibration of the macro model. Therefore it was decided to apply radial load paths in the 2D load space($H - M$-plane) in PLAXIS and find the contours of constant plastic work in order to see what the yield surfaces should look like. The load paths in Table 3.6 were applied, and the plastic work was computed for all steps in

the load paths after Equation 2.2. A script was written to find points in each load path with the same plastic work, and plot them. The ellipse parameters β and b/a computed by the macro model were also used to compute the yield surfaces that should have corresponded with the contours from FEA. The procedure is explained in next paragraph.

The elliptical yield surfaces formulated in Equation 2.3 can also be written in a parametric form, which is easier to plot. Instead of writing M/D as in Equation 2.3, M is used for simplicity. Also, the generalized state variables $\boldsymbol{\alpha_i}$ are zero since the yield surfaces are centered in the origin. When taking this into account, the yield surfaces are expressed with Equation 3.11.

$$H(\theta) = b_i \cos\theta \cdot \cos\beta - a_i \sin\theta \cdot \sin\beta \tag{3.11a}$$

$$M(\theta) = b_i \cos\theta \cdot \sin\beta + a_i \sin\theta \cdot \cos\beta \tag{3.11b}$$

a_i and b_i are the axes of yield surface i, β the rotation angle and θ an angle running from 0 to 2π. Since the macro model only gives the ratio b/a, there is a need to express either a_i or b_i in terms of $M, H, b/a$ and β. For points on the input M-curve, H is zero and the original yield criterion (Equation 2.3) is simplified and used to find an expression for b_i:

$$f_i = \frac{M^2 \sin^2\beta}{b_i^2} + \frac{M^2 \cos^2\beta}{a_i^2} - 1 = 0$$

$$b_i = M \cdot \sqrt{\sin^2\beta + \cos^2\beta \left(\frac{b}{a}\right)^2}$$

With all the parameters in place, the ellipses in parametric form can be plotted.

In order to understand why the computed ellipse rotation angle did not fit well with FEA results, the derivation of the formulas for the ellipse parameters, Equation 2.5 and Equation 2.6, was conducted. Parts of the derivation was provided by Ana Page in an internal document, however some of the steps were missing, and the contour angles (Equation 2.4) was defined opposite in the provided document. The derivation can be found in Appendix A1.2. The resulting expression for β was different from the one used in the macro model. In an attempt to match the ellipses computed with the macro model ellipse parameters, with the contours computed from the radial paths in PLAXIS, the expression for β was changed in the calibration routine.

Table 3.6: Radial load paths applied on the PLAXIS model. Used to calculate plastic work and find contours of constant plastic work.

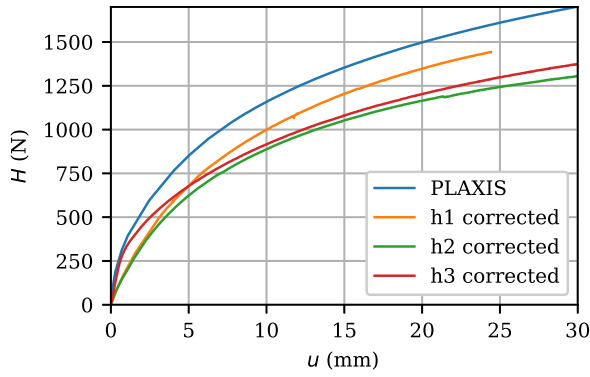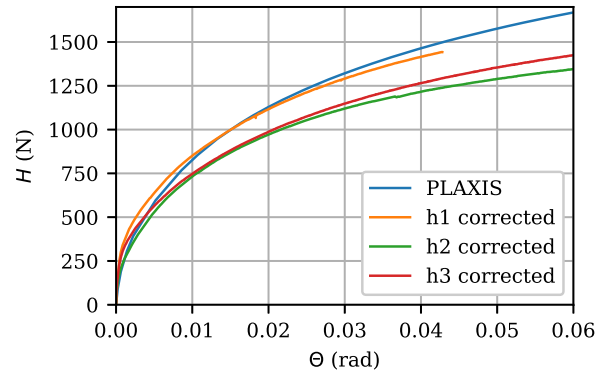| Load												
						Radial paths						
Horizontal force	H	0	2.41M	M	0.41M	-0.41M	-1.43M	-M	-2.41M	-2M	-3M	-3.73M
Moment	0	M	M	M	M	M	M	M	M	M	M	M

Chapter 4

Results

4.1 Macro model input obtained from laboratory testing and PLAXIS

4.1.1 Load-displacement curves

The input curves from the laboratory experiments (h1, h2, h3, m1 and m3 in Table 3.3) and the PLAXIS modeling are displayed below. Figure 4.1 shows the obtained $H\text{-}u$ and $H\text{-}\theta$ curves from a static pushover analysis with pure horizontal force at mudline, hereby referred to as the H-curves. Figure 4.2 shows the obtained $M\text{-}u$ and $M\text{-}\theta$ curves from a static pushover analysis with pure moment at mudline, hereby referred to as the M-curves. Single plots for each conducted laboratory test, with both raw data and corrected curves, are displayed in Figure 4.3 - 4.12. Figure (a) shows the whole curve, and figure (b) is zoomed in on the initial part of the curves.
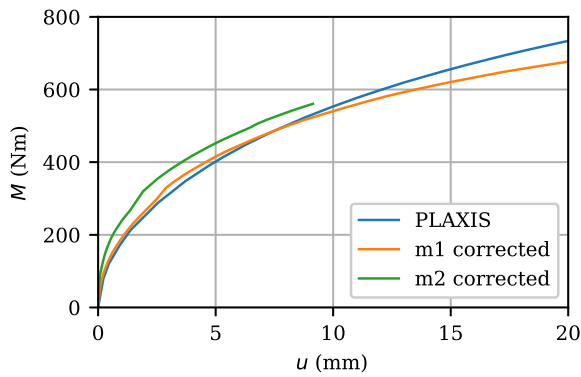
(a)

(b)

Figure 4.1: (a) Load-displacement curves for pure horizontal loading, from PLAXIS and laboratory tests h1, h2 and h3. (b) Load-rotation curves for pure horizontal loading, from PLAXIS and laboratory tests h1, h2 and h3. Force, displacement and rotation is at mudline in case of the PLAXIS model, and approximately 5cm above mudline in case of the laboratory tests.
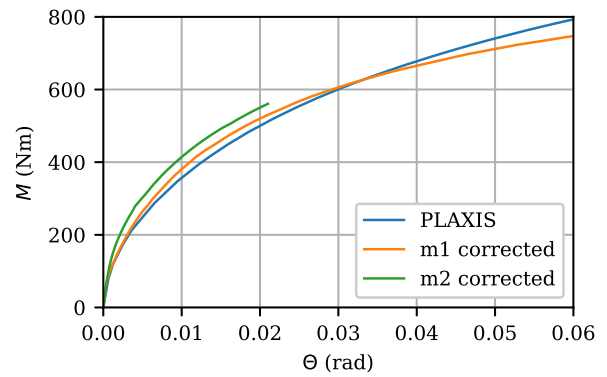

(a)

(b)

Figure 4.2: (a) Moment-displacement curves for pure moment loading, from PLAXIS and laboratory tests m1 and m2. (b) Moment-rotation curves for pure moment loading, from PLAXIS and laboratory tests m1 and m2. Moment, displacement and rotation is at mudline in case of the PLAXIS model, and approximately 5cm above mudline in case of the lab tests.

Test nr. 1 - pure horizontal force at mudline
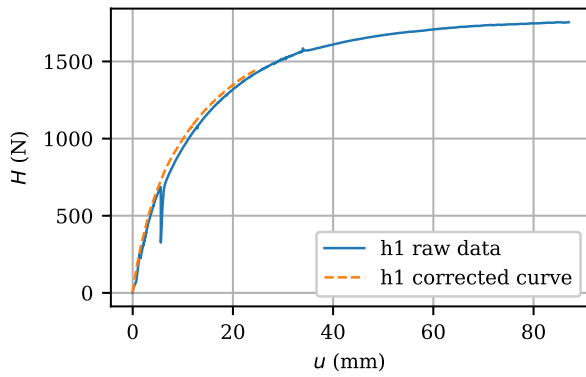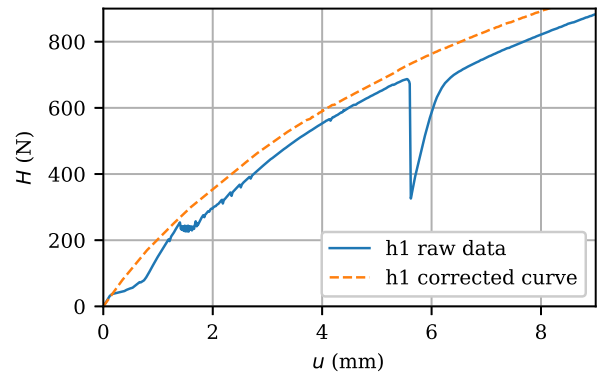
Figure 4.3: (a) Load-displacement curve for pure horizontal loading, h1. (b) Initial part of the load-displacement curve for pure horizontal loading, h1.

Figure 4.4: (a) Load-rotation curve for pure horizontal loading, h1. (b) Initial part of the load-rotation curve for pure horizontal loading, h1.
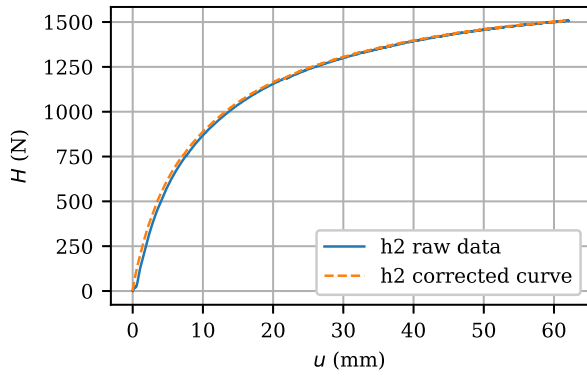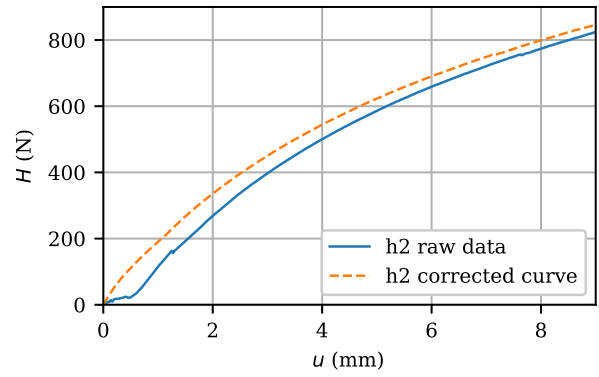
(a)   (b)

Figure 4.5: (a) Load-displacement curve for pure horizontal loading, h2. (b) Initial part of the load-displacement curve for pure horizontal loading, h2.
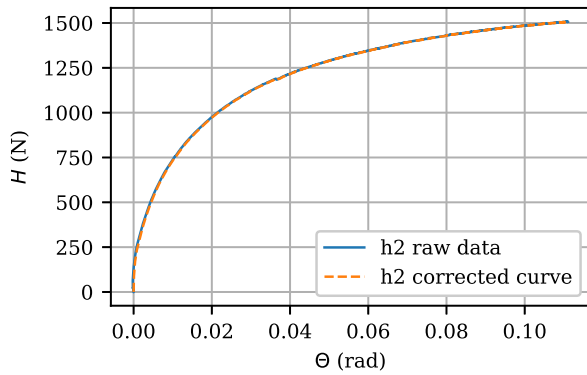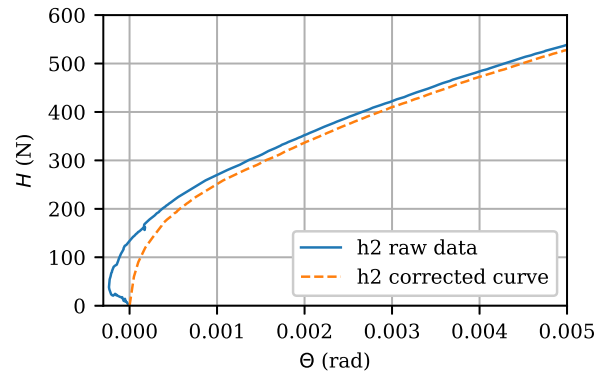
(a)   (b)

Figure 4.6: (a) Load-rotation curve for pure horizontal loading, h2. (b) Initial part of the load-rotation curve for pure horizontal loading, h2.
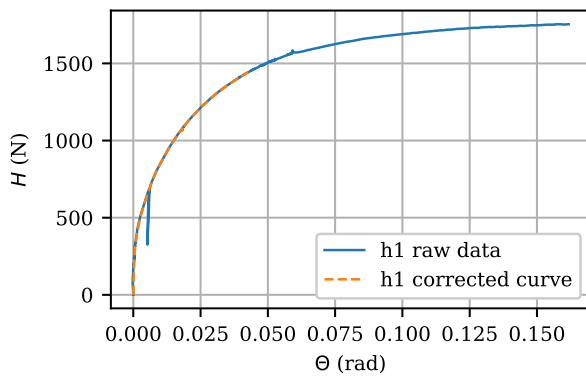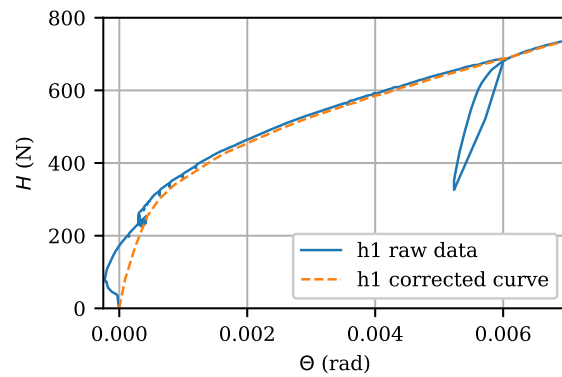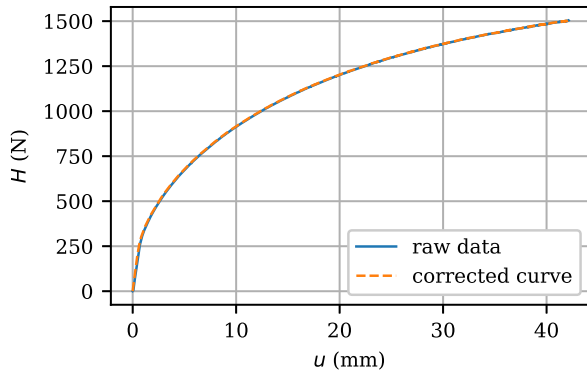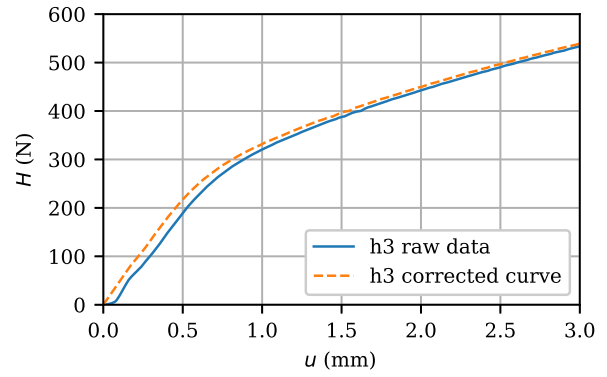
(a)　　　　　　　　　　　　　　　(b)

Figure 4.7: (a) Load-displacement curve for pure horizontal loading, h3. (b) Initial part of the load-displacement curve for pure horizontal loading, h3.
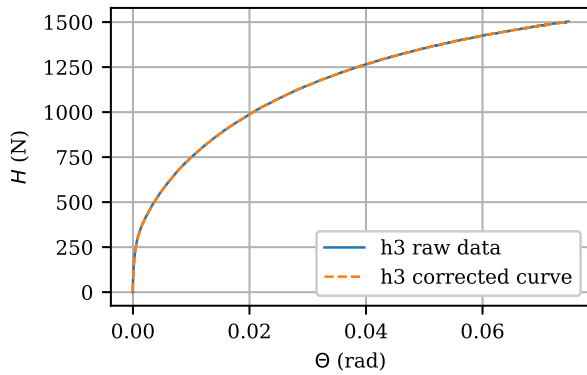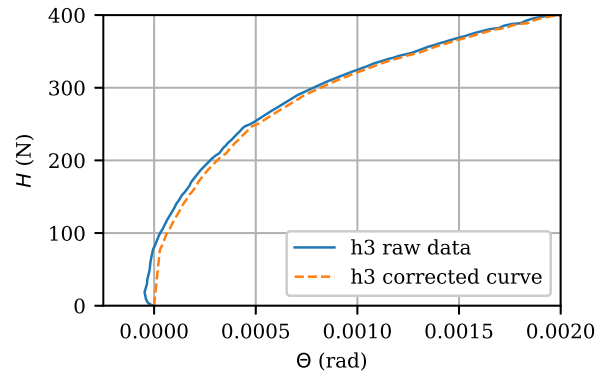
(a)　　　　　　　　　　　　　　　(b)

Figure 4.8: (a) Load-rotation curve for pure horizontal loading, h3. (b) Initial part of the load-rotation curve for pure horizontal loading, h3.

Test nr. 2 - pure moment at mudline
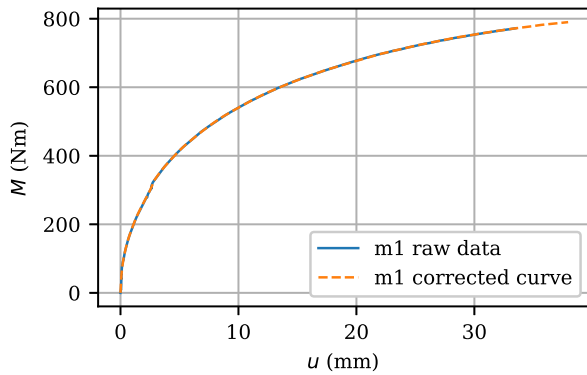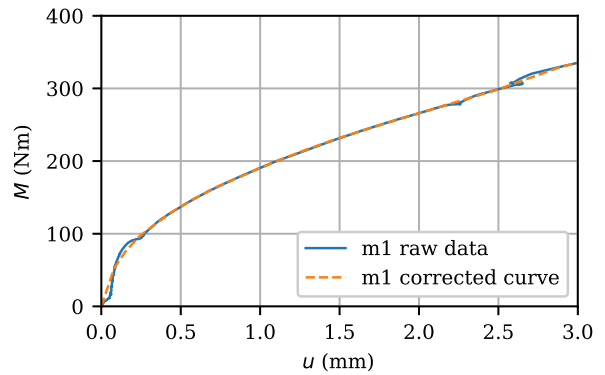
(a)   (b)

Figure 4.9: (a) Moment-displacement curve for pure moment, m1. (b) Initial part of the moment-displacement curve for pure moment, m1.
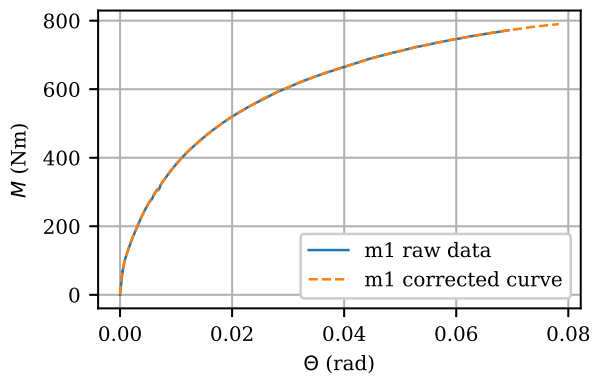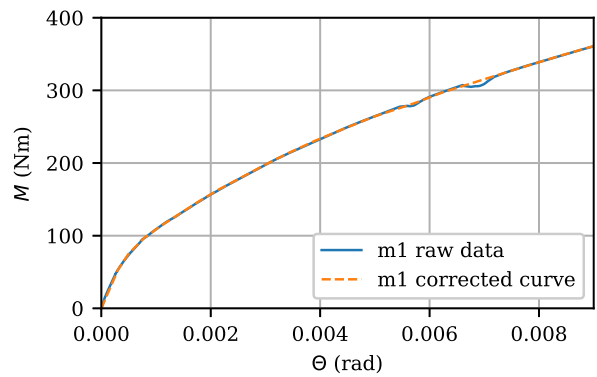
(a)   (b)

Figure 4.10: (a) Moment-rotation curve for pure moment, m1. (b) Initial part of the moment-rotation curve for pure moment, m1.
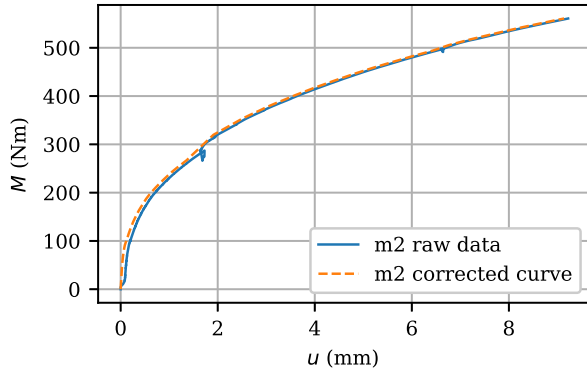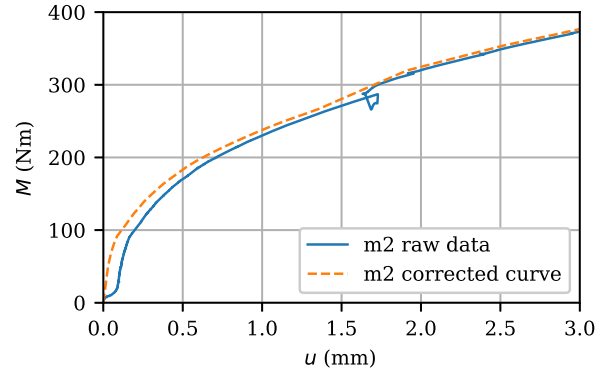
Figure 4.11: (a) Moment-displacement curve for pure moment, m2. (b) Initial part of the moment-displacement curve for pure moment, m2.
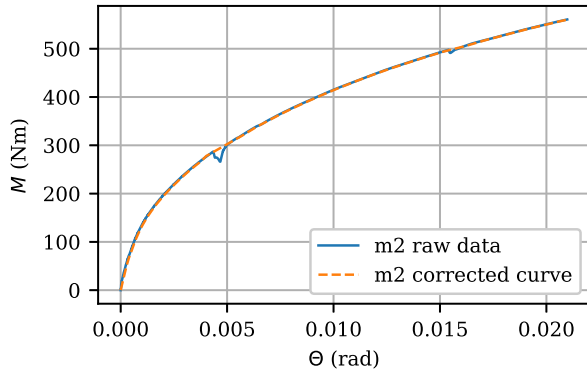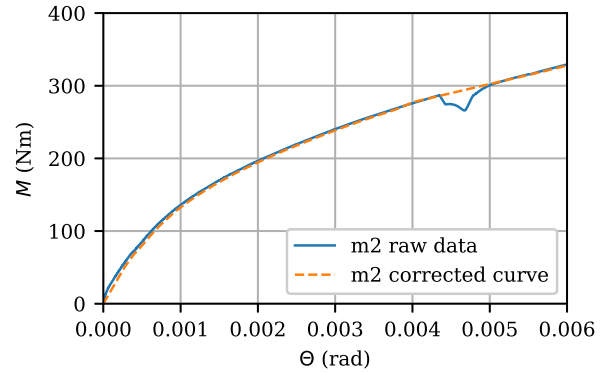
Figure 4.12: (a) Moment-rotation curve for pure moment, m2. (b) Initial part of the moment-rotation curve for pure moment, m2.

4.1.2 Stiffness matrices

Table 4.1: Stiffness matrices obtained by combining the input curves from the laboratory tests, and from PLAXIS.

			Input from					
	h1+m1	h2+m1	h3+m1	h1+m2	h2+m2	h3+m2	PLAXIS	Unit
k_{11}	245.5	290.4	497.2	235.2	279.7	483.3	2384.3	kN/m
k_{12}	-65.9	-78.0	-133.5	-25.7	-30.5	-52.7	-912.1	kN
k_{21}	-48.0	-42.0	-31.5	-48.3	-42.5	-32.2	-894.7	kN
k_{22}	186.6	185.0	182.2	187.8	187.2	186.0	458.7	kNm

4.2 Results from laboratory testing and PLAXIS with combined loading

4.2.1 Test nr. 3 - combination of loads in-plane

Figure 4.13 shows the H_x-u_x and M_y-θ_y curves for lab test mh1 (Table 3.3) and corresponding PLAXIS results. For the lab test, the horizontal force is applied 221cm above mudline, and moment, rotation and displacement are measured/calculated 5cm above mudline. Figure 4.14 shows the H_x-u_x and M_y-θ_y curves for lab test mh2 (Table 3.3) and corresponding PLAXIS results. For the lab test, the horizontal force is applied 109cm above mudline, and moment, rotation and displacement are measured/calculated 5cm above mudline.

(a)   (b)
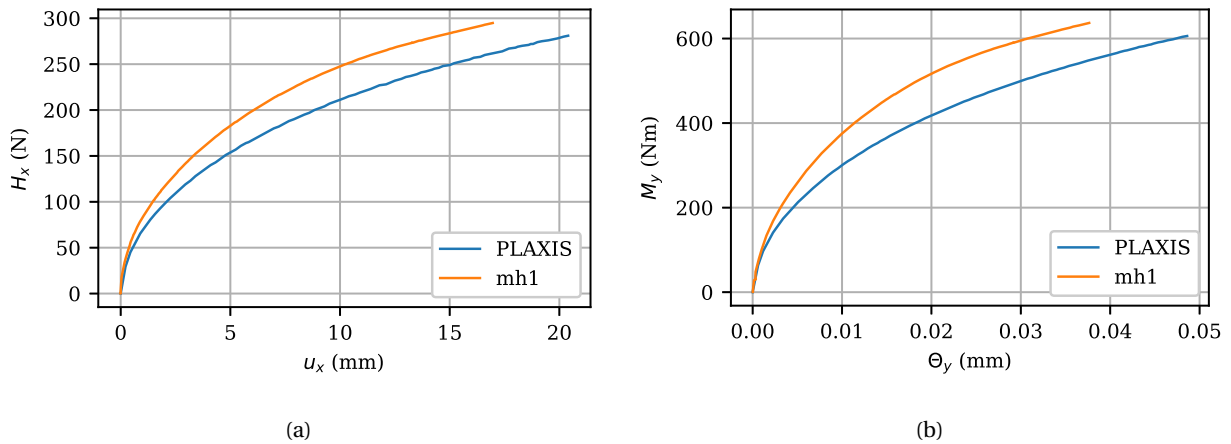
Figure 4.13: (a) Load-displacement curves for in-plane combination of loads, from PLAXIS and laboratory test mh1. (b) Moment-rotation curves for in-plane combination of loads, from PLAXIS and laboratory test mh1. The horizontal force is applied 221cm above the sand, and the moment, displacement and rotation are measured/calculated 5cm above the sand in case of the lab test.
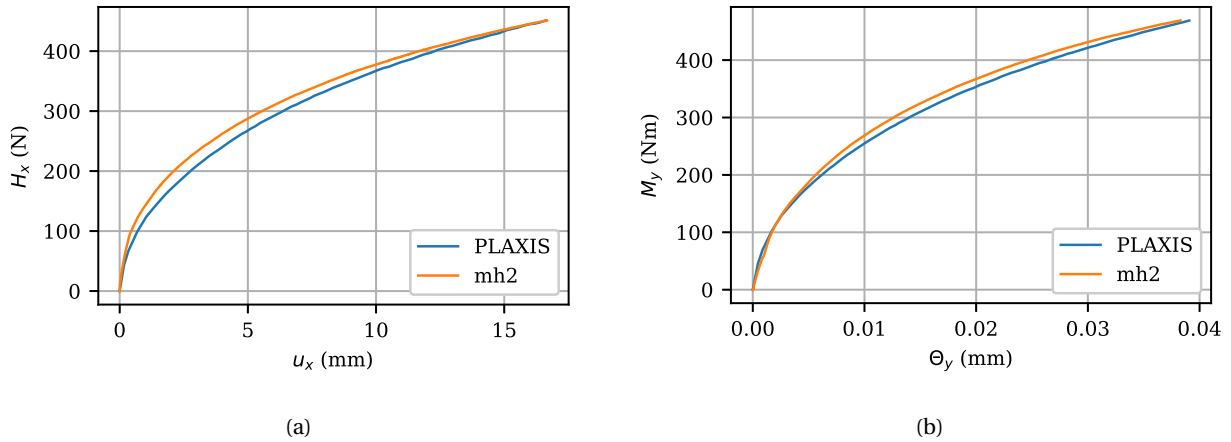
Figure 4.14: (a) Load-displacement curves for in-plane combination of loads, from PLAXIS and laboratory test mh2. (b) Moment-rotation curves for in-plane combination of loads, from PLAXIS and laboratory test mh2. The horizontal force is applied 109cm above the sand, and the displacement and rotation are measured/calculated 5cm above the sand.

4.2.2   Test nr. 4 - multidirectional loading

Figure 4.15 displays the load-displacement curves in plane and out of plane for lab test multi1 and multi2 in Table 3.3, and corresponding PLAXIS results. Figure 4.16 display the load displacement-curves for lab test multi3 in Table 3.3, and corresponding PLAXIS results. Displacements are given for the same height as the load application points. u_x is measured approximately 205cm, and u_y approximately 15cm above mudline. Exact height for each test is specified in the figure texts. Single plots with raw data, and curves corrected for second order effects as explained in subsection 3.1.2, are shown in Figure 4.17 -4.19.
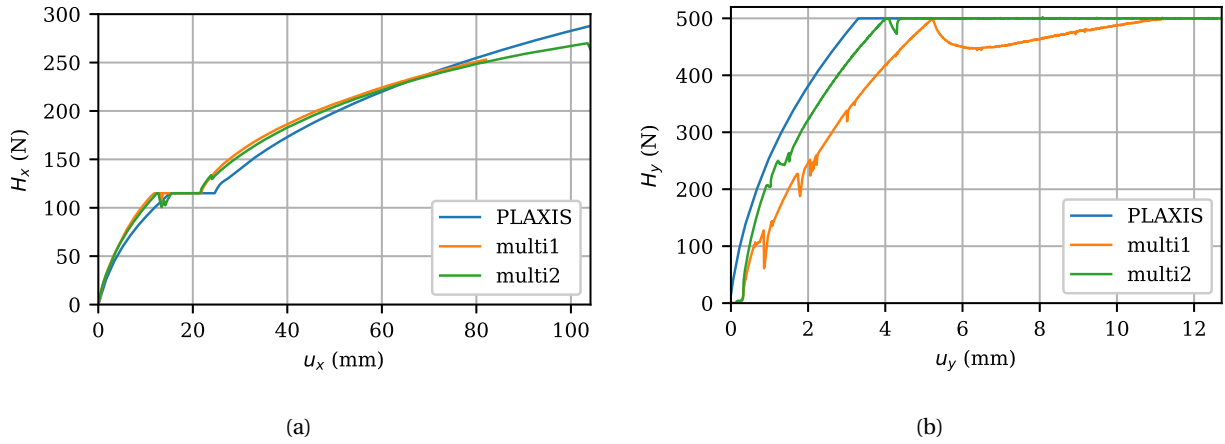
Figure 4.15: (a) Load-displacement, u_x-H_x, curves in-plane from lab and PLAXIS for the first case of multidirectional loading. (b) Load-displacement, u_y-H_y, curves out of the plane from lab and PLAXIS for the first case of multidirectional loading. NOTE that load application in the y-plane starts when $H_x = 115N$, and that further loading in the x-plane starts when $H_y = 500N$
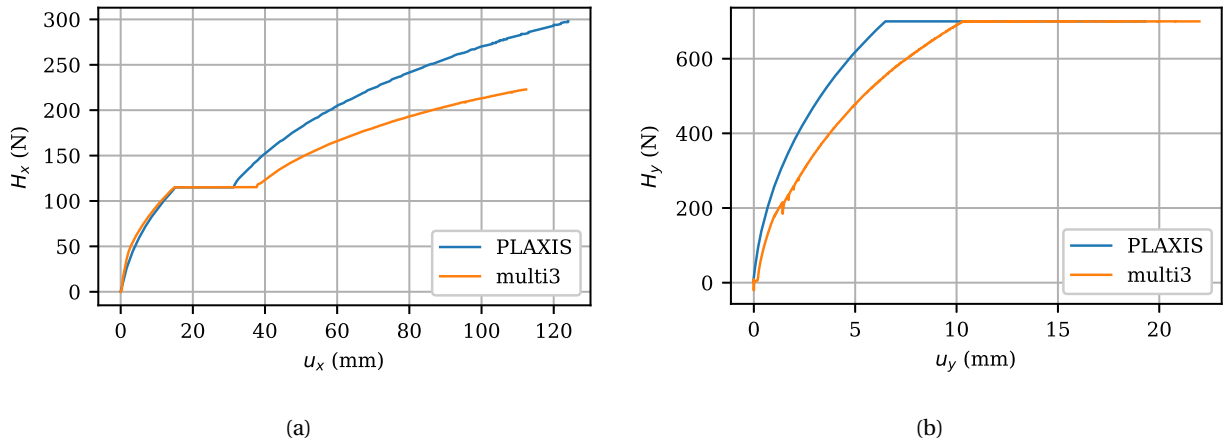
Figure 4.16: (a) Load-displacement, u_x-H_x, curves in-plane from lab and PLAXIS for the second case of multidirectional loading. (b) Load-displacement, u_y-H_y, curves out of the plane from lab and PLAXIS for the second case of multidirectional loading. NOTE that load application in the y-plane starts when $H_x = 115N$, and that further loading in the x-plane starts when $H_y = 700N$
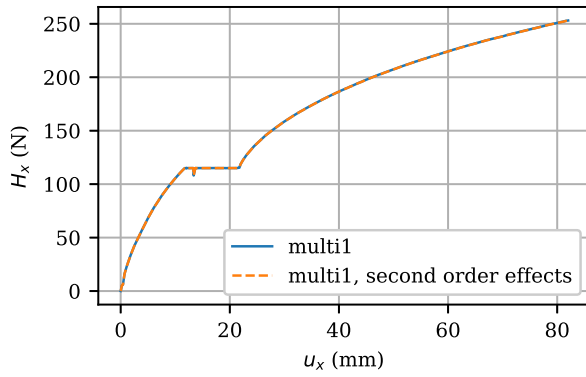
(a)
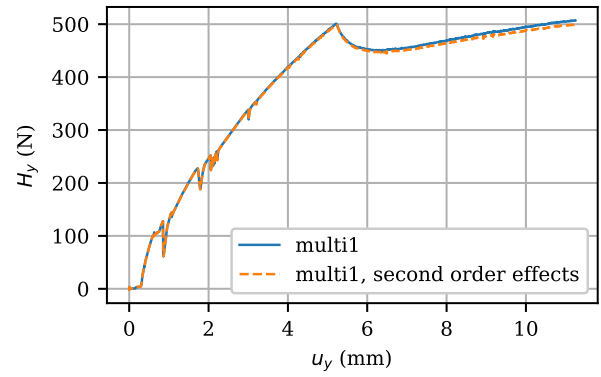
(b)

Figure 4.17: (a) Load-displacement,u_x-H_x, curve in-plane for multi1. Load and displacement measured on the pile 205cm above sand surface. Measured curve and the curve corrected for 2. order effects are shown. (b) Load displacement, u_y-H_y, curve out of plane for multi1. Load and displacement measured on the pile 15cm above sand surface. Measured curve and the curve corrected for 2. order effects are shown. NOTE that load application in the y-plane starts when $H_x = 115N$, and that further loading in the x-plane starts when $H_y = 500N$
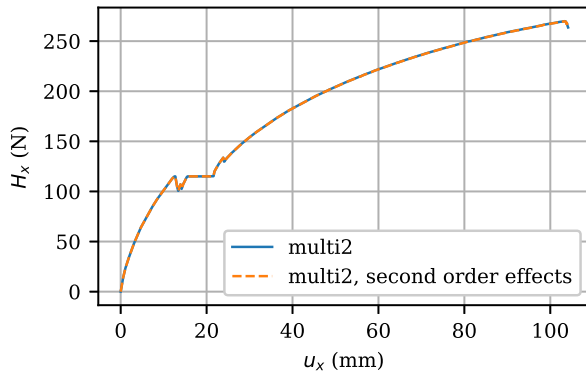
(a)
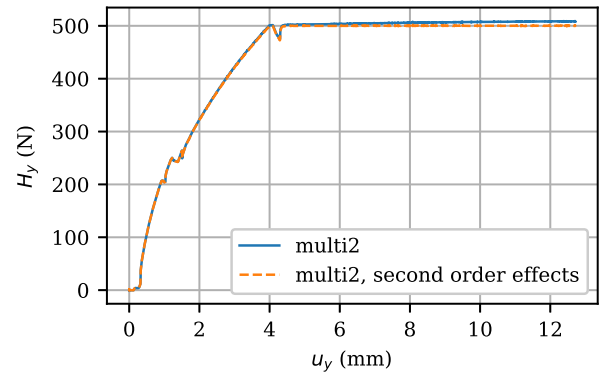
(b)

Figure 4.18: (a) Load-displacement,u_x-H_x, curve in-plane for multi2. Load and displacement measured on the pile 204cm above sand surface. Measured curve and the curve corrected for 2. order effects are shown. (b) Load displacement, u_y-H_y, curve out of plane for multi2. Load and displacement measured on the pile 12.5cm above sand surface. Measured curve and the curve corrected for 2. order effects are shown. NOTE that load application in the y-plane starts when $H_x = 115N$, and that further loading in the x-plane starts when $H_y = 500N$
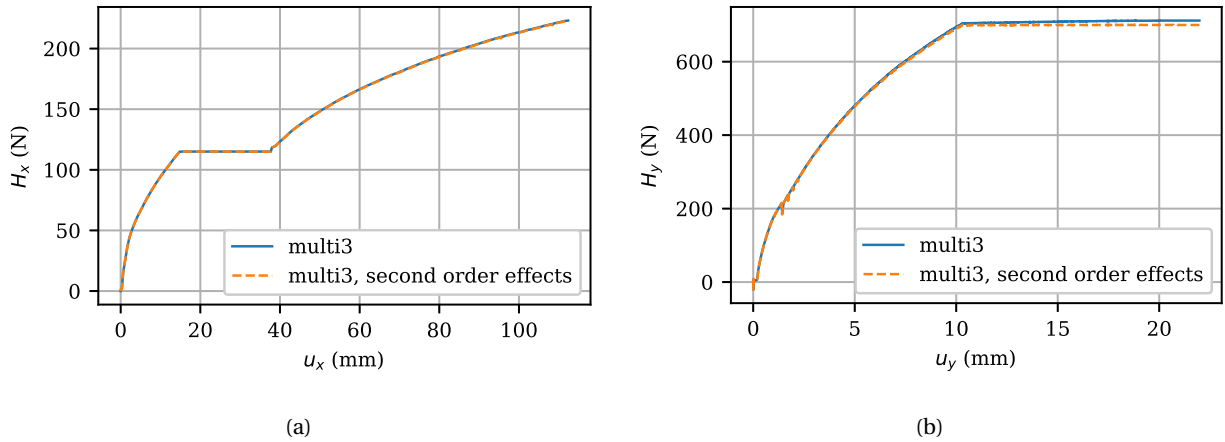
Figure 4.19: (a) Load-displacement,u_x-H_x, curve in-plane for multi3. Load and displacement measured on the pile 205cm above sand surface. Measured curve and the curve corrected for 2. order effects are shown. (b) Load displacement, u_y-H_y, curve out of plane for multi3. Load and displacement measured on the pile 14cm above sand surface. Measured curve and the curve corrected for 2. order effects are shown. NOTE that load application in the y-plane starts when $H_x = 115N$, and that further loading in the x-plane starts when $H_y = 700N$

4.3   Macro model calibration

Figure 4.20 shows contours of constant plastic work (dots) as a result of the radial load paths in PLAXIS (Table 3.6), along with the corresponding yield surfaces computed with ellipse parameters (β and b/a) from the macro model. Figure (a) shows the yield surfaces from the original macro model, whereas figure (b) shows the yield surfaces computed when adjusting the formula for β in the calibration routine to the derived formula in Appendix A1.2.

In Table 4.2, the ellipse parameters calculated by the macro model for different input are summarized.

Figure 4.21 shows the failed reproduction of the PLAXIS input curves with the macro model and the macro model with adjusted calibration routine.

Table 4.2: Ellipse parameters from the macro model calibrated with the PLAXIS and laboratory input. From original macro model, and macro model with adjusted calibration routine.

Input	Parameter	Macro model	Adjusted calibration routine
PLAXIS	β	115.8°	64.2°
	b/a	0.072	
	ϕ_u	63.6°	
	ϕ_θ	64.4°	
h1+m1	β	114.7°	65.3
	b/a	0	
	ϕ_u	65.8°	
	ϕ_θ	65.1°	
h2+m1	β	118.0°	62.0°
	b/a	0.064	
	ϕ_u	61.6°	
	ϕ_θ	62.1°	
h3+m1	β	115.5°	64.5°
	b/a	0.034	
	ϕ_u	64.4°	
	ϕ_θ	64.6°	
h1+m2	β	117.7°	62.3°
	b/a	0	
	ϕ_u	62.8°	
	ϕ_θ	62.1°	
h2+m2	β	123.4°	56.6°
	b/a	0	
	ϕ_u	56.6°	
	ϕ_θ	56.6°	
h3+m2	β	119.1°	60.9°
	b/a	0	
	ϕ_u	61.4°	
	ϕ_θ	60.8°	

Figure 4.20: (a) Contours of constant plastic work from radial load paths in PLAXIS (dots), and corresponding yield surfaces (ellipses) computed with ellipse parameters from the original macro model. (b) Contours of constant plastic work from radial load paths in PLAXIS (dots), and corresponding yield surfaces (ellipses) computed with ellipse parameters from the adjusted calibration routine in macro model. NOTE that dots and ellipses with the same color are corresponding.
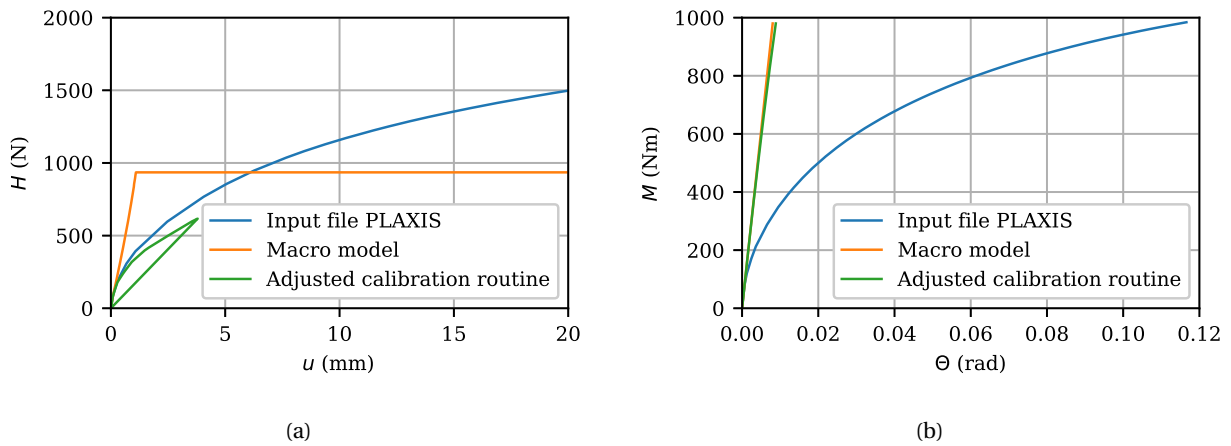
Figure 4.21: (a) Figure showing the input H-u curve from PLAXIS, and the failed reproduction of the curve with the macro model and the adjusted macro model. (b) Figure showing the input M-θ curve from PLAXIS, and the failed reproduction of the curve with the macro model and the macro model with adjusted calibration routine.

Chapter 5

Discussion

5.1 Laboratory testing

The purpose of the laboratory testing was to produce input curves for calibration of the macro model. Also to perform tests with multidirectional loading, which later could be used to verify the macro model.

5.1.1 Laboratory results, and laboratory results compared with PLAXIS

The resulting input curves from laboratory testing and from PLAXIS are presented in Figure 4.1 and 4.2 in chapter 4. Looking at the initial part of the curves in Figure 4.1, it can be seen that the curve from h3 is much stiffer than the curve for h1 and h2, but further out all three curves seem to follow a more similar pattern. All tests, except h3, were performed after the first filling of the sand bin, and the clearly stiffer initial part of the curve for h3 could be explained by that. Looking at the curves from m1 and m2 in Figure 4.2, they show matching results from two equal tests. As expected, there were variations between curves from equal tests, but they still follow the same trend. The variation is explained by local differences between sand properties. The uneven filling explained in subsection 3.1.1 may have contributed to this.

When adjusting the PLAXIS input parameters in Table 3.5 to make the PLAXIS curves match the M-curves and H-curves, it was difficult to match both. The PLAXIS H-curve was either too stiff when the M-curve was a good match, or the H-curve was a good match when the M-curve was too soft. The first option was chosen, and as seen in Figure 4.1 and 4.2, PLAXIS matches well with the lab results in case of the M-curve and show too stiff response on the H-curve. As

mentioned in section 3.2, the mesh used in PLAXIS was quite coarse. A coarse mesh will likely mean that PLAXIS overshoots the stiffness and capacity, however this effect is accounted for when choosing soil parameters to match PLAXIS and lab results.

The PLAXIS response is overall a little stiffer, which is also seen in the calculated stiffness matrices presented in Table 4.1. The stiffness matrix coefficients are in the same magnitude for all the lab input, except for case h3+m1 and h3+m2, which is explained by the clearly stiffer h3-curve. And for the PLAXIS input, the coefficients are distinctly larger.

Load deformation curves, H_x-u_x and M_y-θ_y for the in-plane load combinations from lab tests and PLAXIS are shown in Figure 4.13 and 4.14. The PLAXIS calculations match very well for test mh2, and reasonably well for mh1. It is worth noticing that in case of mh1, the PLAXIS response is softer than the lab response. A possible explanation is that PLAXIS chooses the wrong failure mode, which could be a consequence of the coarse mesh.

Load deformation curves from the first case of multidirectional load test with both PLAXIS and lab results are shown in Figure 4.15. The curves for multi1 and multi2, which is the same test performed twice, show a similar response in-plane (Figure 4.13a), but out of plane the response measured in multi 1 is a little softer (Figure 4.13b). This is explained by the actuator applying load out of the plane failing to constantly increase the load until 500N. The curve clearly shows several load drops at 100N and 200N, and was likely caused by slack in the system. The curves from PLAXIS matches very well with the lab results for multi1 and multi2. The load displacement curves from the second case of multidirectional load test are shown in Figure 4.16. In this case, the PLAXIS curves show a little stiffer response out of the plane, and during the second loading in-plane.

Single plots of the load deformation curves from multidirectional load tests are shown in Figure 4.17-Figure 4.19. The raw data and the curves corrected for second order effects are shown, and it is visible that the second order effect is negligible.

5.1.2 About the practical execution of the tests

To perform static pushover analyses with pure horizontal loading and pure moment applied at mudline was a challenge. Practical reasons made it hard to apply load directly at mudline, and the load had to be applied a few cm above in case of the pure horizontal loading. This resulted in a combination of horizontal force and moment. However, simulations performed in PLAXIS

with load applied at mudline and 10cm above, suggest that the small eccentricity does not affect the results any more than the local variations in sand properties. In case of the pure moment as described in subsection 3.1.2, the LabView program steered the two actuators so that they always struggled to achieve the same force. However, there would always be a difference between the load in the two actuators and that gave a combination of both moment and horizontal force. At higher load levels, the difference would be insignificant, because the horizontal force would be very small compared to the moment. On the initial part of the curve it might have been of importance, but again, PLAXIS simulations with pure moment applied at mudline matched well with the lab results, and the difference is considered insignificant.

When using two actuators for load application, it was challenging to achieve the wanted forces in both actuators. In the tests with pure moment when the upper actuator was pushing, the lower actuator had to release in order to not get too high tension force. It was tricky to set the settings so that the lower actuator was able to release fast enough. The same issue was encountered in the multidirectional load test. When the upper actuator applied load in-plane on the second loading, the lower actuator struggled to uphold a constant force, because it could not adjust fast enough. That is seen in the results from multi1 (Figure 4.17b). Even though there were some struggles with the load application, they were eventually solved and the experiments have proven that the test setup worked well to perform the tests conducted.

5.1.3 Macro model input from the lab tests

The method used to calculate the elastic stiffness matrix is based on the beginning of the input curves. That makes it crucial to get the initial part of the curve correct. The initial part of the input curves from laboratory testing are not very smooth, as seen in Figure 4.3b-4.12b. It is influenced by the sensitivity of the load application procedure and data measuring. Therefore, a few points were fitted to the beginning of all input curves, to make them smoother. The smoothing might have caused a wrong calculation of the elastic stiffness matrices. Data was recorded every second, which made the curves have some thousand points. Since the macro model only supports 200 lines on the input curves, the rest of the curves also had to be processed. The smoothed curves are also shown in Figure 4.3 - 4.12.

5.1.4   Sources of error

The sources of error in the laboratory testing are listed below and discussed.

- Repetition of the same tests suggest local variations of sand properties. When looking at the results from the tests with pure horizontal load, there is difference in stiffness and capacity. Other effects such as pile installation effects and different eccentricity of the load, 5cm, 8cm and 10cm respectively, also contribute to the differences in the load displacement curves. But they should not effect the results as much as observed. This difference between the load displacement curves is therefore believed to mainly be explained by local variations in the sand.

- Rotation is not measured, but calculated from measured displacements. Uncertainties in the displacements are therefore transferred to the rotation and increased.

- The load eccentricity during the tests with pure horizontal load caused an acting moment as well. However, this eccentricity is neglected in the input curves to the macro model. It is considered acceptable because PLAXIS calculations show that the eccentricity does not affect the input curves any more than the local variations in the sand properties.

- During installation of the pile and the actuators, there were disturbances in the sand due to driving of the pile, dropping av tools, touching of the sand and disturbing the pile when installing the actuators, etc. This may have contributed to change and cause varying sand properties at the testing spots.

- The sand bin was filled up unevenly the first time, as explained in subsection 3.1.1, and this may have caused increased variation in sand properties around the pile in each test. The optimal conditions would have been a straight sand surface around the pile during testing, but this was not the case in all the tests.

- The pile was not purely vertically installed in all tests, as this was difficult to achieve when driving the pile by hand.

- Two different load cells were used in the tests when multiple actuators applied load. They required different calibration and this may have caused differences in the recordings of load.

- In the first test with pure horizontal load, there was a slip in the system, causing a load drop. As described in subsection 3.1.2, part of the load displacement curve was cut off to account for this slip. Due to the slip, the measured displacements might be wrong.

- In test h1, the horizontal displacement measured higher up on the pile was done in a poor way as Figure 5.1 illustrates. The measured deformation was done in an increasingly non horizontal direction due to the angle between string and screw. This inaccuracy is transferred to the the rotation calculations. However, this inaccuracy is expected to be negligible. For the next test, the screw was replaced with a shorter one, so that the thread could be fastened almost directly to the pile.

Figure 5.1: Picture illustrating the angle between string pot and pile.

- The elastic response of the support frame which the actuators pulled against to apply load was investigated. However, calculations suggest the elastic response to be insignificant.

- Due to repeated testing of the pile, plastic deformations of the pile could have occurred, but calculations suggest that there were no plastic deformation.

- A leveler was used to check if the actuators was installed horizontally, but there might have been a reading error. The effect of this is expected to be insignificant.

- In the tests with multidirectional loading, it was not measured if the actuators were placed orthogonal. Therefore, the assumed x-plane and y-plane may not be exactly at right angles. The possible effect of this is not accounted for, but assumed insignificant. Calculated

second order effects, which were small, in the same tests due to loading suggest that it is a fair assumption.

5.2   Using the macro model

5.2.1   Macro model input

When using the macro model, one has to be cautious about the input. In addition to making sure that the input curves are monotonically increasing, as mentioned in section 2.2, there are a few more aspects one should be aware of.

A discovery made when looking into the macro model code, is that the input load-displacement curves must have more points than the number of yield surfaces chosen. If not, the model struggles to calculate the plastic stiffness of each yield surface during calibration of the multisurface plasticity model. The model also struggles to calculate the plastic stiffness of the yield surfaces if there are several points in the pure elastic part of the input curves.

The input curves should also extend to a similar displacement and rotation. The macro model cuts off one of the input curves, so that they extend to the same lateral displacement. The moments or horizontal force on the curve that is cut off, are then interpolated from the displacements on the other curve. Moments or horizontal forces are also interpolated from the rotations on the curve that is not cut off. If the H-curve has been cut off, the interpolation routine could end up interpolating outside the input range and the calibration fails. This could happen because for a given plastic displacement, the corresponding plastic rotation on the M-curve is bigger than that on the H-curve.

5.2.2   Calibration issues

The input generated from the laboratory experiments and the PLAXIS modeling are presented in section 4.1. The ellipse parameters and contour angles computed with the macro model with this input are presented in Table 4.2.

From Table 4.2 it can be seen that for some combinations of input from the laboratory testing, the macro model produced $b/a = 0$ which makes the calibration fail. $b/a = 0$ occurs when the contour angle of plastic displacements, ϕ_u, is bigger than that of plastic rotations, ϕ_θ. Physically it means that for the given input, the same plastic displacement caused by pure moment

and pure horizontal force will in the case of pure horizontal force have a larger corresponding plastic rotation than the pure moment case. It should be the other way around. The reason why this happens could be explained by local differences in the sand where the tests have been performed. It could be that the H-curve from one spot in the sand is not representative for the sand where the M-tests was performed. Another explanation is that the plastic rotations on the input M-curve are underestimated, due to an unsuitable elastic stiffness matrix.

The ellipse rotation angle, β, was in all cases larger than 90°. A consequence of $\beta > 90°$ is that the input curves shifted to transformed load space could end up with negative displacements, which again causes trouble when calculating the stiffness of the yield surfaces (see Figure A1.1 in Appendix A1.1). Furthermore, $\beta > 90°$ does not physically makes sense because it means that the pile can resist a larger horizontal force when at the same time applying an overturning moment working in the same direction (Figure 2.4a). The opposite is expected, and was also confirmed by plotting contours of constant plastic work from radial load paths applied to the PLAXIS model. This is shown in Figure 4.20, where computed contours from PLAXIS are plotted with the corresponding yield surfaces computed with the macro model ellipse parameters. The plot suggests that the macro model calibration does not work for the tested cases, which was also confirmed by trying to reproduce the input curves. The model failed, as seen in Figure 4.21.

When using laboratory results as input, one could argue that the macro model was not calibrated with input curves from static pushover analyses with pure moment and horizontal force applied at mudline, because of the practicalities previously mentioned. However, the same calibration issue arose with the PLAXIS input, where the forces were applied exactly at mudline. The issues must hence be explained by something else.

Skau et al. (2018) mentioned in an article about a macro model for bucket foundations, that at higher load levels the contours of plastic work and hence the yield surfaces change shape and orientation. This is also repeated in Page et al. (2018). The assumption about homothetic yield surfaces may therefore not be acceptable for higher load levels. In the lab experiments, the soil was loaded to high mobilization, which is seen because the load displacement curves in subsection 4.1.1 have flattened out. As mentioned in subsection A1.2, β is calculated from the average contour angles which again are calculated from the input curves. Due to the high load levels, the calculated β could therefore be wrong. Consequently it was tested to load the PLAXIS model to approximately 10% of the load first applied (200N and 200Nm), and run the

macro model with this input. It made no difference and the problem with $\beta > 90°$ was still encountered. So yet again, the obtained rotation angles had to be explained by something else.

To explain why $\beta > 90°$, one has to look at the expression used in the macro model (Equation 2.5) repeated below:

$$\beta = \frac{\pi}{2} + \frac{1}{2} \cdot \arctan\left(\frac{2 \cdot \tan\phi_u}{\tan\phi_u \tan\phi_\theta - 1}\right)$$

It can be seen that a case where the second term will be positive, is if both $\tan\phi_u$ and $\tan\phi_\theta$ are bigger than 1. Note that $\tan\phi_u$ and $\tan\phi_\theta$ are positive by the definition and they should not be equal. If the second term is positive, β will be bigger than $\frac{\pi}{2}$ or 90°. $\tan\phi_u > 1$ and $\tan\phi_\theta > 1$ is the case when:

$$\pi \cdot n - \frac{3\pi}{4} < \phi_u < \pi \cdot n - \frac{\pi}{2}, \; n = \mathbb{Z}$$

$$\pi \cdot n - \frac{3\pi}{4} < \phi_\theta < \pi \cdot n - \frac{\pi}{2}, \; n = \mathbb{Z}$$

Since $(\phi_u, \phi_\theta) \in \langle 0, 90°\rangle$, $\tan\phi_u > 1$ and $\tan\phi_\theta > 1$ are fulfilled when:

$$45° < \phi_u < 90°$$

$$45° < \phi_\theta < 90°$$

With all tested input, the contour angles are on the interval that gives $\beta > 90°$, see Table 4.2. The macro model is accordingly not valid for the tested input. Therefore, the derivation of the ellipse parameters was conducted in order to try to find an expression for β that could work with the input.

When deriving the formulas for the ellipse parameters, another expression for β than the one used in the macro model resulted (Appendix A1.2). The expression, repeated below, has a solution for β with $\pi/2$ period.

$$\beta = \frac{1}{2}\left(\frac{2\tan\phi_u}{1 - \tan\phi_u \tan\phi_\theta}\right) + \frac{\pi \cdot n}{2}, \; n = \mathbb{Z}$$

With the altered calibration routine inside the macro model, explained in section 3.4, a condition was set to choose the solution for β on the interval $\langle 0°, 90°\rangle$. The resulting β-values from this adjusted calibration routine are also presented in Table 4.2. Figure 4.20(b) show the result-

ing ellipses for the PLAXIS input with the adjusted expression for β. The orientation is a good match with the contours computed from PLAXIS, but the axes lengths are still a poor match. Even though the calibration of the model seemed to go better with the adjusted expression for β, the model was still not able to reproduce the input curves. The innermost yield surfaces had infinite stiffness, and since the surfaces are coupled in series (Equation 10 in Appendix A1), this error propagates. The reason why this happens was not discovered. The attempted reproduction of the PLAXIS input curves are shown in Figure 4.21.

5.3 Limitations

A limiting factor about this study is the fact that laboratory testing was performed in dry sand, which is not realistic ground conditions on an OWT site. So even though the model could not be verified for the dry sand, there is still a possibility that the macro model could work for undrained sands offshore.

The testing had to be performed on a very small pile, scale 1:60, due to the capacity of the load application equipment available at the lab. The effective stresses in the sand around pile were therefore low, and this may have caused near surface scale effects. The relationships between rotations and displacements could hence be different than those for real size monopiles. Even though the model could not be verified for dry sand with this testing, it does not rule out that there are cases where the macro model could work to describe pile-soil interaction in dry sand.

Note that displacements are only measured at the load application points in the multidirectional load tests. The macro model produces the response at mudline, and should the lab results later be used to compare with this model, one has to transform the response at mudline into the response further up at the pile. Also, no rotations were recorded for the multidirectional load tests because there was no available equipment to do that, since the string pot was used to measure displacements used for second order effect calculations.

Chapter 6

Conclusions and recommendations for further work

6.1   Summary and conclusions

Laboratory load tests of a monopile with 10cm diameter, embedded 60cm in the sand was con-
ducted. It was done to generate input for a macro model that describes the pile-soil interaction
in integrated load analyses. Input in this model are load-displacement-rotation curves from
static pushover analyses with both pure horizontal force, and pure moment applied at mudline.
In addition, an elastic stiffness matrix must be provided. With the given input, the model is
calibrated and can compute the pile response caused by an applied load history. Lab tests that
could be used for comparison with predicted response from the macro model were also per-
formed. All lab tests were simulated with the FE program PLAXIS 3D for comparison. Because
the macro model struggled in the calibration routine with the tested input, this was investigated
by looking into the model code. One of the calibration parameters were adjusted in order to
improve the calibration with the tested input, but new issues occurred that were not solved.

In this thesis we set out to address the following research questions:

- Can the PLAXIS model be optimized so that the calculation results match the results from
  laboratory testing?

- Can input for the macro model successfully be generated with laboratory testing?

- Can the macro model code be verified by testing different input curves from laboratory

experiments and PLAXIS modeling?

- Is the macro model developed in the REDWIN project valid for pile-soil interaction in dry sand?

- Does the macro model predict realistic pile response to multidirectional loading

Overall the PLAXIS results were a good match with the laboratory test results. The soil parameters are representative for the sand in the laboratory, and the answer to the first research question is yes. The PLAXIS parameters were optimized so that the calculation results are a good match with the lab results.

Macro model input was successfully generated with laboratory testing, however the load-displacement curves require some processing before they can be used, and it is a tedious job. It is easier and therefore recommended to use input curves generated with an FE program like PLAXIS 3D. The lab results could instead be used to adjust the FE model so that it is representative for the laboratory conditions.

Because the macro model failed to reproduce the input curves, and the calibration failed with most of the tested input, it appears that the macro model developed in the REDWIN-project is not valid for pile-soil interaction in dry sand. It is concluded that the macro model could not be verified with different input from laboratory experiments and PLAXIS modeling, of a pile with 10cm diameter embedded 60cm in dry sand. It was not tested if the response of this pile to multidirectional loading predicted by the macro model was realistic. But since it was not able to reproduce the input, it is highly unlikely. The calibration problems were studied, and an attempt to improve the calibration routine was made. However, the model was still not able to reproduce the input curves and the reason was not identified in this thesis.

6.2   Recommendations for further work

Working with this master thesis has lead to the following objectives that could be further investigated:

- With the tested input in the macro model, the calibration was wrong or failing. It is therefore recommended to continue investigating why the calibration fails, and possibly adjust the model to make it valid for a wider range of cases.

- The macro model could not be tested against laboratory tests with multidirectional loading, due to wrong or failing calibration of the model. However, the laboratory data obtained during this work can be used to test other models that are made to describe pile-soil interaction.

- The laboratory testing was performed with a small pile due to limited capacity of the load application equipment. It would therefore be interesting to repeat the test program with a bigger pile should equipment with larger capacity be available. It could be investigated if the same calibration problems with the macro model occur if there were larger effective stresses in the sand, as it would be with a bigger pile embedded further. Larger overburden pressure in the sand could also be achieved by sealing off the sand, and apply an under-pressure with a vacuum pump as done by Hanssen (2016).

- The laboratory tests performed proved that the test setup worked well for testing of a small scale monopile. The test program can be expanded to include vertical and torsional loading.

- Only monotonic loading was performed in the experiments, but it is also possible to apply cyclic loading with the lab equipment. It is therefore recommended to apply cyclic loading for verification of the macro model in sand, should the calibration issues be solved.

Bibliography

(2018a). *PLAXIS Material Models Manual.*

(2018b). *PLAXIS Reference Manual.*

Bell, K. (2018). *Matrisestatikk - Statiske beregninger av fagverk, rammer og buer.* Fagbokforlaget, 4. edition.

Det Norske Veritas (2014). Design of Offshore Wind Turbine Structures - Offshore Standard DNV-OS-J101. DNV GL.

Grimstad, G., Rønningen, J., and Nøst, H. (2014). Use of iwan models for modelling anisotropic and cyclic behavior of clays. *Numerical Methods in Geotechnical Engineering,* pages 49–54.

Hald, T., Mørch, C., Jensen, L., Bakmar, C., and Ahle, K. (2009). Revisiting monopile design using py curves. results from full scale measurements on horns rev. In *Proceedings of European Offshore Wind 2009 Conference.*

Hanssen, S. B. (2016). *On the Determination of Spring Stiffness for Laterally Loaded Monopiles.* PhD thesis, NTNU.

Holm, I. (2019). A study of a macro model and its performance compared to FEA.

Koiter, W. (1953). Stress-strain relations, uniqueness and variational theorems for elastic-plastic materials with a singular yield surface. *Quarterly of applied mathematics,* 11(3):350–354.

Krohn, S., Morthorst, P., and Awerbuch, S. (2009). The Economics of Wind Energy.

Lieng, J. (1988). *Behaviour of laterally loaded piles in sand - Large scale model test.* PhD thesis, NTNU.

Lieng, J., Moen, T., and Senneset, K. (1984). Large Scale Model Tests - Test Facilities and Test Examples. In *NGM*, volume 3, pages 177–185, Linköping, Sweden.

Løkke, A., Page, A., and Skau, K. (2018). REDWIN - Reducing cost of offshore wind by integrated structural and geotechnical design. Technical report, NGI.

Nordal, S. (2019). Geotechnical engineering advanced course.

Page, A. (2018). *Monopile Foundation Models for Dynamic Structural Analyses of Offshore Wind Turbines*. PhD thesis, NTNU.

Page, A., Grimstad, G., Eiksund, G., and Jostad, H. (2018). A macro-element pile foundation model for integrated analyses of monopilebased offshore wind turbines. *Ocean Engineering*, 167:23–35.

Page, A., Grimstad, G., Eiksund, G., and Jostad, H. (2019). A macro-element model for multidirectional cyclic lateral loading of monopiles in clay. *Computers and Geotechnics*, 106:314–326.

Shadlou, M. and Bhattacharya, S. (2016). Dynamic stiffness of monopiles supporting offshore wind turbine generators. *Soil Dynamics and Earthquake Engineering*, 88:15–32.

Skau, K., Grimstad, G., Page, A., Eiksund, G., and Jostad, H. (2018). A macro-element for integrated time domain analyses representing bucket foundations for offshore wind turbines. *Marine Structures*, 59:158–178.

Søvik, M. (2017). Macro-model description and model verification.

Tadesse, S. (2000). *Behaviour of saturated sand under different triaxial loading and liquefaction*. PhD thesis, NTNU.

Tefera, T., Grande, L., and Athanasiu, C. (2006). Large scale model test on single strutted sheet pile wall in sand. In *ICPMG*.

Tistel, J. (2018). *Bridge Foundations at Large Water Depths*. PhD thesis, NTNU.

Wind Europe (2020). Offshore Wind in Europe - key trends and statistics 2019.

Zaaijer, M. (2006). Foundation modelling to assess dynamic behaviour of offshore wind turbines. *Applied Ocean Research*, 28:45–57.

Appendix

A1   Macro model

A1.1   Model formulation and calibration

Here follows a more thorough description of some of the macro model components.

The flow rule determines the direction of plastic flow, or incremental plastic displacements. It is defined as the gradient to the plastic potential surface, g (Equation 1). Since an associated flow rule is chosen, the plastic potential surfaces are the same as the yield surfaces.

$$d\boldsymbol{v}^p = d\lambda \cdot \frac{\partial g}{\partial \boldsymbol{t}} \tag{1}$$

To calculate the incremental plastic displacements, $d\boldsymbol{v}^p$, the contributions from all active yield surfaces are summed up, following Koiter's rule (Koiter, 1953) in Equation 2. In the equation, j is the number of yield surfaces translating in load space, and $d\lambda_i$ is an incremental multiplier defining the size of $d\boldsymbol{v}^p$ (Page et al., 2019).

$$d\boldsymbol{v}^p = \sum_{i=1}^{j} d\boldsymbol{v}_i^p = \sum_{i=1}^{j} d\lambda_i \cdot \frac{\partial f_i}{\partial \boldsymbol{t}} \tag{2}$$

The kinematic hardening rule from Grimstad et al. (2014) was chosen for the macro model, and it determines the translation, $d\boldsymbol{\alpha}_i$, of the i'th yield surface center, following Equation 3. The plastic stiffness matrix, $\boldsymbol{K}_i^p$ in the equation is defined as the ratio between $(\boldsymbol{t} - \boldsymbol{\alpha}_i)$ and $d\boldsymbol{v}^p$, and is constant for each yield surface resulting in piecewise linear hardening curves (Page et al., 2019).

$$d\boldsymbol{\alpha}_i = \boldsymbol{K}_i^p \cdot d\boldsymbol{v}^p = d\lambda_i \cdot \boldsymbol{K}_i^p \cdot \frac{\partial f_i}{\partial \boldsymbol{t}} \tag{3}$$

In order to find $d\lambda_i$ for each yield surface, a consistency condition is needed in addition to the flow rule and the hardening law. The consistency condition is defined in Equation 4,

$$\boldsymbol{f} = \begin{bmatrix} f_1 \\ f_2 \\ \vdots \\ f_j \end{bmatrix} \approx \begin{bmatrix} a_{11} + A_1 & a_{12} & \cdots & a_{1j} \\ a_{21} & a_{22} + A_2 & \cdots & a_{2j} \\ \vdots & \vdots & \ddots & \vdots \\ a_{j1} & a_{j2} & \cdots & a_{jj} + A_j \end{bmatrix} \cdot \begin{bmatrix} d\lambda_1 \\ d\lambda_2 \\ \vdots \\ d\lambda_j \end{bmatrix} \tag{4}$$

where a_{ik} is defined in Equation 5 and A_k is defined in Equation 6. $\boldsymbol{K}$ is the elastic stiffness

matrix determining the elastic response of the pile, and the matrix elements depend on soil and pile properties (Page et al., 2019).

$$a_{ik} = \left(\frac{\partial f_i}{\partial t}\right)^T \cdot \boldsymbol{K} \cdot \left(\frac{\partial f_k}{\partial t}\right) \tag{5}$$

$$A_k = \left(\frac{\partial f_k}{\partial t}\right)^T \cdot \boldsymbol{K}_k^p \cdot \left(\frac{\partial f_k}{\partial t}\right) \tag{6}$$

Equation 4, 5 and 6 are thoroughly derived in Skau et al. (2018).

During calibration of the macro model, parameters needed to calculate a transformation matrix, $\boldsymbol{R}$, in Equation 7, are calculated before $\boldsymbol{R}$ itself is computed.

$$\boldsymbol{t}' = \boldsymbol{R} \cdot \boldsymbol{t} = \begin{bmatrix} \sin\beta & 0 & 0 & \cos\beta \\ 0 & -\sin\beta & \cos\beta & 0 \\ 0 & -s\cdot\cos\beta & -s\cdot\sin\beta & 0 \\ -s\cdot\cos\beta & 0 & 0 & s\cdot\sin\beta \end{bmatrix} \cdot \boldsymbol{t} \tag{7}$$

$s = b/a$ determines the compression of the yield surfaces in this process, and β determines the rotation. They are decided based on the input load-plastic displacement curves, and are expressed in Equation 9 and Equation 8 respectively (Page et al., 2019).

$$\beta = \frac{\pi}{2} + \frac{1}{2} \cdot \arctan\left(\frac{2 \cdot a_1/a_3}{a_1/a_3 \cdot a_2/a_3 - 1}\right) \tag{8}$$

$$s = \left(\frac{a_1/a_3 \cdot a_2/a_3 + 1 - \sqrt{(a_1/a_3 \cdot a_2/a_3 - 1) \cdot (a_1/a_3 \cdot a_2/a_3 - 1 + 4 \cdot (a_1/a_3 \cdot a_2/a_3))}}{a_1/a_3 \cdot a_2/a_3 + 1 + \sqrt{(a_1/a_3 \cdot a_2/a_3 - 1) \cdot (a_1/a_3 \cdot a_2/a_3 - 1 + 4 \cdot (a_1/a_3 \cdot a_2/a_3))}}\right)^{1/2} \tag{9}$$

In Equation 7, $\boldsymbol{t}$ is transformed into $\boldsymbol{t}'$. After the transformation, in any radial direction, the same load-plastic displacement curve is obtained. The radius of the yield surfaces, S_i, are calculated, along with the plastic stiffness matrix, $\boldsymbol{K}_i^p = K_i^p \boldsymbol{I}$, for each yield surface. It is illustrated in Figure A1.1 how S_i and K_i^T can be derived from load-plastic displacement curves. K_i^p is then calculated assuming that the yield surfaces are connected in series, following Equation 10 (Page et al., 2019).

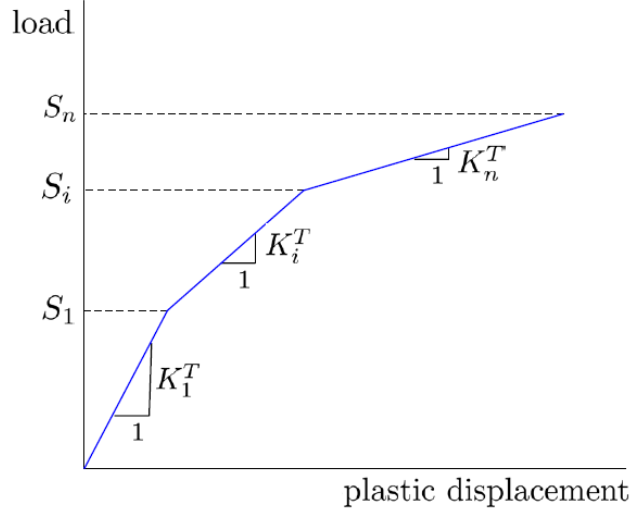$$K_i^p = \frac{1}{\frac{1}{K_i^T} - \sum_{j=1}^{i-1} \frac{1}{K_j^p}} \tag{10}$$

Figure A1.1: Calibration of the internal parameters S_i and K_i^t from load-plastic displacement curve. From Page et al. (2019).

A1.2 Derivation of the ellipse parameters

Parts of this derivation is taken from a document received from Ana Page. However, the yield surface and the contour angles were defined differently in her material. The contour angle definition given here is the one used in the macro model code.

The elliptical yield surfaces are described by the following equation:

$$f = \left(\frac{M \cdot \sin\beta + H \cdot \cos\beta}{b}\right)^2 + \left(\frac{-M \cdot \cos\beta + H \cdot \sin\beta}{a}\right)^2 - 1 = 0$$

Which to make things easier can be written as:

$$f = \left(\frac{H}{H_0}\right)^2 + \left(\frac{M}{M_0}\right)^2 + HM \cdot \frac{\gamma}{H_0 M_0} - 1 = 0$$

Assuming associated flow, the partial derivatives with respect to H, and M are equal to the incremental plastic displacement and rotation respectively:

$$du_p = \frac{\partial f}{\partial H} = \frac{2H}{H_0^2} + \frac{M\gamma}{H_0 M_0}$$

$$d\theta_p = \frac{\partial f}{\partial M} = \frac{2M}{M_0^2} + \frac{H\gamma}{H_0 M_0}$$

The ellipse parameters, β and b/a are derived from the contour angles ϕ_u and ϕ_θ, which are the

ratio between the horizontal force and moment corresponding to the same plastic displacement and plastic rotation on the input curves. They are defined in Equation 11, and the idea is displayed in Figure A1.2. The average value of all the ϕ_u^i and ϕ_θ^i are used further in the calibration. For the calibration to work, the criteria $\phi_u \leq \phi_\theta$ must be fulfilled. That makes sense, because the same plastic displacement caused by pure moment and pure horizontal force will not have the same corresponding plastic rotation. The plastic rotation caused by the moment should be bigger than the rotation caused by horizontal force.

$$\phi_u^i = \left(\frac{H_i}{M_j} \right) \text{ for } u_p^i = u_p^j \tag{11a}$$

$$\phi_\theta^i = \left(\frac{H_i}{M_j} \right) \text{ for } \theta_p^i = \theta_p^j \tag{11b}$$
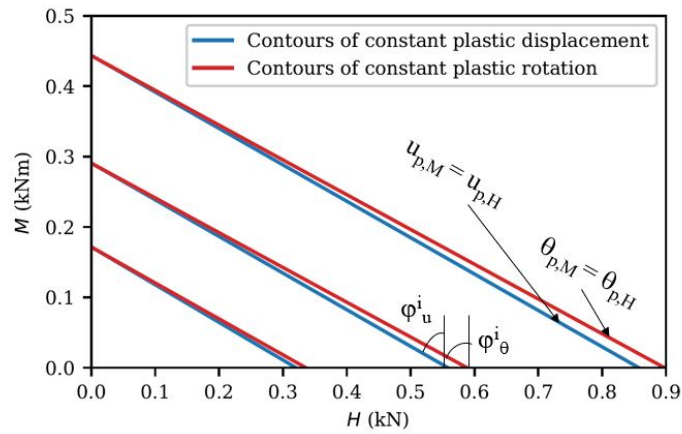

Figure A1.2: Figure displaying the concept of contours of constant plastic rotations and displacements.

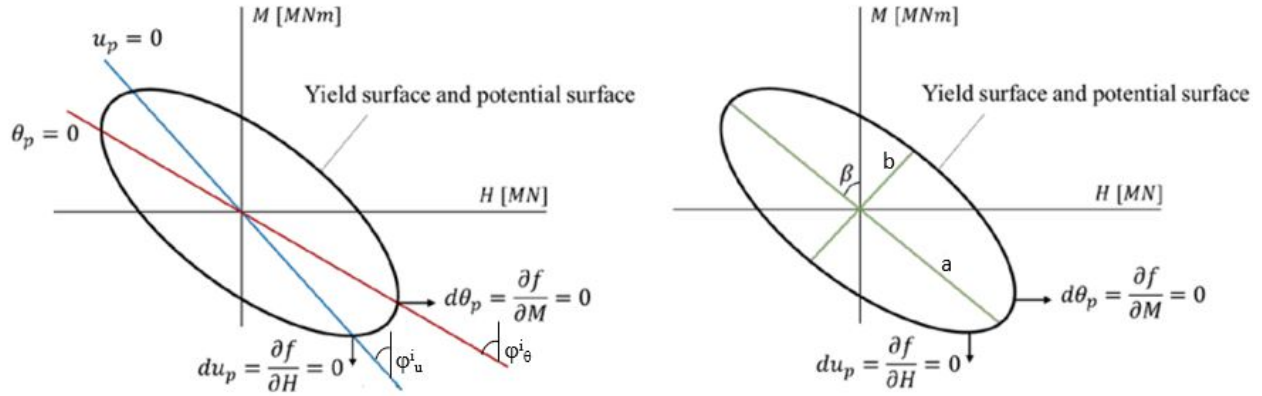Figure A1.3 show how the contour angles are connected to the ellipse.

Figure A1.3: Figure showing the connection between the contour angles and the ellipse parameters. The figure is taken from correspondence with Ana Page, and has been adjusted slightly.

Along a line defined by $H = -M \cdot \tan\phi_u$, plastic displacements are zero, $u_p = 0$, which means that $du_p = 0$. From the previous expression for du_p:

$$du_p = \frac{2H}{H_0^2} + \frac{M\gamma}{H_0 M_0} = \frac{-2M\tan\phi_u}{H_0^2} + \frac{H\gamma}{H_0 M_0} = 0$$

Leading to:

$$\frac{2\tan\phi_u}{H_0} = \frac{\gamma}{M_0} \implies \frac{H_0}{M_0} = \frac{2\tan\phi_u}{\gamma}$$

Similarly along a line defined by $H = -M \cdot \tan\phi_\theta$, plastic rotations are zero, $\theta_p = 0$, which means that $d\theta_p = 0$:

$$d\theta_p = \frac{2M}{M_0^2} + \frac{H\gamma}{H_0 M_0} = \frac{2M}{M_0^2} - \frac{M\gamma\tan\phi_\theta}{H_0 M_0} = 0$$

Leading to:

$$\frac{2}{M_0} = \frac{\gamma\tan\phi_\theta}{H_0} \implies \frac{H_0}{M_0} = \frac{\gamma\tan\phi_\theta}{2}$$

Setting the two expressions for H_0/M_0 equal each other leads to:

$$\frac{\gamma\tan\phi_\theta}{2} = \frac{2\tan\phi_u}{\gamma} \implies \gamma = \pm 2\sqrt{\frac{\tan\phi_u}{\tan\phi_\theta}}$$

which again leads to:

$$\frac{H_0}{M_0} = \frac{\pm 2\sqrt{\frac{\tan\phi_u}{\tan\phi_\theta}}}{2} \cdot \tan\phi_\theta = \pm\sqrt{\tan\phi_u \cdot \tan\phi_\theta}$$

Now the coefficients in the alternative yield criterion are expressed in terms of the contour an-

63

gles, and we can continue on the way to express the ellipse parameters in terms of the contour angles. The initial yield criterion can be rewritten as:

$$f = M^2 \left(\frac{\sin^2 \beta}{b^2} + \frac{\cos^2 \beta}{a^2} \right) + M^2 \left(\frac{\cos^2 \beta}{b^2} + \frac{\sin^2 \beta}{a^2} \right) + 2MH \cos \beta \sin \beta \left(\frac{1}{b^2} - \frac{1}{a^2} \right) - 1 = 0$$

Setting the terms after M^2, H^2 and HM in both forms of the yield criterion equal to each other gives:

$$\frac{1}{M_0^2} = \frac{\sin^2 \beta}{b^2} + \frac{\cos^2 \beta}{a^2} = \frac{\sin^2 \beta}{b^2} + \frac{\cos^2 \beta}{a^2} + \frac{\sin^2 \beta}{a^2} - \frac{\sin^2 \beta}{a^2} = \frac{1}{a^2} \cos 2\beta + \sin^2 \beta \left(\frac{1}{b^2} + \frac{1}{a^2} \right)$$

$$\frac{1}{H_0^2} = \frac{\cos^2 \beta}{b^2} + \frac{\sin^2 \beta}{a^2} = \frac{\cos^2 \beta}{b^2} + \frac{\sin^2 \beta}{a^2} + \frac{\sin^2 \beta}{b^2} - \frac{\sin^2 \beta}{b^2} = \frac{1}{b^2} \cos 2\beta + \sin^2 \beta \left(\frac{1}{b^2} + \frac{1}{a^2} \right)$$

$$\implies \frac{1}{H_0^2} - \frac{1}{M_0^2} = \cos 2\beta \left(\frac{1}{b^2} - \frac{1}{a^2} \right)$$

$$\frac{\gamma}{H_0 M_0} = 2 \cos \beta \sin \beta \left(\frac{1}{b^2} - \frac{1}{a^2} \right) = \sin 2\beta \left(\frac{1}{b^2} - \frac{1}{a^2} \right)$$

Now in the final step to find an expression for β, the two above expressions are divided by each other:

$$\frac{\frac{\gamma}{H_0 M_0}}{\frac{1}{H_0^2} - \frac{1}{M_0^2}} = \frac{\sin 2\beta \left(\frac{1}{b^2} - \frac{1}{a^2} \right)}{\cos 2\beta \left(\frac{1}{b^2} - \frac{1}{a^2} \right)}$$

$$\tan 2\beta = \frac{\gamma}{H_0 M_0} \cdot \frac{1}{\left(1 - \left(\frac{H_0}{M_0} \right)^2 \right) / H_0^2}$$

$$\tan 2\beta = \gamma \frac{H_0}{M_0} \cdot \frac{1}{1 - \left(\frac{H_0}{M_0} \right)^2}$$

H_0 / M_0 and γ expressed by the contour angles are inserted:

$$\tan 2\beta = \gamma \cdot \frac{2 \tan \phi_u}{\gamma} \cdot \frac{1}{1 - \left(\frac{2 \tan \phi_u}{\gamma} \right)^2} = \dots$$

$$\tan 2\beta = \frac{2\tan\phi_u}{1 - \tan\phi_u \tan\phi_\theta}$$

$$\beta = \frac{1}{2}\left(\frac{2\tan\phi_u}{1 - \tan\phi_u \tan\phi_\theta}\right) + \frac{\pi \cdot n}{2}, \; n = \mathbb{Z}$$

To maintain that the capacity when applying a horizontal force will increase if at the same time applying a counteracting moment, β must be on the interval:

$$0 \le \beta \le \frac{\pi}{2}$$

It is worth mentioning that the derived expression for β is not exactly the same as the one used in the macro model. The macro model uses this expression:

$$\beta = \frac{\pi}{2} - \frac{1}{2}\left(\frac{2\tan\phi_u}{1 - \tan\phi_u \tan\phi_\theta}\right)$$

Now it remains to derive the expression for the ratio between the ellipse axes, b/a. From earlier:

$$\frac{1}{M_0^2} = \frac{a^2 \sin^2\beta + b^2 \cos^2\beta}{a^2 b^2} \implies a^2 b^2 = (a^2 \sin^2\beta + b^2 \cos^2\beta) \cdot M_0^2$$

$$\frac{1}{H_0^2} = \frac{a^2 \cos^2\beta + b^2 \sin^2\beta}{a^2 b^2} \implies a^2 b^2 = (a^2 \cos^2\beta + b^2 \sin^2\beta) \cdot H_0^2$$

Two expressions for $a^2 b^2$ leads to:

$$H_0^2(a^2 \cos^2\beta + b^2 \sin^2\beta) = M_0^2(a^2 \sin^2\beta + b^2 \cos^2\beta)$$

Dividing by a^2 gives:

$$H_0^2\left(\cos^2\beta + \frac{b^2}{a^2}\sin^2\beta\right) = M_0^2\left(\sin^2\beta + \frac{b^2}{a^2}\cos^2\beta\right)$$

$$\frac{b}{a} = \sqrt{\frac{H_0^2 \cos^2\beta - M_0^2 \sin^2\beta}{M_0^2 \cos^2\beta - H_0^2 \sin^2\beta}}$$

Dividing denominator and numerator inside the square root sign with $M_0^2 \cos^2 \beta$:

$$\frac{b}{a} = \sqrt{\frac{\left(\frac{H_0}{M_0}\right)^2 - \tan^2 \beta}{1 - \left(\frac{H_0}{M_0}\right)^2 \cdot \tan^2 \beta}}$$

Inserting $H_0 / M_0 = \pm\sqrt{\tan \phi_u \tan \phi_\theta}$ gives the final expression:

$$\frac{b}{a} = \sqrt{\frac{\tan \phi_u \tan \phi_\theta - \tan^2 \beta}{1 - \tan \phi_u \tan \phi_\theta \tan^2 \beta}}$$

The ratio b/a is the same derived here and in the macro model, however it is expressed with only the contour angles and not with β in the macro model.

A2 Laboratory experiments

A2.1 Test setup

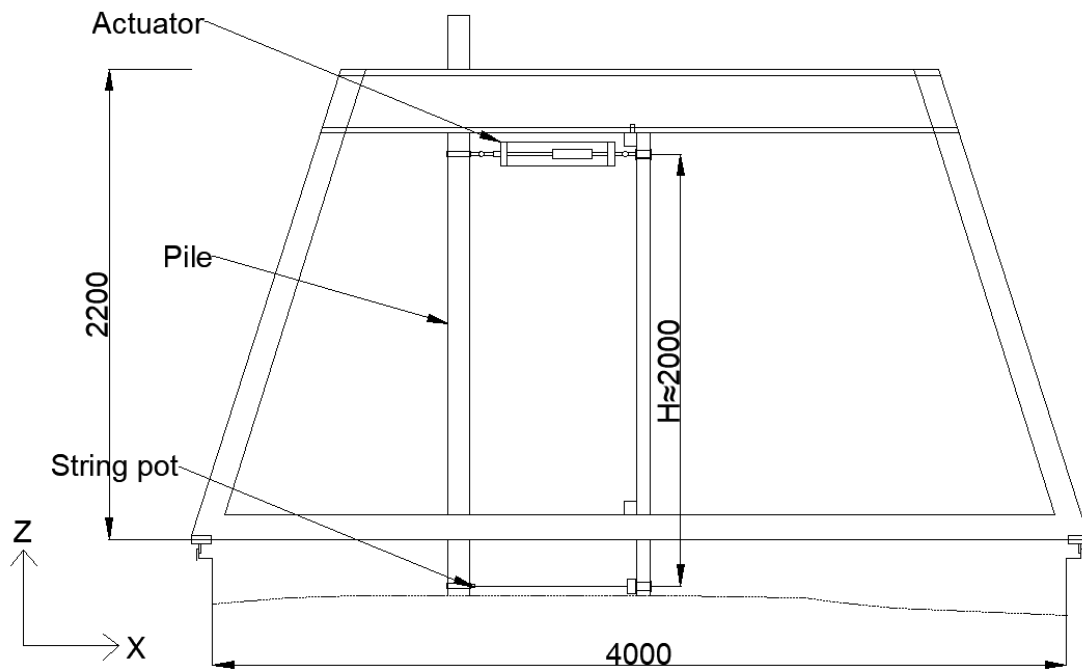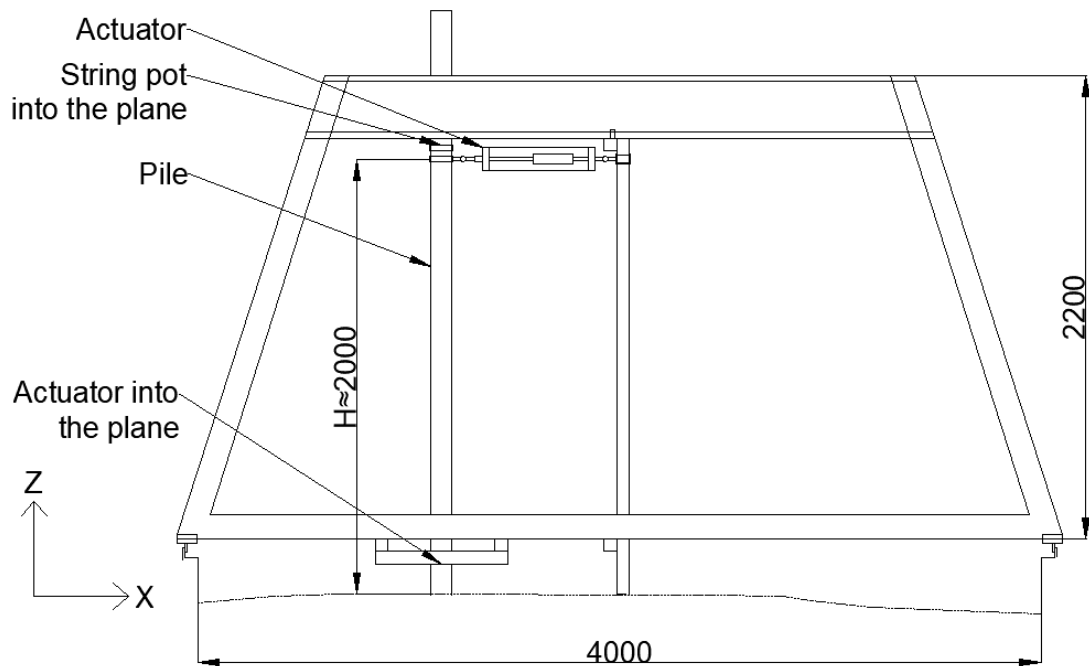**Test 1 - pure horizontal loading**

(a)
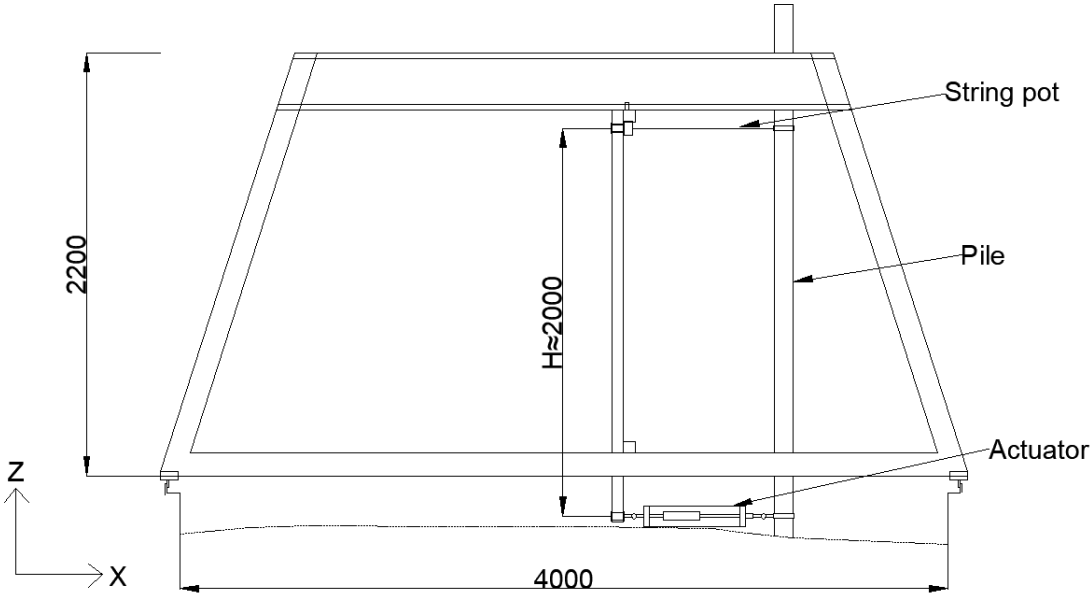
(b)

Figure A2.1: (a) Picture of test setup for test nr.1. (b) Schematic drawing of test setup for test nr.1. Note that not all details are drawn to scale, and all units are in mm. Depth of support frame is 600mm.

Test 2 - pure moment loading

(a)
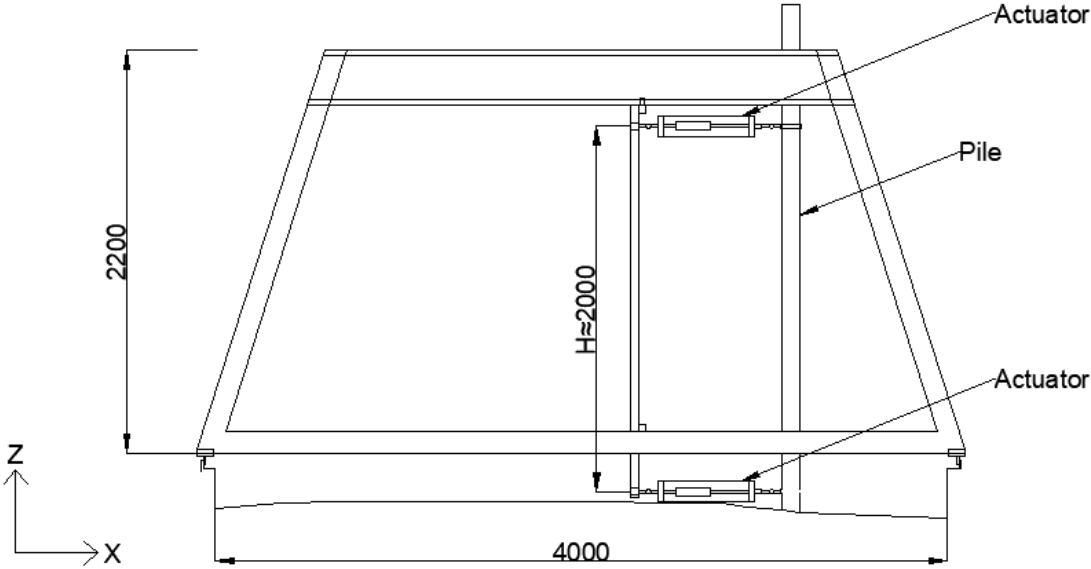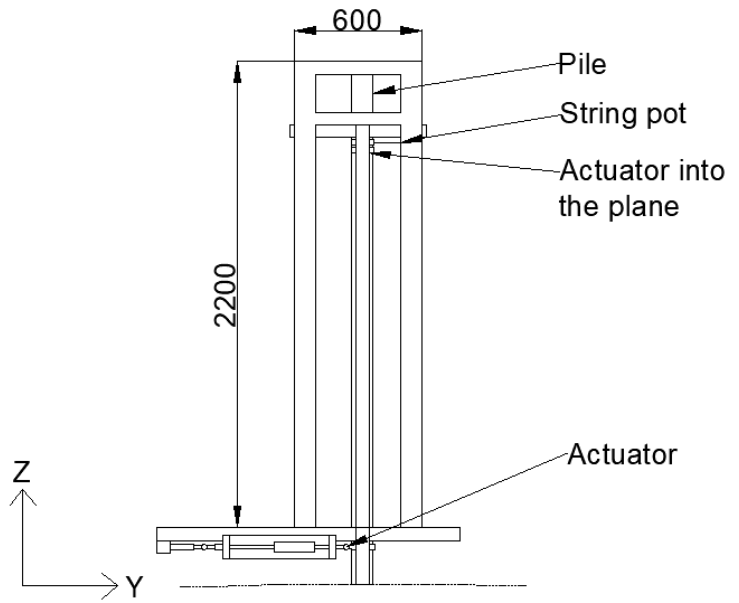

(b)

Figure A2.2: (a) Picture of test setup for test nr.2. (b) Schematic drawing of test setup for test nr.2. Note that not all details are drawn to scale, and all units are in mm. Depth of support frame is 600mm.

Test 3 - in plane combination of loads

(a)

(b)

Figure A2.3: (a) Picture of test setup for test nr.3. (b) Schematic drawing of test setup for test nr.3. Note that not all details are drawn to scale, and all units are in mm. Depth of support frame is 600mm.

Test 4 - multidirectional loading

(a)

(b)

Figure A2.4: (a) Picture of test setup for test nr.4 in plane. (b) Schematic drawing of test setup for test nr.4 in plane. Note that not all details are drawn to scale, and all units are in mm. Depth of support frame is 600mm.

Figure A2.5: (a) Picture of test setup for test nr.4 out of the plane. (b) Schematic drawing of test setup for test nr.4 out of the plane. Note that not all details are drawn to scale, and all units are in mm.

Figure A2.6: Picture of test setup for test 4 seen at an angle.

A3 Specialization project, fall 2019

Ingrid Gryteland Holm

A study of a macro model and its performance compared to FEA

Trondheim, December 2019

NTNU – Trondheim
Norwegian University of
Science and Technology

Abstract

The purpose of this project has been to get familiar with the macro model proposed by Ana Page (Page, 2018), which is a model made to efficiently describe the behaviour of monopiles in integrated load analyses. Furthermore, to test it with input computed with the geotechnical software PLAXIS 3D for a monopile in dry sand, which will be tested in the foundation laboratory at NTNU next semester.

Data from previous laboratory testing at NTNU was used as basis for choice of soil and pile parameters to use in PLAXIS, but the soil parameters were adjusted and different combinations were tried. In total four different models were made, and pile response under multidirectional loading was calculated with both PLAXIS and the macro model for all models. The models responded quite different to loading, but it is not easy to say which model represents the real pile response the best, and the soil parameters must be adjusted when data from laboratory testing becomes available.

Ana Page concluded in her Phd, that the model was easy to calibrate and could reproduce the response computed by FEA with sufficient accuracy (Page, 2018). However, the writer struggled to calibrate the macro model, and found that the model was sensitive to the input. Furthermore, in some cases the macro model produced unrealistic pile response that did not match with the response computed with PLAXIS at all. The reason for these strange results, and the calibration difficulties have not been found, and must be further investigated in the master thesis.

List of Figures

List of Tables

Contents

List of symbols

A_{real}	Real area of cylinder cross section
$A_{equivalent}$	Equivalent area of cylinder cross section
c'	Cohesion
D	Diameter
E_i	Initial Young's modulus
E_{50}^{ref}	Reference Young's modulus for loading
E_{50}	Young's modulus for loading
E_{ur}^{ref}	Reference Young's modulus for unloading
E_{ur}	Young's modulus for unloading
E_{oed}^{ref}	Reference oedometer modulus
E_{oed}	Oedometer modulus
G_0^{ref}	Reference shear modulus at small strains
G_0	Shear modulus at small strains
H	Horisontal force
H_x	Force in x-direction
H_y	Force in y-direction
H_z	Force in z-direction
I_{real}	Real cylinder cross sectional second area moment
$I_{equivalent}$	Equivalent cylinder cross sectional second area moment
$\boldsymbol{K}$	Elastic stiffness matrix
K_0	Earth pressure coefficient
K_0^{NC}	Earth pressure coefficient for normal consolidation
L	Length
m	Stress exponent
M	Overturning moment
M_x	Moment around x-axis
M_y	Moment around y-axis
M_z	Moment around z-axis
p_{ref}	Reference stress equal to atmospheric pressure

q_a	Asymptotic shear strength
q_f	Deviatoric failure stress
$\boldsymbol{R}$	Force vector
u_x	Displacement in x-direction
u_y	Displacement in y-direction
u_z	Displacement in z-direction
u_H	Displacement caused by horizontal force, H
u_M	Displacement caused by overturning moment, M
$\boldsymbol{v^e}$	Elastic displacement vector
ϵ_1	Axial strain
γ_{sat}	Saturated unit weight
γ_{unsat}	Unsaturated unit weight
$\gamma_{0.7}$	Threshold shear strain at which the shear modulus has reduced to 70 %
γ_{real}	Real unit weight of pile
$\gamma_{equivalent}$	Equivalent unit weight of pile
ϕ	Friction angle
ψ	Dilatancy angle
ν	Poisson's ratio
ν_{ur}	Poisson's ratio for unloading and reloading
σ_v	Vertical stress
σ_1	Largest principle stress
σ_3	Smallest principle stress
θ_x	Rotation around x-axis
θ_y	Rotation around y-axis
θ_z	Rotation around z-axis
θ_H	Rotation caused by horizontal force, H
θ_M	Rotation caused by overturning moment, M

Acronyms

DOFs	Degrees of freedom
FE	Finite element
FEA	Finite element analysis
HS	Hardening soil
HS-Small	Hardening soil small strain
NC	Normally consolidated
OC	Overconsolidated
OWT	Offshore wind turbine

Chapter 1

Introduction

In design of offshore wind turbines (OWTs), foundation on monopiles is a popular solution. Todays industry practice to represent the foundation behaviour in integrated load analyses, is the py-method. This method is developed for long, flexible and slender piles (Det Norske Veritas, 2014). The monopiles used as foundation for OWTs are not flexible and slender, and the method is in general not valid (Det Norske Veritas, 2014). By the use of py-curves, foundation stiffness and fundamental frequencies tend to be underestimated (Zaaijer (2006) and Hald et al. (2009)). Finite element analysis (FEA) can also be used to predict the pile response, but in design of OWTs, the response to thousands of load cycles are simulated, and FEA is therefore too time consuming and costly as it requires great computational effort. As a results, one is looking to other methods in order to increase the accuracy and efficiency in predicting pile response in load analyses.

In her Phd research, Ana Page worked on developing a model to accurately describe the soil and pile response in integrated load analyses (Page, 2018). She proposes a macro model, which will be presented in this paper. The macro model concept is to describe the pile response in one node located at the interface between foundation and structure. The model must be calibrated, typically by the use of FEA, but only two loads cycles are needed. For the rest of the load analyses, the macro model is used with much higher efficiency than FEA, and with similar accuracy.

So far, Ana has verified the foundation model against monotonic and cyclic FEA in clay and layered soil profiles, and against large-scale tests in clay (Page, 2018). Her recommendations for further research is to do analyses on drained and undrained sands, and compare with small and large scale field tests. Particularly comparison with multidirectional load tests in field are

recommended. In the master thesis that will take place next semester, a small scale test of a pile in dry sand will be performed and compared with the macro model. This project is a background study for the master thesis. Simulations of the lab pile have been performed in the geotechnical finite element (FE) program PLAXIS 3D, in order to calibrate the macro model, and to compare with the predicted response under multidirectional loading. An extensive amount of time have been spent on understanding the macro model, and to get familiar with the soil model used in PLAXIS 3D.

Chapter 2

Theory

2.1 Macro models

Ana Page have formulated a model (Page et al., 2019) that describes a pile's response to loading in one point, located in the interface between foundation and structure, usually at seabed. The situation is illustrated in Figure 2.1. This macro model requires much less computational effort than traditional finite element analysis (FEA), and predicts the pile behavior with higher accuracy than the conventional py-curve method described in Det Norske Veritas (2014).
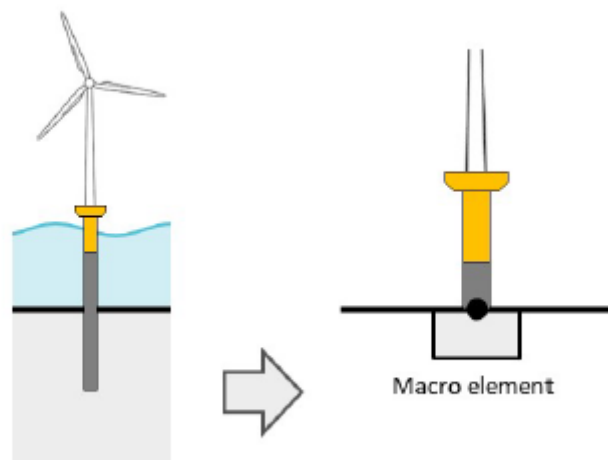

Figure 2.1: Figure showing the concept of the macro model, from Løkke et al. (2018).

The macro model applies load at the center of the pile head, and the pile response is described with only six degrees of freedom (DOFs). These DOFs are three displacements, u_x, u_y

and u_z, and three rotations, θ_x, θ_y and θ_z. The sign convention is shown in Figure 2.2. The response to vertical load and torsion is considered elastic and uncoupled, whereas the response to lateral loading is described as non-linear and with a coupling between the response in perpendicular planes, that is between u_x and θ_x, and u_y and θ_y (Page et al., 2019).

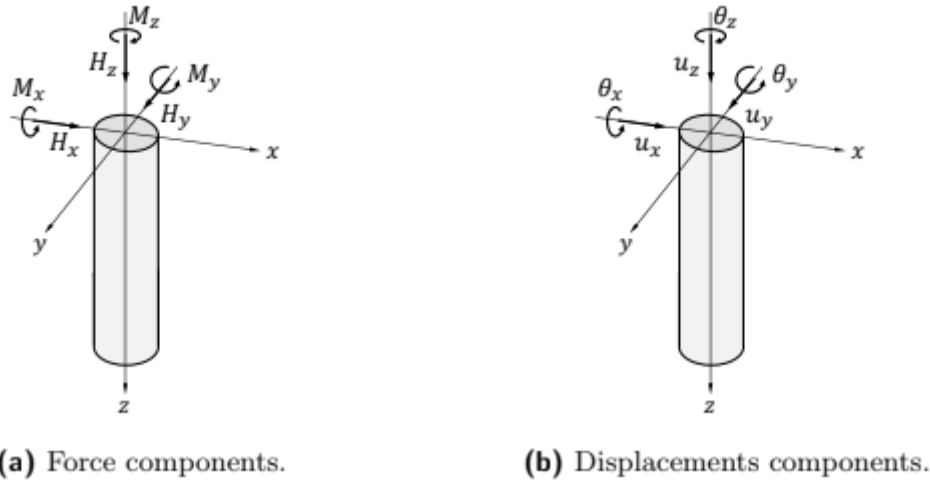**(a)** Force components.   **(b)** Displacements components.

Figure 2.2: Figure showing the sign convention used in the macro model, from Page (2018).

The model is based on multi-surface plasticity, where an initial yield surface describes the border between elasticity and elastoplasticity (Page et al., 2018). A failure surface represents the limit of possible force states. In between these two surfaces are load surfaces, and the plastic response between the surfaces depend on how the load surfaces move in load space, in other words the hardening (Løkke et al., 2018). In this model, kinematic hardening is applied, which means that the surfaces can translate and even intersect, however they do not change shape or size (Page et al., 2018). Figure 2.3 shows how the yield surfaces translate in the load space. The loading surfaces represent contours of constant plastic work and the response between each load surface is incrementally linear. Each load increment causes elastoplastic displacement, and whenever a new load surface is reached, plastic strains occur (Page et al., 2018). Plastic flow in this model is defined by an associated flow rule, meaning the direction of plastic flow is perpendicular to the yield surface (Nordal, 2019). The elastic response of the pile is determined by an elastic stiffness matrix (Page et al., 2018).
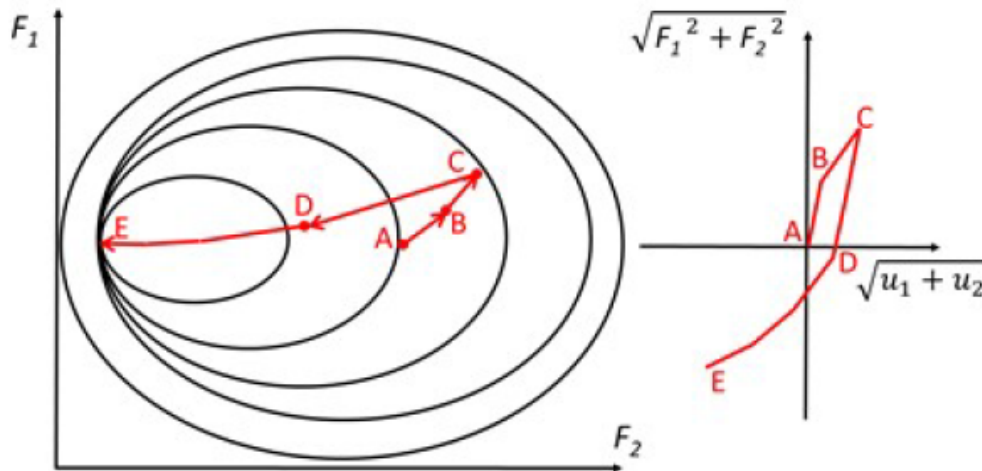
Figure 2.3: Figure illustrating the multi-surface plasticity model and the translation of yield surfaces in load space, from Løkke et al. (2018).

The necessary input in this model are an elastic stiffness matrix, and non linear load-displacement curves. The number of loading surfaces, as explained in previous paragraph, can also be selected (Løkke et al., 2018). Load-displacement curves can be extracted from FEA, by running two static pushover analyses; one with an overturning moment at seabed, and one with lateral load applied at seabed, shown in Figure 2.4. The load displacement curves must be monotonically increasing (Løkke et al., 2018). It is assumed that the response is equal in all horizontal directions (Page et al., 2018). Even though FEA may be needed to calibrate the model, only two load cycles need to be run with FEA, whereas the rest of the maybe thousands of load cycles can be run with the macro model.
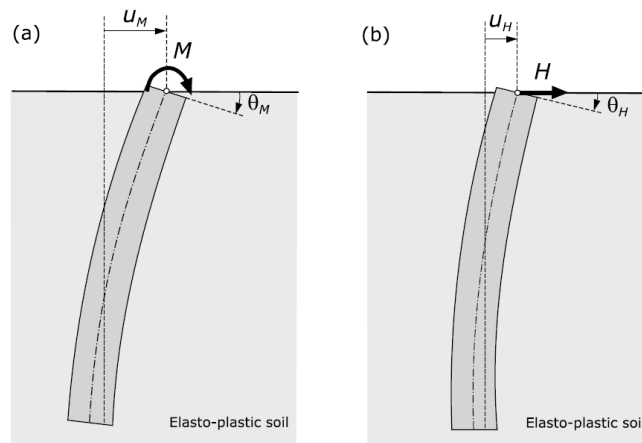

Figure 2.4: Loading conditions applied to determine non linear load-displacement curves, from Page et al. (2018)

Advantages of the macro model are (Page et al., 2018):

- The pile response is condensed to one node, which requires few DOFS.

- The method is easy to implement

- Pile response is predicted with almost the same accuracy as FEA, but with much less computational effort.

- The overall stiffness and hysteretic damping at seabed is easier and more precisely determined, especially in layered soils, than with traditional py-methods.

Limitations of the macro model are (Page, 2018):

- Forces and displacements are only computed at the center of the pile head, and consequently the response along the rest of the pile must be determined by other methods.

- It is assumed that the vertical loads have no impact on the lateral response, however this impact is not expected to be of significance.

- The model is verified against FEA, with homogeneous clay or layered soil with predominantly clay, and assuming that pile and soil response does not depend on frequency. The use of the macro model is hence only applicable on situations where these assumptions are valid.

2.2 Hardening soil and hardening soil small strain

The hardening soil model (HS) in PLAXIS is an elastoplastic model that accounts for the stress dependent stiffness of soils. The model combines hardening in shear governed by a Coulomb criterion, with volumetric hardening governed by preconsolidation stress (PLA, 2018a). The hardening soil model with small strains additionally accounts for the stiffer behavior at very small strains (PLA, 2018a).

The yield surface in the hardening soil model consists of two components; a "cone" and a "cap". The cone is defined by the coulomb criterion and the cap is defined by the preconsolidation stress (Nordal, 2019). When shear loading approaches failure, the cone expands and plastic strains occur. Similarly, volumetric loading past preconsolidation stress causes expansion of the cap and corresponding plastic volumetric strains. This behaviour is similar to that in an

oedometer test; stiff in the overconsolidated (OC) area and softer behavior in the normally consolidated (NC) area (Nordal, 2019). The elastic and plastic strains caused by shear are described by a hyperbola in case of a drained triaxial condition (PLA, 2018a), as displayed in Figure 2.5. In this figure, E_{50} is the secant modulus halfway to devatoric failure stress, q_f, E_{ur} is the elastic stiffness in unloading-reloading and q_a is the asymptotic shear strength defined as $q_a = q_f/0.9$. The total yield surface with the cone and the cap is visualized in Figure 2.6.
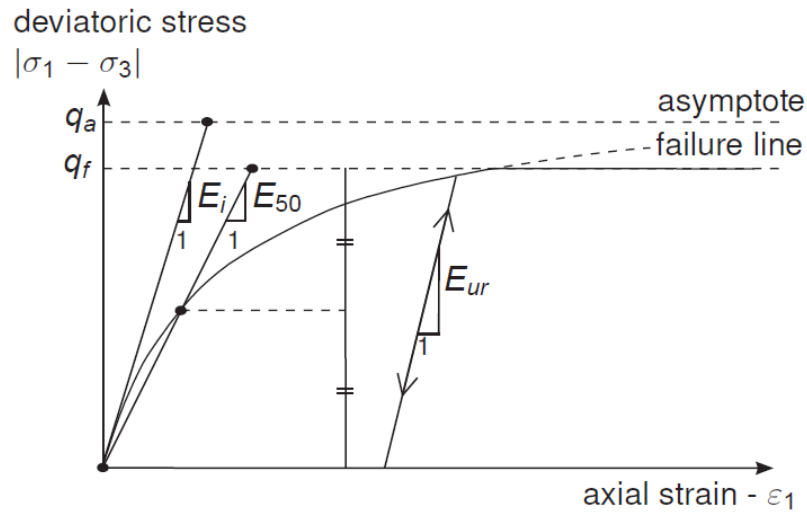

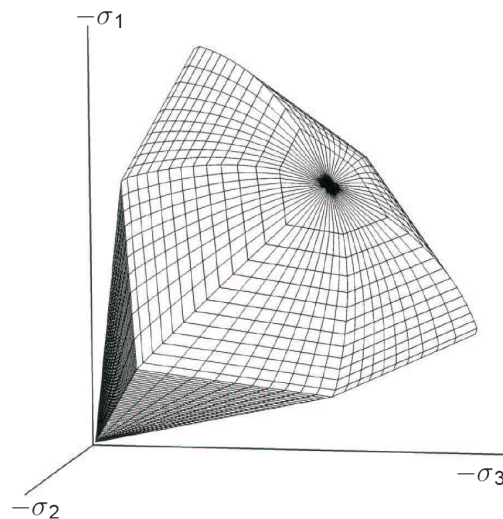Figure 2.5: Hyberbolic stress-strain relationship in a standard drained triaxial test (PLA, 2018a)

Figure 2.6: Yield surface represented by a cap and a cone in a principal stress diagram (PLA, 2018a)

The basic input parameters in the hardening soil model from (PLA, 2018a) is presented below.

- E_{50}^{ref} (kPa): Secant stiffness in standard drained triaxial test. Elastoplastic parameter controlling plastic strains caused by deviatoric loading

- E_{ur}^{ref} (kPa): Elastic unloading/reloading stiffness, connected to elastic unloading and reloading within the yield surface.

- E_{oed}^{ref} (kPa): Tangent stiffness for oedometer loading, connected to plastic strains caused by compression.

- m: Parameter controlling the stress dependent stiffnesses.

- c' (kPa): cohesion

- ϕ' (°): Friction angle.

- ψ (°): Dilatancy angle

- ν_{ur}: Poisson's ratio in unloading/reloading

- p^{ref} (kPa): Reference stress for stiffness, default 100kPa

- K_0^{NC}: K_0 for normal consolidation, default K_0^{NC} = 1-sinϕ

The reference parameters presented above are values defined at effective stress levels equal to p_{ref}; $\sigma_3' = p_{ref}$ for E_{50}^{ref} and E_{ur}^{ref}, and $\sigma_1' = p_{ref}$ for E_{oed}^{ref}. The stress dependent stiffnesses E_{50}, E_{ur} and E_{oed} are calculated according to equation 2.1, 2.2 and 2.3 respectively (PLA, 2018a).

$$E_{50} = E_{50}^{ref} \left(\frac{ccos\phi - \sigma_3' sin\phi}{ccos\phi + p^{ref} sin\phi} \right)^m \tag{2.1}$$

$$E_{ur} = E_{ur}^{ref} \left(\frac{ccos\phi - \sigma_3' sin\phi}{ccos\phi + p^{ref} sin\phi} \right)^m \tag{2.2}$$

$$E_{oed} = E_{oed}^{ref} \left(\frac{ccos\phi - \sigma_1' sin\phi}{ccos\phi + p^{ref} sin\phi} \right)^m \tag{2.3}$$

Under very small strains, soils are almost elastic and the initial stiffness is much larger than under larger strains PLA (2018a). The soil's stiffness decreases non linearly with increased strains, following the pattern in Figure 2.7. To account for the stiffer behaviour under very small strains,

the HS-Small model - hardening soil model with small strains - was developed by Thomas Benz (Benz, 2007). By including the initial soil stiffness, deformations at very small strains are not overestimated. The input parameters in this model are the same as in the HS model, but with two additional parameters; G_0^{ref} and $\gamma_{0.7}$. G_0^{ref} is the reference shear modulus at $\sigma_3' = p_{ref}$ and describes initial stiffness of the soil. $\gamma_{0.7}$ is the shear strain at which the shear modulus has decreased to $0.7G_0$. G_0 can be calculated according to equation 2.4, and $\gamma_{0.7}$ can be estimated with equation 2.5 (PLA, 2018a).

$$G_0 = G_0^{ref} \left(\frac{ccos\phi - \sigma_3'sin\phi}{ccos\phi + p^{ref}sin\phi} \right)^m \tag{2.4}$$

$$\gamma_{0.7} \approx \frac{1}{9G_0} \left(2c'(1 + 2cos(2\phi')) + \sigma_1'(1 + K_0)sin(2\phi') \right) \tag{2.5}$$
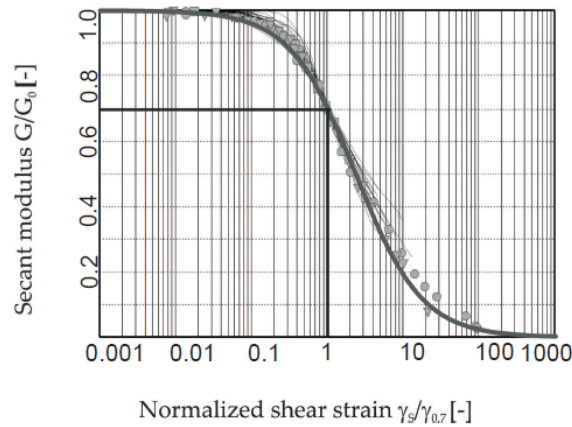

Figure 2.7: Diagram showing the nonlinear decay of shear modulus with strain, (PLA, 2018a)

Chapter 3

Methods

3.1 Literature search

Different methods were used to find relevant literature to this project. Two Phd's written at NTNU, Page (2018) and Hanssen (2016), were provided by supervisor Gudmund Eiksund as basis for the project, and the reference lists in these Phd's were used to find more elaborating literature. The user manuals to the program PLAXIS 3D have also been used extensively, along with the course material (Nordal, 2019) provided in the course TBA4116 - Geotechnical Engineering, Advanced Course at NTNU.

3.2 Previous laboratory testing

Previous Phd candidate Stian Hanssen (2016) performed a 1:20 scale test of a monopile installed in dry sand, in the foundation laboratory at NTNU. The concrete tank measures 4m x 4m in area, and was filled with a 2m thick layer of dry sand. The monopile used in the test was a cylindrical steel pile with 0.273m diameter, embedded 1.4m into the sand in the center of the tank. The same setup will be used in the master thesis next semester.

3.3 Modeling in PLAXIS 3D

Model and mesh

The setup explained in previous paragraph was used as base case to compare PLAXIS results with macro model results. The setup was modeled as a 4m x 4m x 2m soil block in PLAXIS 3D, with the pile center placed 2m from the model boundaries in both x and y direction.

PLAXIS 3D uses 10 node tetrahedral volume elements to represent the soil, whereas 12 node interface elements are used to model the soil-structure interaction (PLA, 2018b). The pile and the soil in a 0.5m radius from the pile center have been modeled with a refined mesh. The meshed model is shown in Figure 3.1.

<table>
<tr><td align="center">(a)</td><td align="center">(b)</td></tr>
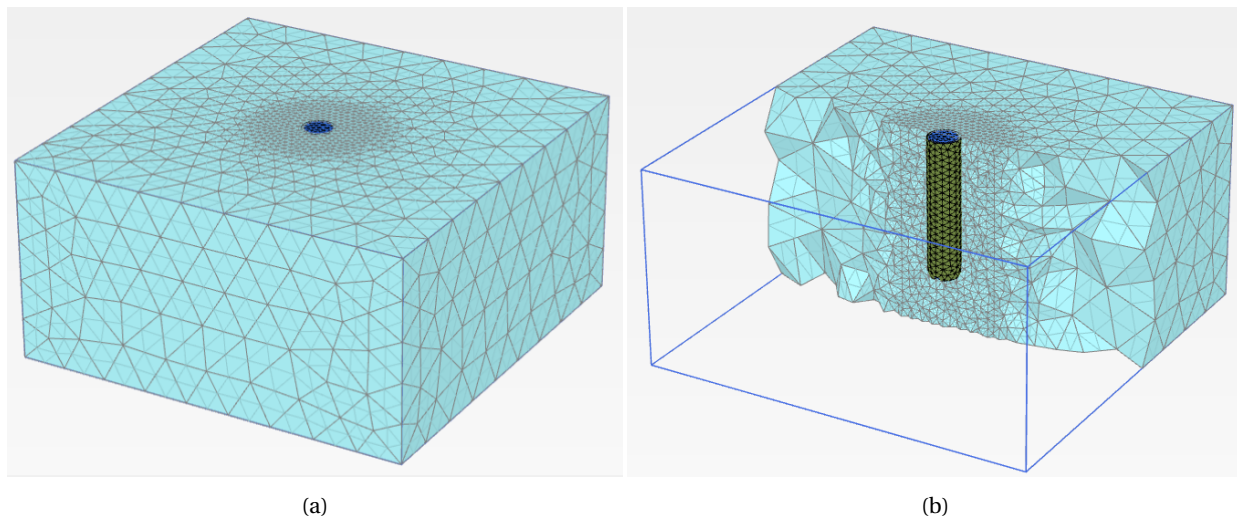</table>

Figure 3.1: (a) Figure showing the meshed PLAXIS model with one sand layer. (b) The figure shows a cut through the model, and the mesh refinement of the pile and around the pile.

Parameter selection

Soil and pile parameters are fetched from the work of Hanssen (2016), but there have been made some adjustments which will be explained shortly. The cylindrical steel pile with properties given in Table 3.1, was modeled as a linear elastic soil volume with an equivalent stiffness and unit weight, corresponding to the stiffness and unit weight of the hollow cylinder. The stiffness of the sand inside the pile is neglected, but the weight is accounted for in the unit weight. The equivalent pile parameters are presented in Table 3.1, and the formulation of equivalent stiffness and unit weight is presented in Equation 3.1 and Equation 3.2. The reason for modeling the pile as compact instead of the actual geometry, is that it is easier to extract pile forces from PLAXIS

for a compact volume than a cylinder. Pile forces were not needed in this project, but that was not known when the modeling started.

To be able to apply point loads which will distribute evenly over the pile head, a 10cm thick steel plate have been modeled on top of the pile.

$$E_{equivalent} = E_{real} \frac{I_{real}}{I_{equivalent}} \tag{3.1}$$

$$\gamma_{equivalent} = \gamma_{real} \frac{A_{real}}{A_{equivalent}} + \gamma_{sand} \tag{3.2}$$

Table 3.1: Parameters of the laboratory pile (Hanssen, 2016).

Parameter	Value
Diameter, D (m)	0.273
Embedded length, L (m)	1.4
Total length (m)	6.0
Wall thickness, t (m)	0.004
Unit weight, γ (kg/m^3)	7850
Young's modulus, E (GPa)	210
Poisson's ratio, ν	0.3

Table 3.2: Equivalent pile parameters used as input in PLAXIS 3D.

Property	Value
Material model	Linear elastic
Diameter, D (m)	0.273
Embedded length, L (m)	1.4
Unit weight, γ (kN/m^3)	20.45
Young's modulus, E (kPa)	23.55E6
Poisson's ratio, ν	0.3
Interface roughness, R	1.0

In Hanssen (2016), the author explains how shear wave velocity measurements have been used to decide the shear modulus of the sand, and an expression for the shear modulus with depth is derived (Equation 3.3).

$$G_{s,max} = 1000(p_{ref}\sigma'_v)^{0.5} + 39000 \tag{3.3}$$

In order to make a fairly good approximation of the shear modulus from shear wave velocity measurements with the HS-small shear modulus in Equation 2.4, and keep a stiffness exponent

of 0.5 which is normal for sands (Nordal, 2019), Hanssen (2016) chose to model the sand in four 0.5m thick layers with different reference moduli. The model with parameters from Hanssen (2016) is labeled model 1. In this project, the soil have been modeled in four different ways, and the parameters used are presented in Table 3.3.

To model the sand as one soil layer, the expression for shear modulus, Equation 2.4, was fitted to the expression from shear wave velocity measurements, Equation 3.3, by changing the stiffness exponent, m, and reference modulus, G_0^{ref}, and minimizing the difference between the two expressions. The resulting reference shear modulus and stiffness exponent, and the other parameters from Hanssen (2016) were used in model 2.

Using a different stiffness exponent, m, results in other stiffnesses, E_{50} (Equation 2.1), E_{ur} (Equation 2.2) and E_{oed} (Equation 2.3), than used by Hanssen (2016). To account for the difference, this difference was minimized by changing the reference moduli. The resulting parameters were used in model 3. Because the PLAXIS results from model 3, were not able to calibrate the macro model, the sand was also modeled with the HS soil model, and the reference stiffness given in Hanssen (2016). This model is labeled model 4.

Table 3.3: Soil parameters used in the four PLAXIS models.

Parameter	Parameter value			
	Model 1	Model 2	Model 3	Model 4
Condition	Drained	Drained	Drained	Drained
Soil model	HS-Small	HS-Small	HS-Small	HS
$\gamma_{sat} = \gamma_{unsat}$ (kN/m^3)	16	16	16	16
ϕ' (°)	38	38	38	38
c' (kPa)	0.1	0.1	0.1	0.1
ν_{ur}	0.2	0.2	0.2	0.2
E_{50}^{ref} (MPa)	82.036	82.036	34.727	82.036
E_{ur}^{ref} (MPa)	190	190	80.430	190
E_{oed}^{ref} (MPa)	50	54 [1]	28.519	50
m	0.5	0.186	0.186	0.5
G_0^{ref} (MPa)	461.495 341.091 299.551 278.140	134.369	134.369	–
γ_{07}	2.41E-06 2.02E-05 3.24E-05 4.26E-05	1.019E-06	1.019E-06	–

[1] PLAXIS required a minimum $E_{oed}^{ref} \geq 54$MPa in combination with the other stiffnesses, hence the increase.

Load application

In order to compare predicted pile response from the macro model with PLAXIS, multidirectional loading, presented in Table 3.4, have been applied. The required load displacement curves from static pushover analyses were also obtained by applying the load in Table 3.4, according to the macro model sign convention (Figure 2.2).

Table 3.4: Loading applied in static pushover analyses in PLAXIS 3D, and multidirectional loading applied in both PLAXIS 3D and the macro model. Loads according to the macro model sign convention (Figure 2.2).

	Static pushover analyses in PLAXIS 3D		
Load	Horizontal force	Overturning moment	Multidirectional loading
H_x	10kN		1kN
H_y			2kN
M_x		10kNm	1kNm

3.4   Input parameters in the macro model

As mentioned in chapter 2, the macro model needs an elastic stiffness matrix as input. This elastic stiffness matrix is computed from the first load step from calculations in PLAXIS. Two load cases are considered, only applying moment at the pile head, and only applying horizontal force at the pile head. The resulting force-displacement, and moment-rotation curves can be used to calculate $\boldsymbol{K}$ in Equation 3.4.

$$\boldsymbol{K}\boldsymbol{v}^e = \boldsymbol{R} \tag{3.4}$$

Two basis cases, Equation 3.5 and Equation 3.6, are used to obtain four equations in matrix form, with four unknown stiffness parameters;

$$\begin{bmatrix} k_{11} & k_{12} \\ k_{21} & k_{22} \end{bmatrix} \begin{bmatrix} u_H \\ \theta_H \end{bmatrix} = \begin{bmatrix} H \\ 0 \end{bmatrix} \tag{3.5}$$

$$\begin{bmatrix} k_{11} & k_{12} \\ k_{21} & k_{22} \end{bmatrix} \begin{bmatrix} u_M \\ \theta_M \end{bmatrix} = \begin{bmatrix} 0 \\ M \end{bmatrix} \tag{3.6}$$

By rearranging the four equations above, the following expressions for each element in the

elastic stiffness matrix are achieved:

$$k_{22} = \frac{Mu_H}{\theta_M u_H - \theta_H u_M} \tag{3.7}$$

$$k_{21} = -\frac{M\theta_H}{\theta_M u_H - \theta_H u_M} \tag{3.8}$$

$$k_{12} = \frac{Hu_M}{\theta_H u_M - \theta_M u_H} \tag{3.9}$$

$$k_{11} = -\frac{H\theta_M}{\theta_H u_M - \theta_M u_H} \tag{3.10}$$

The stiffness matrices obtained using the method explained above, have been compared with formulas for dynamic stiffness of rigid piles embedded in soils with parabolic increase of soil modulus with depth, from Gazetas (1991). In Gazetas's formulations, Young's modulus for the soil is required, and this is chosen based on the shear modulus from shear wave velocity measurements in Hanssen (2016), and the connection between shear modulus and Young's modulus in Equation 3.11. The elastic Young's modulus was roughly estimated as the apparent value of the Young's modulus at one pile diameter's depth, $E = 150$MPa (Hanssen, 2016).

$$E = 2G(1 + \nu) \tag{3.11}$$

Displacements and ΔM_{stage}, which is the completed proportion of a plastic calculation in PLAXIS (PLA, 2018b), are direct output for selected nodes in PLAXIS. ΔM_{stage} is used to calculate the applied load in each loadstep, and displacements are used to calculate rotations as it is no direct output from PLAXIS.

To avoid numerical issues with nodes selected in the interface between pile and plate, and the load application point, a node 0.03m under the top is selected, and used as representative for the pile head. Deformations are small, and the difference between the pile top an 3cm below, is negligible.

Rotation of the pile head can be calculated according to Equation 3.12 and 3.13, where (x_1, z_1) and (x_2, z_2) are the coordinates of two nodes along the pile centerline. In this case, the vertical distance between the two nodes are selected as approximately 10cm. Figure 3.2 shows the

situation. Due to small displacements, the impact of the vertical displacements on the rotation is considered negligible.
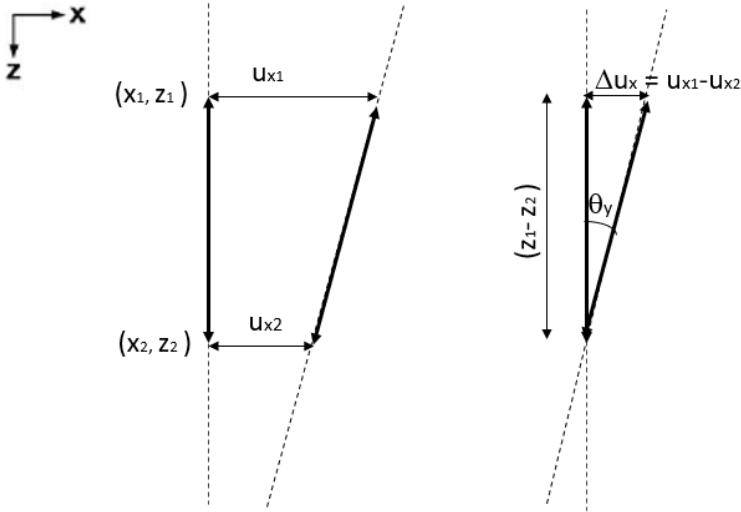

Figure 3.2: Sketch of how rotation of the pile head is calculated. Defintions for Equation 3.12 and 3.13.

$$\theta_x = \arctan\left(\frac{u_{y1} - u_{y2}}{z_1 - z_2}\right) \tag{3.12}$$

$$\theta_y = \arctan\left(\frac{u_{x1} - u_{x2}}{z_1 - z_2}\right) \tag{3.13}$$
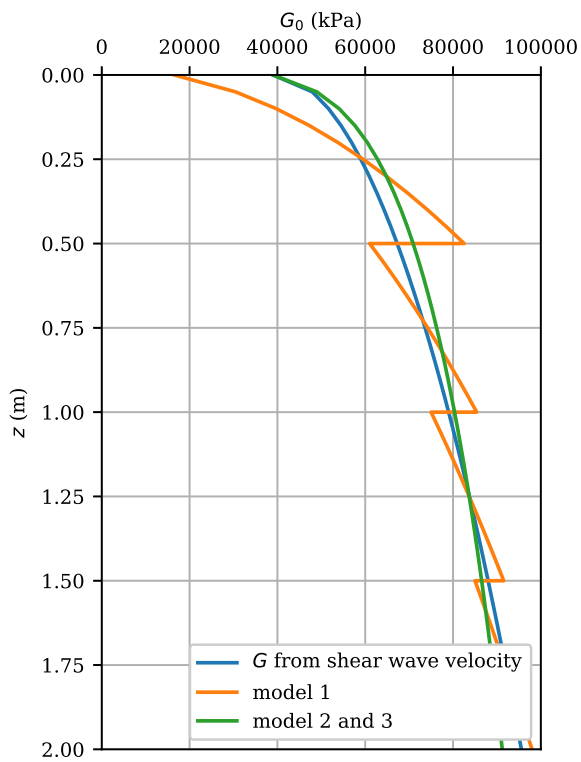
Chapter 4

Results

4.1 Parameter selection

Figure 4.1: Shear modulus with depth from shear wave velocity and model 1 (Hanssen, 2016), model 2 and 3.
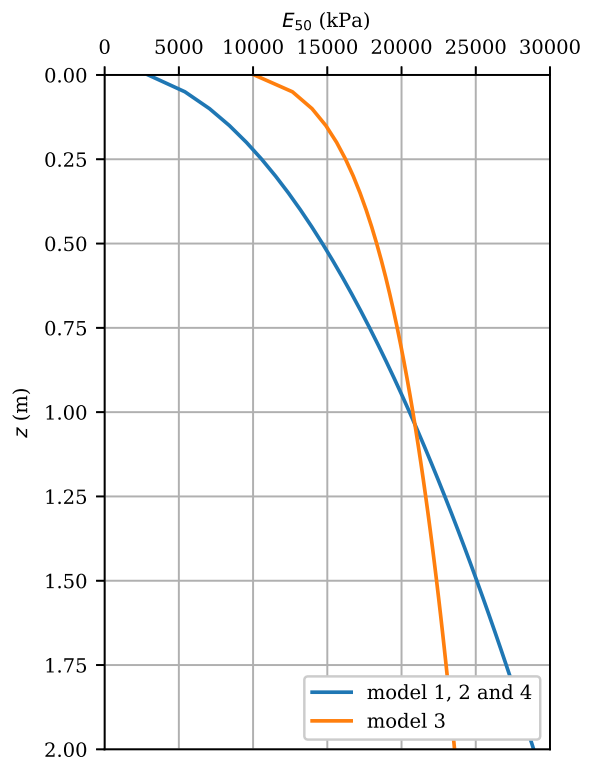
Figure 4.2: Secant modulus for model 1 (Hanssen, 2016), model 2, 3 and 4.
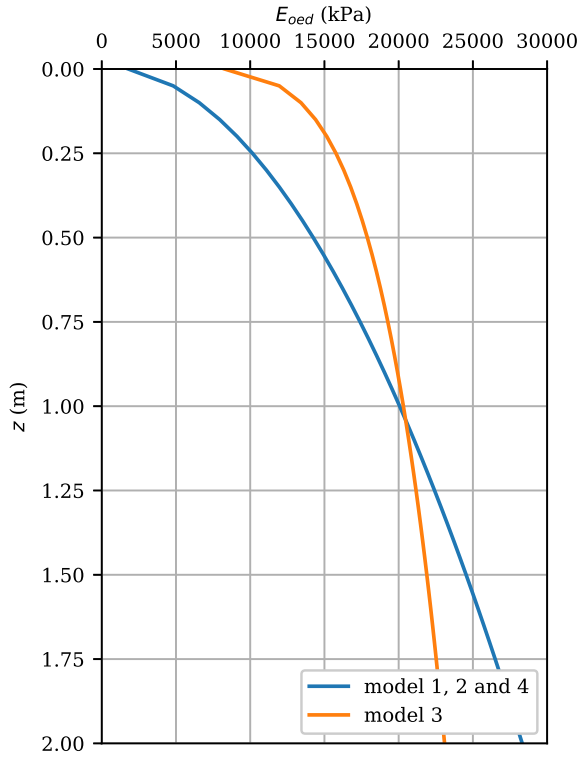
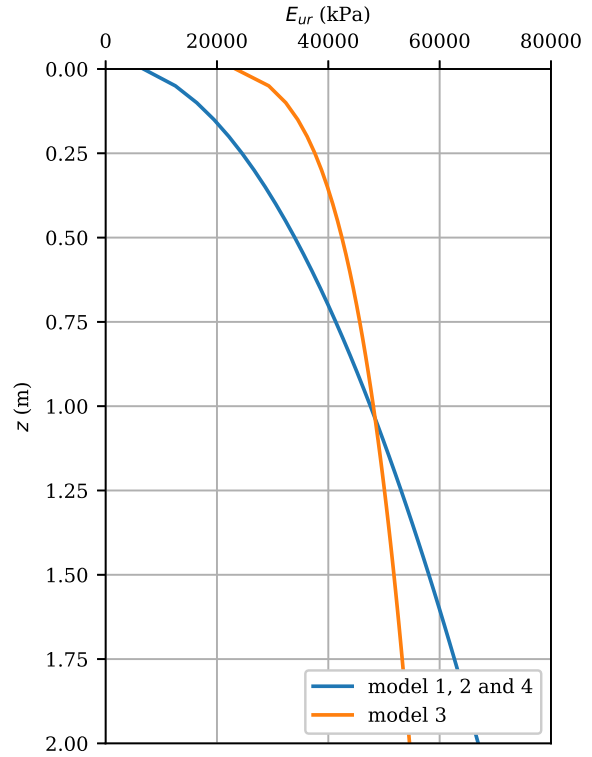Figure 4.3: Oedometer modulus for model 1 (Hanssen, 2016), model 2, 3 and 4.

Figure 4.4: Unloading/reloading modulus for model 1 (Hanssen, 2016), model 2, 3 and 4.
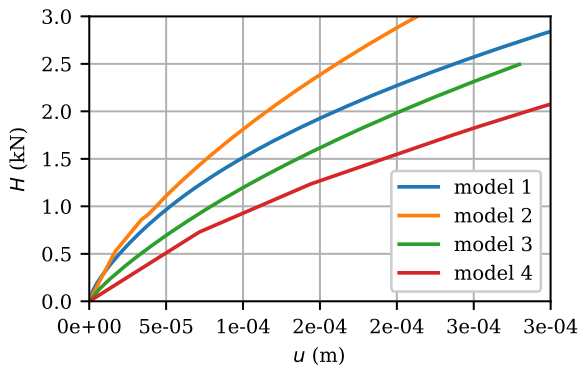
4.2   Macro model input

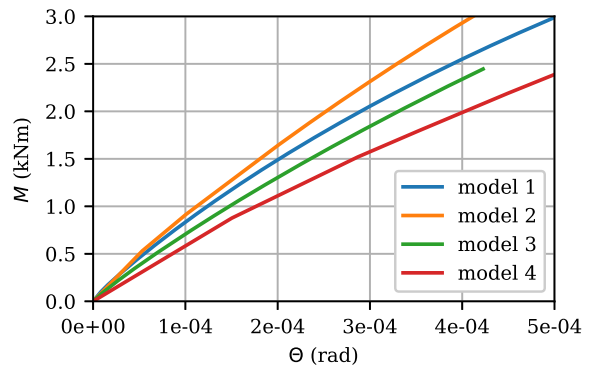Figure 4.5: Horizontal force-dipslacement curves for the four models, used as input in the macro model.

Figure 4.6: Moment-rotation curves for the four models, used as input in the macro model.

Table 4.1: Elastic stiffness matrices for all the models, and by the method of Gazetas (1991).

Element	Model 1	Model 2	Model 3	Model 4	Gazetas
k_{11} (kN/m)	1.060E+05	7.298E+04	4.209E+04	2.657E+04	5.011E+05
k_{12} (kN)	-3.853E+04	-3.017E+04	-1.919E+04	-1.595E+04	-4.234E+05
k_{21} (kN)	-4.211E+04	-3.240E+04	-2.255E+04	-1.561E+04	-4.234E+05
k_{22} (kNm)	2.722E+04	2.335E+04	1.912E+04	1.519E+04	8.660E+05

4.3 Multidirectional loading
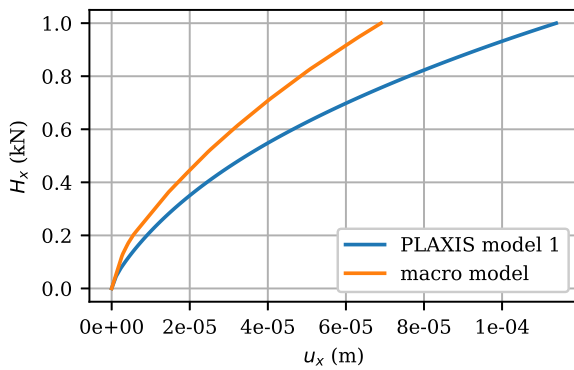
Model 1

Figure 4.7: Horizontal force in x-direction vs. horizontal displacement for model 1 computed with PLAXIS and the macro model.
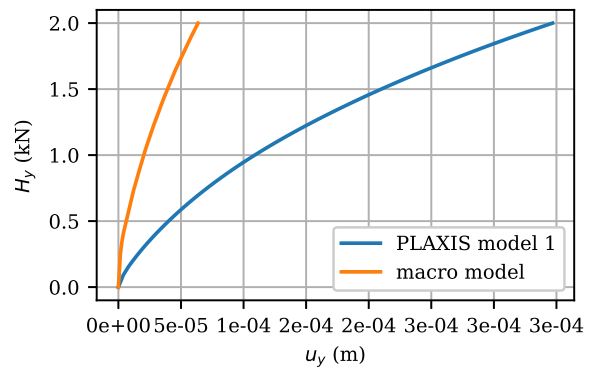

Figure 4.8: Horizontal force in y-direction vs. horizontal displacement for model 1 computed with PLAXIS and the macro model.
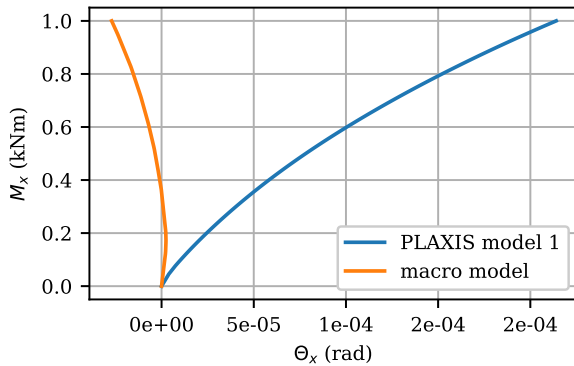

Figure 4.9: Moment around the x-axis vs. rotation for model 1 computed with PLAXIS and the macro model.
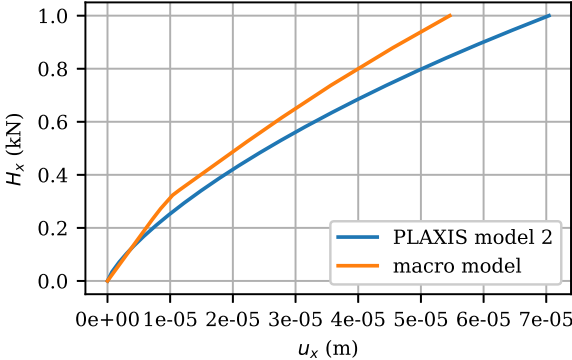
Model 2

Figure 4.10: Horizontal force in x-direction vs. horizontal displacement for model 2 computed with PLAXIS and the macro model.

Figure 4.11: Horizontal force in y-direction vs. horizontal displacement for model 2 computed with PLAXIS and the macro model.

Figure 4.12: Moment around the x-axis vs. rotation for model 2 computed with PLAXIS and the macro model.

Model 4

Figure 4.13: Horizontal force in x-direction vs. horizontal displacement for model 4 computed with PLAXIS and the macro model.
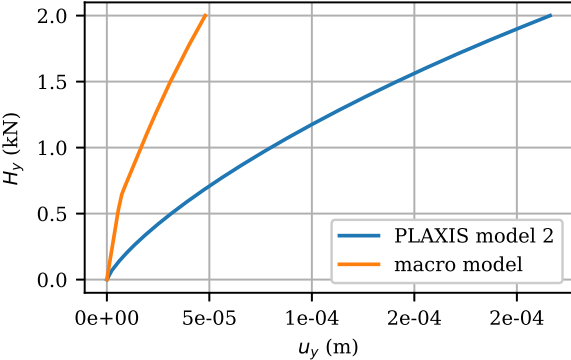

Figure 4.14: Horizontal force in y-direction vs. horizontal displacement for model 4 computed with PLAXIS and the macro model.
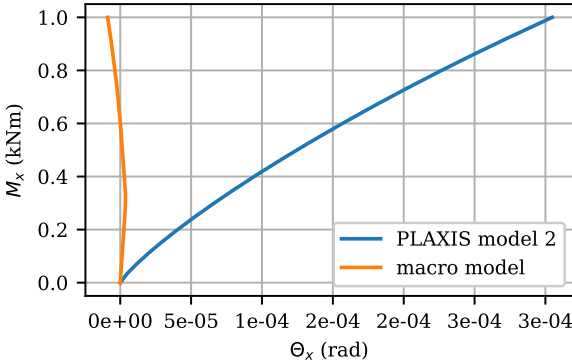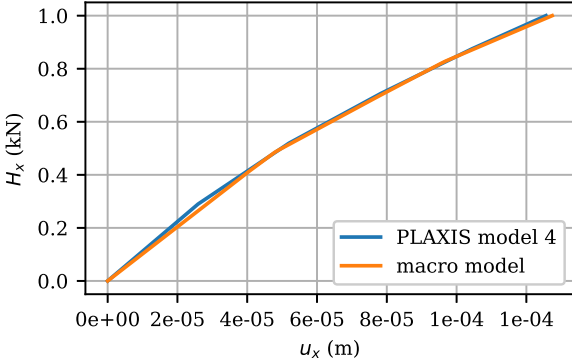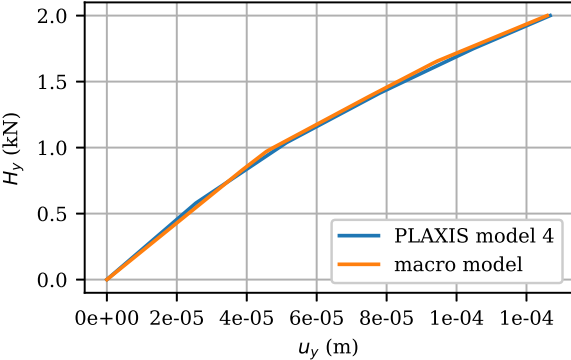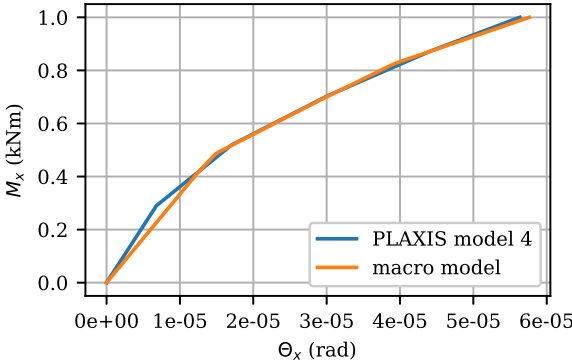

Figure 4.15: Moment around the x-axis vs. rotation for model 4 computed with PLAXIS and the macro model.

Chapter 5

Discussion

5.1 Discussion of results

Figure 4.1 shows the shear modulus with depth from shear wave velocity measurements (Hanssen, 2016), and the ones used in the different models. The profile produced by adjusting the stress exponent corresponds better with the shear wave profile, than the profile used by Hanssen (2016). Figure 4.2, Figure 4.3 and Figure 4.4 display the other stiffness profiles obtained by changing the stress exponent, in comparison with the profiles used by Hanssen (2016). Note that these curves do not indicate which model is the best, they are only a comparison of stiffness. It will be interesting to see which model predicts the pile response best, when lab testing have been done.

Figure 4.6 and Figure 4.5 display the load-displacement and moment-rotation curves from static pushover analyses in PLAXIS. It can be seen that the stiffness of the four models, are quite different. This is also seen in the computed elastic stiffness matrixes presented in Table 4.1. The stiffness matrixes computed from PLAXIS are softer compared to the stiffness matrix computed with the method of Gazetas.

During the analyses, in all four models, PLAXIS was unable to apply all the load and bring the soil to failure. The load advancement stopped at different load levels in the four models, and the failure loads entered in the macro model were hence different. However, the purpose of this project was to compare the pile behaviour before failure, predicted by the macro model and by PLAXIS, and the failure load is therefore not important.

Load-displacement and moment-rotation curves from multidirectional loading for model 1,

2 and 4 are shown in section 4.3. There are no results for model 3, because the macro model would not run. In case of model 4, the macro model corresponds very well with the PLAXIS results. However, in case of model 1 and 2, the match between PLAXIS and the macro model is poor. The macro model even predicts a negative rotation around the x-axis, which is illogical considering the load (Table 3.4). The reason for this negative rotation is unknown, and it is difficult to find out without looking at the macro model code, which at this moment is unavailable. It should be noted that the macro model is only as good as the input, so poor input will produce poor output. There could therefore be something wrong with the input used, but this have not been discovered.

It turned out that the macro model was sensitive to which input curves were used. In many of the attempts to run the macro model, an error message saying that the multisurface plasticity model could not calibrate, occured. Another problem that arose, was that nothing happened after the macro model had read the input files, as it was iterating without convergence, and the model had to be interrupted. By playing around with number of points on the input load-displacement curves, the macro model sometimes succeeded. One suggestion as to why these problems occured, is that there were too rapid stiffness changes in the input curves, but this was not confirmed.

5.2 Modeling

As mentioned in previous chapters, the macro model needs load displacement curves from static pushover analyses with overturning moment, and horizontal load applied at seabed. These curves could have been obtained from PLAXIS, by only modeling half of the pile geometry, due to symmetry. This would have been more effective, however, the complete pile geometry was modeled in order to later apply multidirectional loading on the pile, without having to make new models.

The goal of this project was to get familiar with the macro model, and test it with input from PLAXIS. It was not necessary to use an advanced soil model in PLAXIS, like HS-Small, to produce input for the macro model. However, the PLAXIS models from this project will be used to compare with lab testing of a pile next semester and was a preparation for that.

The parameters used by Hanssen (2016) could also have been used directly, without mak-

ing any adjustments, but it was wanted to model the sand as one layer. Therefore, different combinations of parameters were tried, and the pile response was compared with the response obtained using the parameters from Hanssen (2016). Also, varying the PLAXIS parameters gave more data to test the macro model with. No conclusion of which parameters are most representative for the real sand have been made, but this will be further investigated in the master thesis.

Chapter 6

Conclusion

6.1 Conclusion

The purpose of this project was to get familiar with Ana Page's macro model concept, and furthermore test the model and compare with results from FEA. During the project it has become clear that the macro model is sensitive to the input, and does not always give reasonable output. The model is not robust enough to handle all kinds of input, and should therefore be further investigated.

6.2 Further work

The project work has lead to the following tasks that should be worked on in the master thesis:

- Get hold of and look into the macro model source code in order to find out why the model sometimes fails to run.

- Perform a small scale lab test of a pile in dry sand and compare with the macro model.

- Optimize the input soil parameters in PLAXIS, and compare with the lab test.

Bibliography

(2018a). *PLAXIS Material Models Manual.*

(2018b). *PLAXIS Reference Manual.*

Benz, T. (2007). *Small-Strain Stiffness of Soils and its Numerical Consequences.* PhD thesis, Universität Stuttgart.

Det Norske Veritas (2014). Design of Offshore Wind Turbine Structures - Offshore Standard DNV-OS-J101. DNV GL.

Gazetas, G. (1991). Foundation vibrations. *Foundation Engineering Handbook*, pages 553–593.

Hald, T., Mørch, C., Jensen, L., Bakmar, C., and Ahle, K. (2009). Revisiting monopile design using py curves. results from full scale measurements on horns rev. In *Proceedings of European Offshore Wind 2009 Conference.*

Hanssen, S. B. (2016). *On the Determination of Spring Stiffness for Laterally Loaded Monopiles.* PhD thesis, NTNU.

Løkke, A., Page, A., and Skau, K. (2018). Redwin - reducing cost of offshore wind by integrated structural and geotechnical design. Technical report, NGI.

Nordal, S. (2019). Geotechnical engineering advanced course.

Page, A. (2018). *Monopile Foundation Models for Dynamic Structural Analyses of Offshore Wind Turbines.* PhD thesis, NTNU.

Page, A., Grimstad, G., Eiksund, G., and Jostad, H. (2018). A macro-element pile foundation model for integrated analyses of monopilebased offshore wind turbines. *Ocean Engineering*, 167:23–35.

Page, A., Grimstad, G., Eiksund, G., and Jostad, H. (2019). A macro-element model for multidirectional cyclic lateral loading of monopiles in clay. *Computers and Geotechnics*, 106:314–326.

Zaaijer, M. (2006). Foundation modelling to assess dynamic behaviour of offshore wind turbines. *Applied Ocean Research*, 28:45–57.